Galaxies in Milgromian Dynamics

Dissertation
zur
Erlangung des Doktorgrades (Dr. rer. nat.)
der
Mathematisch-Naturwissenschaftlichen Fakultät
der
Rheinischen Friedrich-Wilhelms-Universität Bonn

von
Fabian Lüghausen
aus
Bergisch Gladbach

Bonn, September 2014

Dieser Forschungsbericht wurde als Dissertation von der Mathematisch-Naturwissenschaftlichen Fakultät der Universität Bonn angenommen und ist auf dem Hochschulschriftenserver der ULB Bonn `http://hss.ulb.uni-bonn.de/diss_online` elektronisch publiziert.

1. Gutachter:	Prof. Dr. Pavel Kroupa
2. Gutachter:	Prof. Dr. Cristiano Porciani
Tag der Promotion:	21. Januar 2015
Erscheinungsjahr:	2015

Summary

Since its first formulation in 1983, Milgromian dynamics (also known as modified Newtonian dynamics or MOND) has been very successful in predicting the gravitational potential of galaxies from the distribution of baryons alone. This includes general scaling relations and detailed rotation curves of individual galaxies. To date, with only few Milgromian *N*-body codes and simulations available, only very little is known about the time-evolution of dynamical objects within that framework, and generic, fully dynamical tests using *N*-body codes with live particles, high spatial resolution, and full treatment of hydrodynamics are still missing. In the course of this thesis, I developed such a code, allowing to simulate generically the formation and evolution of galaxies in the Milgromian framework for the first time. This code, named Phantom of Ramses (POR), is based on the hydrodynamics and *N*-body code Ramses, and achieves exceptionally high spatial and temporal resolutions thanks to the adaptive mesh refinement technique. It includes hydrodynamical treatment of gas, and includes physical sub-grid processes (star formation, stellar feedback, etc.). Three research projects emerged during that development:

(i) Milgromian dynamics is tested in polar ring galaxies (PRGs). PRGs are ideal objects for studying the three-dimensional shapes of galactic gravitational potentials, because they feature two rotating components: the host galaxy, and a rotating polar ring that is typically oriented perpendicular to its host. Accordingly, two distinct rotation curves can be measured, both of which must be explained by the same gravitational potential. Observational studies have uncovered systematically larger rotation velocities in the extended polar rings than in the associated host galaxies. To test Milgromian dynamics in these objects, the Milgromian potential and the expected rotation curves are computed for a set of PRG models. It turns out that Milgromian dynamics naturally explains the systematic differences between the rotation velocities in the polar ring and those in the host galaxy, and that also the shapes and amplitudes of the predicted rotation curves match well with the observations.

(ii) The dynamical properties of the Milky Way's five most massive dwarf spheroidal satellites expected in Milgrom's modified gravity framework are investigated and compared to available observational data, taking into account self-consistently the external field of the Milky Way, which strongly affects the satellites' internal dynamics. The predicted effective dynamical masses for the most luminous ones, Fornax and Sculptor, agree well with available velocity dispersion data. Moreover, the central power-law slopes of the dynamical masses agree exceedingly well with values inferred observationally from velocity dispersion measurements. The predicted effective dynamical masses for Sextans, Carina and Draco are low compared to usually quoted observational estimates, as has already been pointed out in previous work. The possible consequences are discussed.

(iii) The final POR code is presented and explained. Testing results are shown, and sample applications are provided, including spherical equilibrium models, and models of exponential disk galaxies, with and without initial bulge. The software developed to set up the initial conditions of these sample models constitutes the basis of future projects with the new Milgromian dynamics code.

Acknowledgements

First and foremost, I want to thank my advisors, Pavel Kroupa and Benoit Famaey, for supporting and guiding me during the last few years. In 2010, during the time of writing my Diploma thesis in Pavel's group here in Bonn, Benoit presented to us the idea of developing a QUMOND-based N-body code, and Pavel provided me with the opportunity to realize this project in his research group in close collaboration with Benoit. As a programming enthusiast, I enjoyed the work very much. Not least because the subject itself is very interesting and provides us with a new view on the dynamics of galaxies. I therefore want to thank Pavel for this special opportunity, and for his motivation and enthusiasm on research in general. For striking new research paths when it becomes necessary, and for sharing his broad knowledge across the various subjects.

My special thank goes to Benoit, for welcoming me to the MOND community, and for his trust in me and my work. For sharing his knowledge and smart ideas with me, and for his great advice. In particular his very extensive review paper, which he has written together with Stacy McGaugh, has been a great help, and provided me (and surely others as well) with a profound overview of the research papers that appeared in this field in the past 30 years. I also thank Benoit for the many invitations to the Observatoire astronomique de Strasbourg, which have always been a joy. And for the fun we had together.

I would like to thank most sincerely the members of the thesis committee, Cristiano Porciani, Elisabeth Soergel, and Martin Langer, for their interest in my work and for reviewing this thesis, which I know comes along with a lot of additional work. I hope you will enjoy reading it.

I want to thank all my colleagues and friends from the Argelander Institute. I very much enjoyed the time we had together, the coffee breaks, lunch times, and the many chats and discussions, whether or not these were scientific or non-scientific. In particular, I want to thank Verena Lüghausen, Lars Flöer, Michael Brockamp, and Marcel Pawlowski for carefully proof-reading the introduction chapter, and for their honest opinions. I also want to thank Shahram Faridani for his friendship and encouragement during the past years.

At this point, I also want to thank Pavel again for the opportunity to attend several international conferences, which have been great experiences, and for the chance to travel to Canberra, Australia, funded by the DAAD, and the enjoyable time we had there together.

Last but not least, I want to thank my family. Foremost, I thank my lovely wife, Verena, for her invaluable encouragement in any and every possible way. Also, I thank my mother, my siblings, and my parents in law for the constant support and backup I experienced during the whole time.

Contents

CHAPTER 1

Introduction

1.1 Mass or acceleration discrepancy in the Universe

Since the early 1930s, a discrepancy has been observed in the Universe between the visible, baryonic mass on the one hand and the effective dynamical mass, inferred indirectly from the dynamics of stars and gas, on the other hand, when assuming gravity to be described by Newtonian dynamics. That discrepancy appears on very different scales. The first observational evidence was found by Oort (1932), who discovered that the vertical restoring force acting on the stars in the Solar neighborhood exceeds the value expected from star count data by a factor of ≈ 2. This became known as the Oort discrepancy. Whether that discrepancy is real or not is however still under debate today (Bovy and Tremaine, 2012; Bienaymé et al., 2014). Shortly after Oort's discovery, Zwicky (1933) observed, on a much larger scale, the velocity dispersion of the galaxies in the Coma cluster of galaxies to exceed the theoretical value expected from the visible mass by a factor of ≈ 400. This number reduces to ≈ 50 if today's measurements of the Hubble constant are used (van den Bergh, 1999), and further down to ≈ 6 if the extragalactic gas, which is visible in X-ray data, is taken into account (Hughes, 1989). Subsequently, Smith (1936) obtained a similar mass discrepancy for the Virgo cluster. Around the same time, Babcock (1939) has been the first to report a discrepancy between the rotation velocities and stellar mass estimates of the Andromeda galaxy. That discrepancy became widely accepted only much later, in the 1970s, when Rubin and Ford (1970) measured and analyzed the rotation curves of a sample of bright spiral galaxies. They found (i) that the rotation velocities of spiral galaxies are super-Keplarian, i.e. exceed significantly the velocities derived from the baryonic matter content; and (ii) that these rotation curves are approximately flat, even at large galactic radii at which already most of the mass is enclosed (see Figure 1.1), so that the circular orbit rotation velocity should decrease with the inverse square root of the galactic radius, $V_{\rm rot}(R) \propto R^{-1/2}$ (Rubin and Ford, 1970; Rubin et al., 1978, 1980). Their work has later independently been confirmed by Bosma (1981), whose contribution finally established the 'missing mass' problem in astronomy. Since then, the mass discrepancy has also appeared in cosmological models, in which additional, non-baryonic mass is needed to explain the growth of the large-scale structure and the angular power spectrum of the cosmic microwave background (CMB) (Bennett et al., 2013; Planck Collab., 2013a).

The observed discrepancy can have the following implications. (i) Let us assume that general relativity (GR) is the valid description of gravity on *all* scales. GR is well tested within the Solar System and in several other strong acceleration fields (e.g. gravitational lensing, binary pulsars), and is excel-

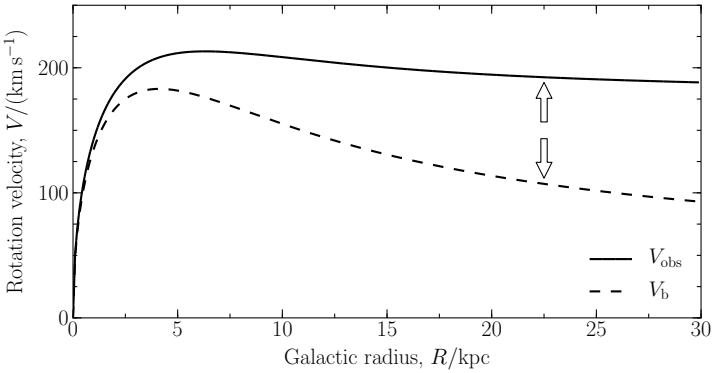

Figure 1.1: Example of a typical rotation curve (this example model is a thin exponential disk with a total mass of about $6 \times 10^{10}\,\mathrm{M}_{\odot}$ and a scale-length of 2.3 kpc, which is similar to the Milky Way). The dashed line shows the rotation curve expected by a Newtonian observer from the distribution of the baryonic mass, and falls off according to $V_{\mathrm{b}}(R) \propto R^{-1/2}$ at large radii. The solid line represents the typically measured rotation velocity, $V_{\mathrm{obs}}(R)$, which is asymptotically flat. (Here, V_{obs} has been derived analytically using the empirical mass discrepancy–acceleration relation that is detailed in Section 1.2) The discrepancy between the two rotation curves has been discovered by Babcock (1939) and has later been established by Rubin and Ford (1970) and Bosma (1981). The discrepancy can be explained by (i) the existence of unseen matter, or (ii) the deviation from GR, or (iii) both.

lently approximated by Newtonian dynamics on the scales of galaxies. If so, there must exist yet unseen matter, so called "dark matter" (DM), which provides the galaxies with additional mass and boosts the rotation curves. Or (ii) the former assumption is wrong, i.e. GR is not valid on all scales, and Newtonian dynamics does not account for the dynamics on low-acceleration scales, such as galaxies. In this case, the theory of gravity has to be revised. Or (iii) our understanding of gravity needs to be revised *and* additional DM is required.

Gravity is the least understood of the four fundamental forces, but it is the dominant force on large scales. The approaches (i) and (ii) generally lead to very different implications, for the dynamics of galaxies as well as for cosmology. The possible scenarios (i) and (ii) are discussed in this chapter.

Mass discrepancy: interpreting the discrepancy in terms of general relativity

In the 1980s, the first approach seemed obvious and is since then favored by the majority of astronomers. Hypothesizing the existence of additional, dark matter is convenient, because it allows using the established and well-known physics of gravity, at the price of postulating new particles which are not contained in the standard model of particle physics. Various DM candidates have been considered so far, but none of them has been directly detected to date (for a detailed review on the considered DM candidates and direct detection experiments, see Bertone et al., 2005). For the DM candidate favored today, the weakly interacting massive particle (WIMP, see below), a large range of possible cross sections has been excluded (XENON100 Collab., 2012; LUX Collab., 2013).

In the 1990s, a cosmological model has emerged from the GR-DM hypothesis: today's concordance model of cosmology, the so called the Λ cold dark matter (ΛCDM) model (Ostriker and Steinhardt,

1995). This model is a Friedmann-Lemaître cosmological model, based on Einstein's field equations and the assumption that the Universe is, on cosmological scales, isotropic and homogeneous. The composition of today's mass-energy density in units of the critical density, $\rho_{\rm cr} = 3H_0^2/(8\pi G)$, has been constrained to be: $\Omega_\Lambda = 0.685 \pm 0.017$ (dark energy); $\Omega_{\rm m} = 0.315 \pm 0.017$ (total, i.e. baryonic and dark matter); $\Omega_{\rm b} = 0.049 \pm 0.002$ (baryonic matter) (Planck Collab., 2013b). Today's total energy is $\Omega_{\rm tot} \approx 1$ in this model. The ΛCDM model postulates the existence of dissipationless, collisionless, dynamically cold dark matter (CDM) particles, which are non-relativistic at the time of decoupling (redshift $z \approx 1000$), to allow the formation of the small-scale structure we observe today, including individual galaxies, dwarf galaxies, etc. The concordance model is clear and simple, and performs exceptionally well in explaining the CMB power spectrum (Planck Collab., 2013a), the observed large-scale structure (e.g. Springel et al., 2005), the relative abundances of the light elements (hydrogen, helium, and lithium) through the Big Bang nucleosynthesis (BBN) (Alpher et al., 1948), and the expansion of the Universe as evidenced by Supernova type Ia data (e.g. Riess et al., 1998; Schmidt et al., 1998; Perlmutter et al., 1999).[1]

Two arguments exist for the DM particles to be non-baryonic. (i) The ΛCDM cosmological model requires the total matter density, $\Omega_{\rm m} = \Omega_{\rm b} + \Omega_{\rm DM}$, to be larger than the amount of baryonic matter inferred from BBN, $\Omega_{\rm b}$, to account for the observed growth of structure in the Universe (e.g. Springel et al., 2005). From the above listed constraints, $\Omega_{\rm m}/\Omega_{\rm b} \approx 6$. (ii) The densities of baryonic and non-baryonic matter are imprinted in the CMB power spectrum: before the decoupling at $z \approx 1000$, the density fluctuations in the primordial baryon-photon fluid did not grow, but were oscillating in the form of acoustic waves. At the time of the decoupling, these fluctuations are diffusion-damped. Diffusing damping (Silk, 1968) is more effective on smaller angular scales, meaning that the higher-order acoustic peaks visible in the CMB power spectrum should have a lower amplitude than the lower-order peaks. However, the non-baryonic DM is decoupled from the baryon-photon fluid, allowing it to grow instabilities on its own well before the baryon-photon decoupling. As a consequence, the decoupled DM component can overcome the diffusion damping of the oscillations, allowing the third peak of the CMB power spectrum to have an amplitude similar to that of the second peak. The observed equality of the amplitudes of the second and third acoustic peak is often considered as the strongest argument in favor of non-baryonic DM on large scales: any alternative to non-baryonic DM must provide some new degree of freedom, such as the existence of massive neutrinos, in order to effectively reproduce this behavior (Skordis et al., 2006).

In summary, the DM particle is expected to be an exotic, non-baryonic, dissipationless, collisionless, possibly weakly interacting, massive particle (WIMP) with a mass of the order of $\approx 100\,{\rm GeV}$ (e.g. Bertone et al., 2005). The detection of such a particle is one of the major challenges of modern cosmology, and possibly physics as a whole, and major efforts have been made to detect it. Nevertheless, no DM candidate has been securely detected to date. The chances for accommodating the speculative DM particle into extensions of the standard model of particle physics vanishes, because evidence for supersymmetry has not emerged at the LHC (e.g. ATLAS Collab., 2011).

Moreover, the cosmological model makes predictions concerning the formation of large- and small-scale structure in the Universe. At the time of photon-baryon-decoupling, the temperature fluctuations of the baryonic matter are of the order of $\approx 10^{-5}$ (Smoot et al., 1992). At that time, the DM density exhibits already larger fluctuations (see above). When the baryonic matter decouples from the photons, the baryons fall into the potentials of the DM, and hierarchical structure formation begins (Lacey and Cole, 1993; see also Padmanabhan, 1993): DM filaments, halos and voids form through subsequent

[1] Note however that the agreement with the quoted observations is generally not unique to the ΛCDM model. See e.g. Angus (2009), and Kroupa (2012, 2014) for further discussions.

merging of smaller, mostly dark structures. The dark halos have a certain shape, which is well described by the Navarro–Frenk–White (NFW) profile (Navarro et al., 1997), and also by the Einasto (1965) profile (e.g. Merritt et al., 2006; Navarro et al., 2010). This shape appears on all scales (with varying parameters), as has been shown in many cosmological simulations. In the dark structures, baryonic gas is trapped, virializes, cools and forms stellar populations and galaxies. From the cosmological point of view, galaxies are therefore very small structures, and they are merely the baryonic, luminous content of much larger DM structures. Their exact properties appear to be rather unimportant in the wider cosmological context.

Nevertheless, for the cosmological model to survive, it is required that the existence of DM is not in disagreement with the dynamical properties of galaxies or small-scale structure in general, independent of the vast success on large scales and the excellent match of the CMB power spectrum. The assumptions being made for the model to explain the large-scale structure, the CMB, and the super-Keplarian rotation curves of galaxies, and large velocity dispersions in clusters of galaxies, must be able to explain the properties of galaxies consistently. This applies in particular to the postulated DM particles. If the observed dynamics of galaxies disproofs the existence of DM, the standard model of cosmology,[2] which is based on GR and the DM hypothesis, fails accordingly.[3] In that case, we would have to reinterpret the dynamics of galaxies as well as cosmology in the view of a revised theory of gravity. This is the subject of Section 1.2, where various galactic scaling relations are discussed in the view of the DM picture and Milgromian dynamics.

Acceleration discrepancy: interpreting the discrepancy as the deviation from GR

The need for additional, non-baryonic mass is observationally well established under the assumption that GR is valid on all scales, and accordingly that the dynamics of galaxies is well approximated by Newtonian dynamics. If this assumption is dropped, the conclusion that DM exists loses validity. Indeed, tests of GR are restricted to much stronger gravitational fields, e.g. the Solar System or binary pulsars (for a review, see e.g. Will, 2006), and the only data that tests the theory on galactic scales are the data that show the described mass or acceleration discrepancy (McGaugh, 2014). At the time at which GR has been formulated, it was not even known what a galaxy is. The assumption that it correctly describes gravity on all scales implies an extrapolation of approximately five orders of magnitude in acceleration, from the outer Solar System with $\approx 10^{-5}\,\mathrm{m/s^2}$ towards galactic scales with $\approx 10^{-10}\,\mathrm{m/s^2}$. Therefore, it seems reasonable to give up the former assumption, and reinterpret the discrepancy in the view of a revised theory of gravity. In this case, a theory of gravity should exist, which ought to explain the observed dynamics from the baryonic matter alone, i.e. without the need of additional, non-baryonic DM, and which ought to be consistent with GR on the scales on which no such discrepancy is found.

Many attempts to solving the mass discrepancy problem have arisen since it has been established. One possible approach that has not been excluded until today is the following ansatz proposed by Milgrom (1983), which has been developed from the following two observations: (a) Rotation curves of galaxies are observed to be asymptotically flat at large radii (see Figure 1.1), and (b) the asymptotic rotation velocities seem to depend on the mass of only the luminous matter content of the galaxies, $L \propto V_{\mathrm{flat}}^4$ (Tully and Fisher, 1977).

These two conditions led to the following symmetry ansatz. Let the equations of motion be scale-invariant under the transformation

$$(\boldsymbol{x}, t) \rightarrow (\lambda \boldsymbol{x}, \lambda t) \tag{1.1}$$

[2] If not stated otherwise, the term 'standard model' refers to the standard model of cosmology.

[3] Independent of whether an alternative or better model exists. For a general discussion about the incommensurability of the standard model and DM-alternatives, see McGaugh (2014).

with $\lambda \in \mathbb{R}$ (Milgrom, 2009d). Consider for example a configuration of point-masses, m_i, located at the positions $\boldsymbol{r}_i(t)$. If the trajectory $\boldsymbol{r}_i(t)$ of the point-mass m_i is a solution of the equations of motion of that system, then the transformed trajectory $\lambda \boldsymbol{r}_i(t/\lambda)$ is a solution as well. This simple symmetry assumption implies already the flatness of the rotation curves around isolated point-masses (Milgrom, 2009d). The assumed scale-invariance is, in the weak-field limit (see below), satisfied by the effective law of gravity described by Milgrom's 1983 formula,

$$\boldsymbol{g} = \nu\left(|\boldsymbol{g}_{\rm N}|/a_0\right)\, \boldsymbol{g}_{\rm N}\,, \tag{1.2}$$

with $\nu(y) \rightarrow y^{-1/2}$ if $y \ll 1$ ("weak field limit"), and $\nu(y) \rightarrow 1$ if $y \gg 1$ ("classical Newtonian regime").[4] $\boldsymbol{g}$ is the 'true' or effective acceleration, and $\boldsymbol{g}_{\rm N}$ is the classical Newtonian acceleration. $a_0 \approx 10^{-10}\,{\rm m\,s^{-2}}$ is Milgrom's constant. In its simplest form, Milgrom's formula reads

$$g = \begin{cases} \sqrt{g_{\rm N}\, a_0} & \text{if } \; g_{\rm N} \ll a_0 \\ g_{\rm N} & \text{if } \; g_{\rm N} \gg a_0\,, \end{cases} \tag{1.3}$$

with $g = |\boldsymbol{g}|$.

Inserting the Newtonian point-mass acceleration field, $\boldsymbol{g}_{\rm N}(\boldsymbol{r}) = -(GM_{\rm b}/r^3)\,\boldsymbol{r}$, in equation (1.3), the acceleration of a point-mass becomes, in the weak-field limit,

$$g(r) = \left(a_0\, g_{\rm N}(r)\right)^{1/2} = \left(\frac{a_0 G M_{\rm b}}{r^2}\right)^{1/2}\,. \tag{1.4}$$

In this field, which is scale-invariant under the transformation defined in equation (1.1), test particles on circular orbits have the radius-independent rotation velocity

$$V_{\rm rot}(r) = |g(r)\, r|^{1/2} = (a_0 G M_{\rm b})^{1/4}\,. \tag{1.5}$$

This equation yields the baryonic Tully–Fisher relation, $M_{\rm b} \propto V_{\rm flat}^4$, which will be discussed in Section 1.2, and accordingly the luminous Tully–Fisher relation if $L \propto M_{\rm b}$.

The heuristic symmetry assumption of equation (1.1) and the (less general) effective law of gravity of equation (1.2) fulfill the stated requirements (a) and (b) by definition for a point-mass. It is however by no means guaranteed that it generally describes the dynamics of galaxies correctly, which is to be tested. The simplest and obvious test is provided by rotation-supported, thin, axisymmetric systems (e.g. spiral galaxies). In such systems, the shape of the effective gravitational potential can be measured indirectly through the circular orbit rotation velocities. If equation (1.2) is a valid effective law of gravity, any rotation curve must precisely be determined by the distribution of baryonic matter alone. That is, the mass or acceleration discrepancy between visible, baryonic mass enclosed within the galactic radius R, $M_{\rm b}(R)$, and the effective dynamical mass[5], $M_{\rm dyn}(R) = V_{\rm obs}^2(R)\, R/G$, must be described by

$$\frac{g(R)}{g_{\rm N}(R)} = \frac{M_{\rm dyn}(R)}{M_{\rm b}(R)} = \frac{V_{\rm obs}^2(R)}{V_{\rm b}^2(R)} = \nu\left(|g_{\rm N}(R)|/a_0\right) \tag{1.6}$$

with a universal ν-function and a universal constant a_0. $g_{\rm N}(R)$ is the Newtonian radial acceleration deduced from the baryonic mass profile, $M_{\rm b}(R)$.[6] $V_{\rm obs}(R)$ is the observed rotation curve. And $V_{\rm b}(R) =$

[4] One can equivalently write: $g_{\rm N} = \mu(|g|/a_0)\, g$, with $\mu(x) \rightarrow x$ if $x \ll 1$, and $\mu(x) \rightarrow 1$ if $x \gg 1$.

[5] The 'dynamical mass' is the mass that would be deduced from the observed rotation velocities or velocity dispersions, when Newtonian dynamics is applied.

[6] In a perfectly flat disk, this is $g_{\rm N} = -GM_{\rm b}(R)/R^2$. More generally, $g_{\rm N}$ is defined by Poisson's equation, $-\nabla \cdot \boldsymbol{g}_{\rm N} = 4\pi G \rho_{\rm b}(\boldsymbol{x})$.

$|g_N(R)\,R|^{1/2}$ is the rotation velocity expected in Newtonian dynamics from the baryons alone (cf. Figure 1.1). This **mass discrepancy–acceleration (MDA) relation** is a strict prediction of Milgrom's law, and has subsequently been observed (Sanders, 1990; McGaugh, 2004; Scarpa, 2006). The MDA relation is discussed in the next section.

Note that equation (1.2) is an *effective law* of gravity and a successful phenomenological scheme for which an underlying theory is needed (Bekenstein and Milgrom, 1984), and it is often misunderstood to be a full theory of gravity. Indeed, if it is applied directly to the equations of motion of a N-body system, that system conserves neither energy nor angular momentum (Milgrom, 1983; see also Famaey and McGaugh, 2012). Milgrom's formula as such is a heuristic scaling law that applies only to highly symmetric systems, e.g., to the rotation curves of axisymmetric, thin disk galaxies, or to the velocity dispersion of spherically symmetric, pressure-supported systems like elliptical galaxies. One can however construct relativistic and non-relativistic theories of gravity yielding Milgrom's formula in symmetric systems (e.g., Bekenstein and Milgrom, 1984; Bekenstein, 2004; Milgrom, 2009a, 2010). These aspects are elaborated in Section 1.3. To avoid further misunderstandings, the work of Milgrom (1983) is referred to as the *pristine formulation* of Milgromian dynamics, and equations (1.2) and (1.3) are referred to as *Milgrom's formula* or *law*.

The 'missing acceleration' approach appears to be more elegant than the 'missing mass' interpretation, because it preserves the predictability of the gravitational fields from the distribution of visible matter alone. If we know the exact baryonic matter density distribution, the applicable theory of gravity (which ever it may be) predicts the according gravitational potential. For example, if the mass density distribution of a rotating disk galaxy is measured, the theory strictly predicts the rotation curve $V(R)$. Comparing those predictions to the observed rotation curves, $V_{\rm obs}(R)$, provides a unique test in every single galaxy.

This is in strong contrast to the standard GR-DM framework, in which the hypothesized DM component by definition fills the gap between the galactic dynamics expected from the theory, in that case Newtonian dynamics without DM, and the observed dynamics. Predicting the kinematics for an individual observed galaxy is therefore not possible, and the DM-hypothesis is, for the same reason, not testable on an object-by-object basis. In practice, the distribution of the postulated DM is indirectly "measured", i.e., it is inferred from the observed dynamics. If we want to explore whether the DM-hypothesis can explain the mass discrepancy in galaxies consistently, or if rather a general revision of our understanding of gravity is required, it is necessary to see the overall picture: we have to analyze the properties of the mass or acceleration discrepancy, and, more generally, galactic dynamics in a statistical manner. This is the subject of the section below.

1.2 Scaling relations in disk galaxies

The two different frameworks, Newtonian dynamics (as the non-relativistic limit of GR) with DM on the one hand and revised gravity without DM on the other hand, have very different implications on the dynamics of galaxies. In the DM picture, galaxies are embedded in pressure-supported DM halos that commonly make up the major fraction of the total galactic mass and thus the dominant part of the galactic potential. Contrary to rotating disks, pressure-supported halos are very stable and not particularly sensitive to instabilities due to self-gravity, therefore providing the galactic disk with a robust potential and accordingly preventing disk instabilities (e.g., Toomre, 1964; Ostriker and Peebles, 1973). The galactic potential is defined by the sum of those two distinct matter components, which interact with each other only gravitationally. In the Milgromian framework, on the other hand, the potential is

The same applies to the estimate of $M_{\rm dyn}(R)$.

defined by the baryonic matter alone.

If the mass discrepancy ought to be explained by the existence of non-baryonic DM particles that interact only gravitationally, then the properties of the distribution of dark and baryonic matter should depend on the individual formation histories of the individual galaxies, and tight correlations between the dark and the baryonic matter are not expected globally. On the other hand, if the mass discrepancy should be mimicked by a universal force law and the gravitational potential is defined by the baryons alone, we expect a tight correlation between the baryonic matter and the observationally indirectly inferred distribution of the apparently missing mass. In the following, it is shown that the latter is the case for galaxies.

A number of galactic scaling relations are known to date, most prominently the **Tully-Fisher relation** (Tully and Fisher, 1977). It relates the asymptotically flat rotation velocity to the total luminosity of rotation-supported objects, $L \propto V_{\rm flat}^4$. That relation holds for gas-poor galaxies, but breaks down for gas-rich objects. However, a tight correlation persists if the total baryonic mass, $M_{\rm b}$, is considered instead of the total luminosity:

$$M_{\rm b} \propto V_{\rm flat}^4 \tag{1.7}$$

(see Figure 1.2). This relation is known as the **baryonic Tully–Fisher relation** (BTFR, McGaugh et al., 2000), and relates the asymptotic flat rotation velocity, $V_{\rm flat}$, to only the baryonic mass content of the galaxy.[7] The BTFR ranges over more than five decades of mass (e.g., Verheijen, 2001; McGaugh, 2011b, 2012) and covers all kinds of rotation-supported galaxies: gas-rich galaxies as well as gas-poor ones, and high surface brightness (HSB) galaxies as well as those having a low surface brightness (LSB). Even tidal dwarf galaxies, which generally cannot harbor a significant amount of DM (Barnes and Hernquist, 1992; Gentile et al., 2007; Bournaud, 2010), obey this relation (McGaugh and Wolf, 2010). In the standard model, the DM, which constitutes the largest fraction of galactic mass, must therefore carefully be distributed to yield, depending on the total baryonic mass, the correct asymptotic rotation velocity, as has been detailed and discussed by McGaugh et al. (2000), McGaugh (2008a), and also by Famaey and McGaugh (2012). Years ago, it has been thought that the effective surface density of baryonic and dark matter is nearly universal in all disk galaxies (Freeman, 1970). To date, we know that this is not the case, as many LSB galaxies have been observed, and none of them departs significantly from the BTFR (Begum et al., 2008). This imposes a fine-tuning challenge on the DM model (McGaugh, 2005a).

In cosmological simulations, $M_{\rm b} \propto V_{\rm flat}^3$ is found (Steinmetz and Navarro, 1999, see the dashed line in Figure 1.2). To explain the difference between the data and the numerical finding, it has to be assumed that not the total, but only a fraction, $0 < f_{\rm d} \leq 1$, of the total galactic baryonic mass content, $M_{\rm b,tot}$, is actually detected, in order to 'correct' the baryonic mass to $M_{\rm b,tot} = M_{\rm b,det}/f_{\rm d}$ (McGaugh et al., 2010). However, if this would be the case, then the detected baryon fraction, $f_{\rm d}$, would have to depend systematically on the DM halo mass, as has been demonstrated by McGaugh et al. (2010). This is however not plausible, and leaves basically two possible conclusions: either (i) the simulations are unrealistic in the sense of being incomplete, or (ii) they contradict the observations. More recent results of the Illustris simulations, focussing on the formation and evolution of galaxies in the cosmological context, show better agreement with the observed BTFR, but at the cost of introducing baryonic feedback processes whose intensities are scaled *artificially* with the DM halo mass (Vogelsberger et al., 2014).[8] I.e., the

[7] A correlation similar to the BTFR is known for pressure-supported galaxies: the **Faber–Jackson relation**, which relates the baryonic mass to the velocity dispersion, $Ga_0 M_{\rm b} \propto \sigma^4$ (Faber and Jackson, 1976). In that case, the fine-tuning problematics are similar to those described above (Sanders, 2010).

[8] In the Illustris simulations, the stellar wind velocities of the stellar supernova feedback are scaled with the local DM halo (1-dim.) velocity dispersion, $\propto 3.7\,\sigma_{\rm DM}^{\rm 1D}$, and thus with the DM halo mass, $\sigma_{\rm DM}^{\rm 1D} \propto (M_{\rm DM})^{1/2}$.

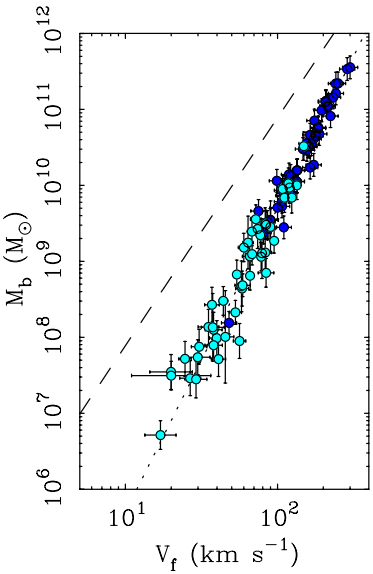

Figure 1.2: The baryonic Tully–Fisher relation (BTFR) relates the baryonic mass of a galaxy, M_b, to its asymptotic flat rotation velocity, V_f. The light blue dots represent gas-dominated galaxies ($M_\mathrm{gas} > M_*$), the dark ones represent those with $M_\mathrm{gas} < M_*$. The dotted line shows the prediction of Milgromian dynamics, $M_\mathrm{b} = (a_0 G)^{-1} V_\mathrm{flat}^4$, with $a_0 = 1.2 \times 10^{-10}\,\mathrm{m\,s^{-2}}$. The dashed line is a prediction of the standard CDM-based model (Steinmetz and Navarro, 1999). The mismatch between the data and the ΛCDM prediction constitutes a fine-tuning challenge to the standard CDM-based model, which is detailed in the text. (This figure has been reproduced from and with the permission by Famaey and McGaugh, 2012)

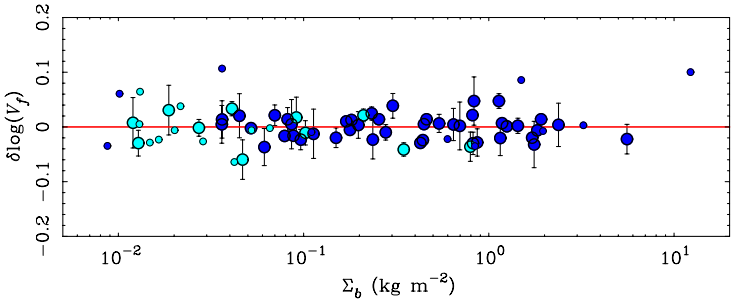

Figure 1.3: The residuals of the BTFR as function of the charateristic baryonic surface density, $\Sigma_\mathrm{b} = 0.75 M_\mathrm{b}/R_\mathrm{p}^2$, obtained within the galactic radius R_p, at which the baryonic rotation curve, $V_\mathrm{b}(R)$, peaks. If the baryonic matter contributes a significant fraction to the total (baryonic plus dark) mass, a systematic deviation from the BTFR with characteristic surface density, Σ_b, should be visible. However, no such deviation is found. That adds to the fine-tuning problem in the DM-model of galaxies, because it means that the hypothesized DM has to be *carefully* distributed to just compensate the effect of varying baryonic surface density. (This figure has been reproduced from and with the permission by Famaey and McGaugh, 2012)

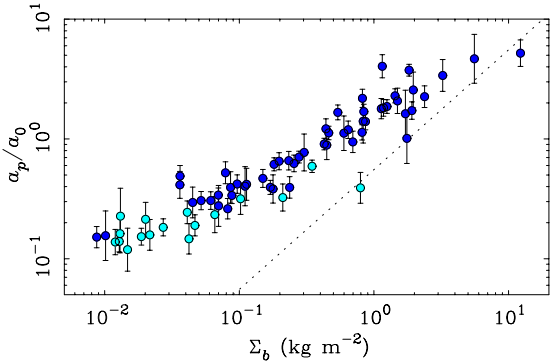

Figure 1.4: The acceleration–surface density relation in rotation-supported galaxies. The radial acceleration, $a_\mathrm{p} = V_\mathrm{p}^2/R_\mathrm{p}$, is plotted vs. the characteristic surface density of baryonic matter, Σ_b. The dashed line is the Newtonian acceleration expected from only the visible mass ($a_\mathrm{p} \propto \Sigma_\mathrm{b}$; this is however only an approximation, and does not take into account the disk thickness or the bulge). There is a clear correlation between the galactic potentials and the resulting radial accelerations and the baryonic mass contribution. This shows that, in the DM-model, the baryonic matter indeed contributes significantly to the rotation curve. That finding, as such, is not surprising, because it is expected that the baryons contribute a non-neglectable fraction to the total galactic mass. The correlation however confirms the fine-tuning problematic pointed out in Figure 1.3. (This figure has been reproduced from and with the permission by Famaey and McGaugh, 2012)

agreement with the observational data is artificially induced by implementing *by hand* the fine-tuning requirements pointed out by McGaugh et al. (2010). It should also be noted that these simulations exhibit a large scatter in the simulated BTFRs, while the observed BTFR is compatible with having zero intrinsic scatter (McGaugh et al., 2000). The small scatter is one of the outstanding features of this relation, because it is unclear how the inherently chaotic processes in the individual galaxy formation histories can lead to this very ordered scaling relation in the DM model. Therefore, it seems conceivable that not DM, but rather an effective law of gravity in the form of equation (1.2) accounts for the BTFR, and that baryonic feedback processes like the stellar winds from SN feedback play only a minor role. But this is speculative and has not been demonstrated yet, and will be part of the future work with the galaxy simulation code presented in Chapter 4. (See also the discussion by Kroupa, 2014.)

What further adds to the DM fine-tuning problem is the fact that V_flat does not vary systematically with the baryonic matter surface density, Σ_b, as is shown in Figure 1.3 (McGaugh, 2005a). In thin, axisymmetric systems, the Newtonian acceleration is $g_\mathrm{N} = GM_\mathrm{b}(R)/R^2 = G\pi\Sigma_\mathrm{b}(R)$, i.e. proportional to the baryonic surface density. If the baryonic mass contributes a significant, although not necessarily the largest fraction to the total galactic mass, a systematic deviation from the BTFR with varying surface density should be visible in the data, depending on the ratio of baryonic to dark mass. But, a systematic deviation from the BTFR is not found. As a consequence, additional fine-tuning is required to just compensate this effect.

Now, because one does not observe the expected systematic deviation from the BTFR with varying baryonic matter surface density, one could think that the proportional contribution of the baryons to the galactic potential is very small, $\Sigma_\mathrm{b} \ll \Sigma_\mathrm{b+DM}$, thereby avoiding this particular fine-tuning aspect. This is however not the case, as demonstrated by the **surface density–acceleration relation** (Figure 1.4), which relates the characteristic surface density of galaxies, $\Sigma_\mathrm{b} = 0.75M_\mathrm{b}/R_\mathrm{p}^2$, obtained within the galactic radius R_p at which the baryonic rotation curve, $V_\mathrm{b}(R)$, peaks (cf. Figure 1.1), to the radial acceleration

at the same radius, $a_\mathrm{p} = V_\mathrm{p}^2/R_\mathrm{p}$. That correlation clearly confirms the highlighted issue.

The existing fine-tuning issues are further established by Renzo Sancisi (2004), who notices that "for any feature in the luminosity profile there is a corresponding feature in the rotation curve and vice versa." That observation became known as **Renzo's rule**. It adds another interesting point to the fine-tuning discussion, because features in the luminosity profiles of galaxies, such as bumps and wiggles, should be smeared out in the rotation curves, as the DM halos dominate the galactic potentials and thus the shapes of the rotation curves. This, however, is apparently not the case, including in LSB galaxies, which generally reside in gravitational potentials displaying extraordinary high mass discrepancies even at the galactic centers (e.g. Strigari et al., 2008). This points towards the need of *local* fine-tuning. (For further discussions on these scaling relations, see the very detailed review of Famaey and McGaugh, 2012, and also Trippe, 2014).

Up to this point, only single, global quantities of galaxies have been discussed (L, M_b, V_flat, a_p, Σ_b). It nevertheless becomes clear that the systematics between these quantities hint at an extensive fine-tuning between dark and luminous matter. To obtain better constraints on the properties of the required fine-tuning, one has to look for dependencies between the distribution of ordinary and DM in every galaxy individually, and to compare the individual results to each other.

The mass discrepancy–acceleration relation

As we will see below, the above discussed relations of galactic properties can be summarized by a single, local relation between the distribution of baryons and the mass discrepancy.

The DM hypothesized in the standard model cannot be observed directly. In order to compare the distribution of DM to that of the baryons and to find possible connections, we however have to quantify its distribution in some way. The available observables are (i) the distribution of luminous matter and the according cumulative mass profile, $M_\mathrm{b}(R)$, and (ii) the dynamics, in spiral galaxies in form of the rotation curves, $V_\mathrm{obs}(R)$. From these observables, we can derive several other useful quantities to compare with. From the rotation curve, we obtain the cumulative profile of the *effective* dynamical mass,

$$M_\mathrm{dyn}(R) = R\frac{V_\mathrm{obs}^2(R)}{G}\,, \tag{1.8}$$

that is, in the standard model, the sum of luminous and dark mass. We thereby make the assumption that the DM is distributed spherically symmetrical. We can estimate the centripetal acceleration as a function of the galactic radius,

$$a_\mathrm{R}(R) = -\frac{\partial\Phi(R)}{\partial R} = -\frac{V_\mathrm{obs}^2(R)}{R}\,, \tag{1.9}$$

which equals to the gradient of the effective gravitational potential, $\Phi(R)$. On the other hand, the radial (Newtonian) acceleration expected from the distribution of baryons, $M_\mathrm{b}(R)$, would be

$$a_\mathrm{R,b}(R) = -G\frac{M_\mathrm{b}(R)}{R^2}\,. \tag{1.10}$$

If the mass discrepancy, $M_\mathrm{dyn}(R)/M_\mathrm{b}(R)$, is plotted as a function of the acceleration, $a_\mathrm{R,b}(R)$, for all available galaxies, a tight correlation between the mass discrepancy and the gravitational potential becomes visible (Sanders, 1990; McGaugh, 2004; Scarpa, 2006). This is shown in Figure 1.5 (bottom panel). That relation summarizes all observations discussed before.

This fully empirical correlation shows that the distribution of DM is indeed locally connected to that of the baryonic matter, i.e. at every single point (or galactic radius) in the individual galaxies. Or, put

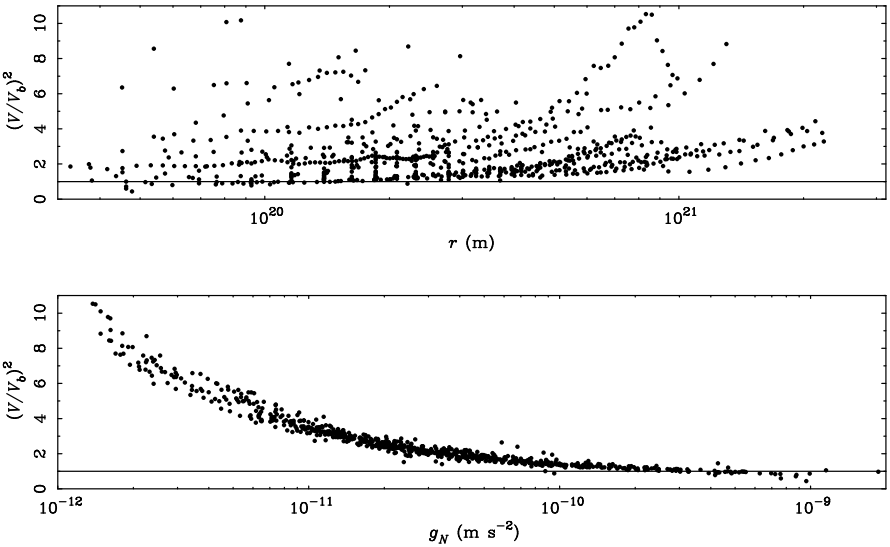

Figure 1.5: The mass discrepancy–acceleration (MDA) relation of 60 rotation-supported galaxies is shown (736 individual data points in total, see McGaugh, 2004). The plot shows the mass discrepancy, i.e. the ratio of effective, dynamical mass (that is baryonic plus dark mass in the standard model) to baryonic mass, $V^2(R)/V_b^2(R)$ (see equation 1.6), as function of the galactic radius, R, (top panel) and as function of the Newtonian acceleration, $g_N(R) = GM_b(R)/R^2$, (bottom panel) for a sample of spiral galaxies. While there is global no correlation visible if the mass discrepancy is plotted vs. the galactic radius, there is a clear correlation between the mass discrepancy and the Newtonian acceleration, which is computed from the baryons alone. This correlation agrees with Milgrom's law (equation 1.2), $g/g_N = V_{obs}^2/V_b^2 = \nu(|g_N|/a_0)$. (This figure has been reproduced from and with the permission by Famaey and McGaugh, 2012)

another way, the distribution of DM is a function of the baryonic matter, in the form

$$\frac{M_{DM}(R)}{M_b(R)} = f\left(a_{R,b}(R)\right) . \tag{1.11}$$

The available data agrees with $f\left(a_{R,b}(R)\right) = \nu\left(|a_{R,b}(R)|/a_0\right) - 1$, with $\nu(y) \to y^{-1/2}$ if $y \ll 1$, and $\nu(y) \to 1$ if $y \gg 1$. That is the key prediction of Milgromian dynamics (equation 1.6).

This relation between the observationally deduced mass discrepancy and the distribution of baryonic matter leaves basically the following possible conclusion:

(i) It points towards the existence of a universal law of gravity that mimics the potential of the hypothetical DM. Although the data can only test and generally not prove the existence of such a law,[9] the fact that the present data do not falsify this possibility strongly emphasizes the importance of considering today's understanding of gravity as being incomplete.

(ii) Alternatively, if one nevertheless wants to retain the standard, DM-based model to understand the

[9] The same is true for any other theory, e.g. GR.

small-scale structure, the distribution of DM mimics the effective force law of equation (1.2), and the appearance of this law must be understood in the context of galaxy formation and evolution. Today, the speculation is that baryonic feedback processes are responsible and account for the fine-tuning associated with that law.[10] Understanding the details of the formation of galaxies with the help of baryonic feedback processes requires the modeling of the formation of the DM halos, the subsequent trapping of gas in their gravitational potentials, and finally the star formation including various stellar feedback processes. In any case, there is no reason why the mass discrepancy should correlate with any physical scale (e.g. Famaey and McGaugh, 2012). The formation of DM halos in ΛCDM cosmological simulations has been examined extensively in the recent decades. It is noticed and widely accepted that the forming DM halos share a common shape, which is shown to be scale-free (Navarro et al., 1997): dark halos possess very similar profiles on very different scales, but with varying parameters (length scale, total mass). Baryon-free CDM haloes are thus excluded to exhibit the observed behavior, including the acceleration scale a_0. On the other hand, the baryonic feedback processes, which are hoped to come to the rescue, depend on the individual galaxy formation histories. Because the galaxies underlying the data of Figure 1.5 cover a *wide* range of very different properties ($V_{\rm flat} = 50 \ldots 300\,{\rm km\,s^{-1}}$, $L_{\rm B} = 5 \times 10^7 \ldots 2 \times 10^{11}\,{\rm L_\odot}$, the disk scale lengths cover $0.5 \ldots 13\,{\rm kpc}$, and the gas fractions $f_{\rm gas} = 0.07 \ldots 0.95$; for details see McGaugh, 2004), it seems very unlikely, if not impossible, that the relation plotted in Figure 1.5 emerges from the individual galaxy formation processes. Keeping that and the persistent success of Milgrom's empirical law in galaxies in mind, a possibly wrong conclusion is that the complexity of baryonic physics hinders us from understanding the dynamics of galaxies (see also the related discussion in Kroupa, 2014).

In either case, the MDA relation, which has been predicted and is excellently described by Milgrom's empirical law, is observationally evident in this data and has to be understood in one way or the other. Independent of the existence or non-existence of CDM, the great success of equation (1.2) warrants the research on Milgromian dynamics. Even if it turns out that no fundamental theory leading to the discussed phenomenology exists, it would persist as the phenomenon it is, and would tell us something fundamental about the formation and evolution of galaxies and the nature of DM in general.

However, some issues with the simple ansatz by Milgrom (1983) do exist. For example, if Milgrom's law is applied to clusters of galaxies, additional mass is still required to explain the observed velocity dispersions of the galaxies (e.g. Sanders, 1999). This missing-mass-residual is of the order of the observed baryonic mass, i.e. small compared to the mass discrepancy derived from Newtonian dynamics, which exceeds the baryonic cluster mass typically by a factor of $\approx 6 \ldots 8$ (e.g. Giodini et al., 2009). Various possible explanations exist (Famaey and McGaugh, 2012): (i) The residual missing mass could be baryonic dark matter, meaning that undetected baryons in the center of the galaxy clusters could account for the discrepancy, such as diffuse intra-cluster gas. This could be plausible, because only gas-rich clusters are affected by this issue, and it is estimated that $\approx 30\%$ of the baryons produced by the BBN are still unobserved to date (Shull et al., 2012). (ii) Also non-baryonic dark matter could account for the residual mass discrepancy, e.g. neutrinos with a hypothetical mass of $\approx 2\,{\rm eV}$ (e.g. Sanders, 2007), a limit that agrees with experimental constraints of currently $\lesssim 2.2\,{\rm eV}$ for the mass of the electron neutrino (Kraus et al., 2005). Constraints on the neutrino mass limit from cosmological structure formation in the ΛCDM model ($\approx 1.5\,{\rm eV}$, Nieuwenhuizen, 2009) do not apply in this case. (iii) The discrepancy could also lead to the conclusion that Milgromian dynamics is an incomplete paradigm, and an additional scale, that of galaxy clusters, is required to be included. Milgrom's law as such is an

[10] Note however that there may be also other alternatives which consider DM with properties different to those of the CDM claimed by the ΛCDM model, e.g. self-interacting DM (Spergel and Steinhardt, 2000). Also gravitational permittivity of a gravitationally polarizable medium could, theoretically, lead to the observed phenomenology (Dipolar DM, Blanchet and Bernard, 2014). These theories however have their own problems.

effective scaling relation, and it is speculated that it emerges from more fundamental physical principles (see next section). Because we have explored only 'effective' or 'approximate' theories so far, it is imaginable that the yet unexplored fundamental theory, if existing, predicts a scaling law for galaxy cluster scales that deviates from Milgrom's 1983 law applying to galaxy scales. Or, (iv) it disproves not only Milgrom's law in galaxy clusters, that is argument iii, but Milgromian dynamics in general.

Although not supported with facts, the possible conclusions (i) and (ii), and even (iii), cannot be excluded. In the case of (iv), the failure of Milgrom's formula in clusters of galaxies does not weaken its unique success on galaxy scales, which then still has to be understood.

However, the confirmation of Milgrom's law in the static tests provided by the rotation-supported stellar systems described above justifies and demands making the step from static to dynamical modeling of galaxies, to see whether Milgromian dynamics can survive the tests provided by dynamical stellar systems. To do so, and to explore the possible limits of the theory, we need to consider full theories of gravity which can be implemented in simulation codes, to test the theory in as many systems as the standard model has been tested. In the coming section, it is explained how such theories can be constructed, and how they can be used to develop our understanding of galaxies in such a framework.

1.3 Milgromian dynamics theories

It has already been emphasized that Milgrom's formula, equation (1.2), is an empirical scaling law that applies to highly symmetric systems only, and that it is not yet a theory of gravity, because this phenomenological law conserves neither energy nor momentum, if it is applied directly to the equations of motion of a self-gravitating system. One can, however, construct field theories of gravity, relativistic and non-relativistic, that are energy and momentum conserving, and scale-invariant in the sense of equation (1.1) in the weak-field limit, and thus make the basic predictions of the pristine formulation of Milgromian dynamics. By analogy with Newtonian dynamics and GR, we start from an action,

$$S = \int_{t_1}^{t_2} L(\boldsymbol{x}, \dot{\boldsymbol{x}}, t)\, \mathrm{d}t\,, \tag{1.12}$$

(e.g., Bekenstein and Milgrom, 1984; Bekenstein, 2004; Milgrom, 2010; see also Famaey and McGaugh, 2012; Milgrom, 2014). Making use of the least action principle, one obtains (i) the Euler-Lagrange equations and thus the equations of motion, and (ii) the Poisson equation.

For a Newtonian, non-relativistic, self-gravitating system, the Lagrangian L generally reads

$$L = L_{\rm kin} + L_{\rm in} + L_{\rm grav} = \int \rho(\boldsymbol{x})\, \frac{\dot{\boldsymbol{x}}^2}{2}\, \mathrm{d}^3x \;-\; \int \rho(\boldsymbol{x})\, \phi_{\rm N}(\boldsymbol{x})\, \mathrm{d}^3x \;-\; \frac{1}{8\pi G} \int |\nabla \phi_{\rm N}(\boldsymbol{x})|^2 \;\mathrm{d}^3x \tag{1.13}$$

(e.g. Milgrom, 2014) with the matter density $\rho(\boldsymbol{x})$ and the Newtonian potential $\phi_{\rm N}(\boldsymbol{x}) = -G \int \rho(\boldsymbol{x}')/|\boldsymbol{x}' - \boldsymbol{x}|\, \mathrm{d}^3x'$. The first term, $L_{\rm kin}$, constitutes the kinetic energy, and the second plus third term, $L_{\rm in} + L_{\rm grav}$, the potential energy of the whole system. Varying S with respect to the position space, $\boldsymbol{x}$, one gets the equations of motion, $\boldsymbol{g}_{\rm N} = \ddot{\boldsymbol{x}} = -\nabla\phi_{\rm N}$. On the other hand, by varying S with respect to the potential, $\phi_{\rm N}(\boldsymbol{x})$, one obtains the Poisson equation, $\nabla^2\phi_{\rm N} = 4\pi G\rho(\boldsymbol{x})$.

To derive, analogously, a Milgromian dynamics theory, the Lagrangian is modified. The scale-invariance of the equations of motion is attained if the action, S, has a well-defined scaling dimension, $\xi \in \mathbb{N}$, such that under the transformation $(\boldsymbol{x}, t) \rightarrow \lambda(\boldsymbol{x}, t)$, the action scales according to $S \rightarrow \lambda^\xi S$ (Milgrom, 2014). This is not the case for the standard Lagrangian of equation (1.13), where the first

and the second term have the scaling dimension $\xi = 1$, and the last term has $\xi = 2$ (Milgrom, 2014). Therefore, one has the choice to either (i) adapt the first and the second term of equation (1.13), $L_{\rm kin}$ and $L_{\rm in}$, to ensure $\xi = 2$. The results are summarized as **modified inertia** theories. Or (ii) the third term, $L_{\rm grav}$, is adapted to enforce $\xi = 1$, which yields **modified gravity** theories.

Changing the inertia or the gravity are the two very basic approaches to Milgromian dynamics. The modified inertia ansatz generally leads to non-local theories (Milgrom, 1994), leading to complications if those theories are applied to systems that are not highly symmetric. However, this is generally not the case for the modified gravity theories, of which a variety of applicable theories already exist. The first modified gravity theory has been the 'aquadratic Lagrangian' formulation (AQUAL) by Bekenstein and Milgrom (1984), which is described below as an example of non-relativistic modified gravity theories. Another non-relativistic theory is the quasi-linear formulation (QUMOND) recently developed by Milgrom (2010), which is very practical for use in N-body codes, and is detailed below as well. Like in Newtonian dynamics, the field equations of the non-relativistic modified gravity theories are generally static, i.e. not time-dependent. Keep however in mind that, although the modified gravity theories are technically less complicated, it is also possible that the concept of modified inertia might be the more fundamental approach to the Milgromian dynamics phenomenon (e.g. Milgrom, 1999).

By developing the so called Tensor-Vector-Scalar (TeVeS) theory, Bekenstein (2004) has been the first to show that relativistic theories exist. TeVeS uses a metric whose action is the standard Einstein-Hilbert action, and which is extended by an auxiliary vector field and a scalar field. Further relativistic theories exist, e.g. BIMOND (Milgrom, 2009a), in which gravity is described by two metrics. However, because the collisionless dynamics of galaxies are generally non-relativistic, standard simulation codes treat gravity with classical Newtonian dynamics rather than GR. And for the same reason, the focus is laid on non-relativistic theories here.

In general, an infinite number of theories exist leading to the described scale-invariance in the weak-field limit and to Milgrom's law (a detailed list of the most prominent theories is provided in the review by Milgrom, 2014). The Milgromian dynamics field theories described here are, like Newtonian dynamics, not built upon deeper, new fundamental physics. They all hinge on transition functions (e.g. $\mu(x)$, $\nu(y)$), which smoothly connect the weak-field limit or Milgromian regime ($g \ll a_0$) to the opposite Newtonian limit ($g \gg a_0$).

A fundamental physical approach to the Milgromian dynamics paradigm could be based on vacuum effects having an effect on the inertia that are represented by the first term of the action of equation (1.12), as has been suggested by Milgrom (1999). The vacuum is also held to account for dark energy, which is represented by the cosmological constant Λ in Einstein's field equations, and appears to be correlated with Milgrom's constant, $a_0 \approx c(\Lambda/3)^{1/2}$ (Milgrom, 1999). However, although this could hint a possible connection, no dynamical effects leading to Milgromian dynamics have been demonstrated to date (Milgrom, 2014). The described theories are nevertheless very useful as 'effective' or 'approximate' theories in the same way as Newtonian dynamics has been for most astrophysical problems. Two of them are outlined below.

While in general the individual theories can have different properties, they all share the predictions derived from the basic tenets of Milgrom (1983). These common predictions are usually entitled *Milgrom's 'Kepler-laws'*, or *Milgrom's laws of galactic dynamics*, and are listed and discussed by Milgrom (2002, 2008), Sanders and McGaugh (2002), and Famaey and McGaugh (2012). They cover rotation- and pressure-supported dynamical systems, and are supported by observational data. The latter is not surprising, because Milgrom's law, from which the predictions follow, is empirically evident in form of the MDA relation. However, these predictions highlight the different roles played by a_0. The most interesting point about these roles is that they appear, in view of the standard DM model, completely *independent* of each other, but can *all* be unified by Milgrom's 1983 formula. Besides the predictions

that have already been discussed in this chapter, the role of a_0 as a transition acceleration is emphasized, and the therewith connected transition surface density, a_0/G, which is, in the Milgromian framework, critical for the stability of isolated disks: below (Milgromian regime) and above (Newtonian regime) that surface density, the dynamics and thus the stability properties of isolated disks are different. Observationally, that critical surface density is evident as the maximum central surface density of HSB galaxies (McGaugh, 1996; Famaey and McGaugh, 2012), which is otherwise known as the Freeman (1970) limit. The existence of such a limit is not explained by the standard model, in which the galactic disk is stabilized by a DM halo, which is generally thought not to prefer a particular scale, as has been discussed before. Moreover, the transition acceleration a_0 is also imprinted in spheroidal systems, which exhibit a_0 as the typical effective acceleration at the effective radius (Sanders and McGaugh, 2002). This is because these systems are usually well described by quasi-isothermal[11] spheres (ISs). In the Milgromian framework, ISs have a finite mass, and a radial density profiles that is $\propto r^{-2}$ at radii at which the effective acceleration is above a_0 (Newtonian IS), and $\propto r^{-4}$ in the opposite, weak-field limit. The radius that separates both regimes happens to be similar to the effective radius, and consequently, the acceleration at that radius is always of the order of a_0.

"AQUAL" formulation (Bekenstein and Milgrom, 1984)

The obvious and simplest modified gravity formulation of Milgromian dynamics is based on the Lagrangian with a gravity term defined by

$$L_{\rm grav} \equiv -\frac{1}{8\pi G}\int a_0^2\, F\left(\frac{|\nabla\Phi(\boldsymbol{x})|^2}{a_0^2}\right) {\rm d}^3x\,, \tag{1.14}$$

(see Bekenstein and Milgrom, 1984) with the Milgromian potential $\Phi(\boldsymbol{x})$ and the function $F(z)$. To ensure scale-invariance in the weak field limit, and compliance with Newtonian dynamics in the $g \gg a_0$ regime, i.e. to recover Milgrom's effective law of gravity (equation 1.2), we ensure ${\rm d}F(z)/{\rm dz} = \mu(z^{1/2})$, i.e. $F(z) \rightarrow 2/3\, z^{3/2}$ if $z \ll 1$, and $F(z) \rightarrow z$ if $z \gg 1$. Varying S with respect to $\Phi(\boldsymbol{x})$, this ansatz leads to the modified Poisson equation

$$\nabla\cdot\left(\mu\left(\frac{|\nabla\Phi(\boldsymbol{x})|}{a_0}\right)\nabla\Phi(\boldsymbol{x})\right) = 4\pi G\rho(\boldsymbol{x})\,, \tag{1.15}$$

with the (baryonic) matter density $\rho(\boldsymbol{x})$. Because the matter term of the Lagrangian has not been touched, the equations of motion remain $\boldsymbol{g} = \ddot{\boldsymbol{x}} = -\nabla\Phi(\boldsymbol{x})$, in that case with the Milgromian potential $\Phi(\boldsymbol{x})$.

Equation (1.15) is a non-linear elliptical partial differential equation, and a relaxation scheme is needed to solve it for an evolving N-body system in a grid code. It is not possible to solve the equation applying the widely used discrete FFT-methods (general aspects of Milgromian dynamics N-body codes are discussed in the next section). The difficulty of numerically solving equation (1.15) is discussed in Section 1.4, and is one of the primary reasons for the small number of AQUAL gravity codes available to date.

[11] The term quasi-isothermal is used, because ISs have different density profiles in Newtonian and Milgromian dynamics, and the term 'IS' is classically used for Newtonian ISs, which have a matter density profile $\propto r^{-2}$.

Quasi-linear formulation (QUMOND, Milgrom, 2010)

The quasi-linear formulation of Milgromian dynamics (QUMOND, see also sections 2.2, 3.2, 4.2) makes use of the Newtonian potential, $\phi_{\rm N}(\boldsymbol{x})$, as an auxiliary potential. The term $L_{\rm grav}$ is defined by

$$L_{\rm grav} \equiv -\frac{1}{8\pi G}\int\left(2\nabla\Phi\cdot\nabla\phi_{\rm N} - a_0^2\,Q\left(\frac{|\nabla\phi_{\rm N}|^2}{a_0^2}\right)\right)\mathrm{d}^3x\,, \tag{1.16}$$

with the transition function $\mathrm{d}Q(z)/\mathrm{d}z = \nu(z^{1/2})$. To recover Milgrom's law, equation (1.2), we define $Q(z) \rightarrow 4/3\,z^{3/4}$ if $z \ll 1$, and $Q(z) \rightarrow z$ if $z \gg 1$.

Applying the least action principle, this Lagrangian leads to the following quasi-linear Poisson equation:

$$\nabla^2\Phi(\boldsymbol{x}) = 4\pi G\left(\rho_{\rm b}(\boldsymbol{x}) + \rho_{\rm ph}(\boldsymbol{x})\right)\,, \tag{1.17}$$

with the Milgromian potential $\Phi(\boldsymbol{x})$, the baryonic matter density $\rho_{\rm b}(\boldsymbol{x})$, and the 'phantom dark matter' (PDM) density

$$\rho_{\rm ph}(\boldsymbol{x}) = \frac{\nabla\cdot\left[\bar{\nu}\left(|\nabla\phi(\boldsymbol{x})|/a_0\right)\nabla\phi(\boldsymbol{x})\right]}{4\pi G}\,, \tag{1.18}$$

which is a function of the Newtonian potential and accordingly of the distribution of baryonic matter. We define $\bar{\nu}(x) \equiv \nu(x) - 1$. The PDM density, $\rho_{\rm ph}$, is the matter density that would, in Newtonian gravity, yield exactly the additional gravitational potential, $\Phi_{\rm ph}$, that is predicted by Milgromian dynamics, so that the full Milgromian potential, Φ, can be divided into a Newtonian and an additional, Milgromian part,

$$\Phi = \phi_{\rm N} + \Phi_{\rm ph}\,, \tag{1.19}$$

with $\nabla^2\phi_{\rm N}(\boldsymbol{x}) = 4\pi G\rho_{\rm b}(\boldsymbol{x})$, and $\nabla^2\Phi_{\rm ph}(\boldsymbol{x}) = 4\pi G\rho_{\rm ph}(\boldsymbol{x})$.

The phantom matter is not real matter, it is a mathematical expression that allows solving the Poisson equation (1.17) with only linear differential equations (the two Poisson equations above) and one additional, algebraic step (equation 1.18), giving this formulation the attribute "quasi-linear". This has a significant advantage for the practical use in simulation codes, because it allows making use of the already available Newtonian Poisson solvers implemented in the available state-of-the-art collisionless N-body codes, as described in detail in Chapter 4.

Because the Newtonian potential, $\phi_{\rm N}$, is used as an auxiliary potential, the QUMOND formulation provides a very illustrative approach to the Milgromian framework. The PDM density is exactly the matter density that would, in the standard model of cosmology, be interpreted as missing or dark matter, and provides the Milgromian framework with a useful classical analogue.

In Figure 1.6, the PDM density distribution of an example disk model is shown and compared to the effective, spherical DM halo that an observer using the ΛCDM-model as working hypothesis would deduce from the observed baryonic matter distribution, $M_{\rm b}(R)$, and the observed rotation velocity,

$$V^2_{\rm obs}(R) = \nu\left(\frac{V^2_{\rm b}(R)/R}{a_0}\right)V^2_{\rm b}(R)\,, \tag{1.20}$$

predicted by Milgrom's law (equation 1.2). The spherical DM halo density deduced from the rotation curve would be

$$\rho_{\rm DM,diff}(R) \approx \frac{1}{4\pi R^2}\frac{\partial}{\partial R}\Big(\underbrace{\frac{R}{G}V^2_{\rm obs}(R)}_{M_{\rm dyn}(R)} - \underbrace{\frac{R}{G}V^2_{\rm b}(R)}_{M_{\rm b}(R)}\Big)\,. \tag{1.21}$$

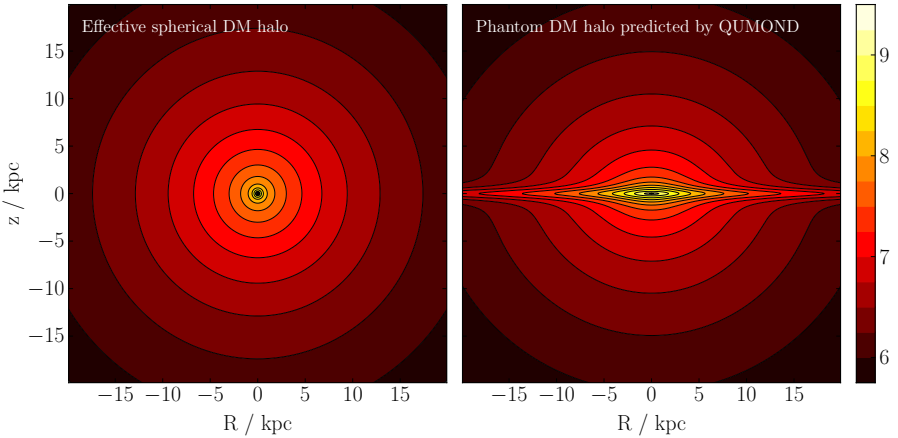

Figure 1.6: Contour plot of the effective (phantom) DM halo density, $\log_{10}(\rho_{\rm ph}(R,z)/(\mathrm{M}_\odot\,\mathrm{kpc}^{-3}))$, predicted by two different formulations of Milgromian dynamics, is plotted as a function of the galactic radius, R, and the galactic height, z, for an example disk model (Miyamoto-Nagai disk with a total mass of $6\times10^{10}\,\mathrm{M}_\odot$, length scale of 2.5 kpc, and z-scale of 0.5 kpc; the baryonic disk is seen edge-on in both plots). ***Left panel.*** The effective, spherical DM halo density that would be deduced from the observed rotation curve, $V_{\rm obs}(R)$, in the galactic plane ($z = 0$), if applying Newtonian dynamics (see equation 1.21). In this example, Milgrom's law is applied to determine $V_{\rm obs}(R)$. ***Right panel.*** The actual 3-dimensional phantom DM halo predicted by a "full" modified gravity theory, in this case QUMOND (equation 1.18), for the same disk model. The phantom halo is not spherical, which is expected since the Newtonian potential is aspherical as well. The halo is isothermal and spherical at very large radii, and oblate at intermediate radii. It further features a "phantom disk" that is aligned with its baryonic counterpart (the exact shapes are however different). In this example, both effective halos yield the identical rotation curve, $V_{\rm obs}(R)$, in the plane of the galactic disk.

While the Newtonian observer would assume the particle DM halo to have a certain shape (e.g. spherical symmetry, or triaxiality), Milgrom's law is restricted to the prediction of the effective acceleration in the galactic plane, where the rotation curve, $V_{\rm obs}(R)$, is measured. To draw a conclusion on the 3-dimensional shape of the effective phantom halo, a full Milgromian theory has to be considered. In the right hand side plot of Figure 1.6, the according PDM halo density predicted by QUMOND (equation 1.18) is plotted. The PDM halo is generally not spherically symmetric (in this particular case, it is axisymmetric). This is not surprising, since the Newtonian potential, $\phi_{\rm N}$, is not spherical either. The PDM halo is isothermal ($\rho_{\rm ph}(\boldsymbol{x}) \propto |\boldsymbol{x}|^{-2}$) and spherical at very large galactic radii, and oblate at intermediate radii. In addition, it features a "phantom disk" that is aligned with its baryonic counterpart (the exact shapes are however different), and which is one of the major differences to the standard picture of particle DM halos. In the axisymmetric example model presented in the figure, both effective halos yield the identical rotation curve $V_{\rm obs}(R)$. The PDM densities of other example models are shown in Figure 2.4 on p. 29 (a polar ring galaxy model), and in Figure 4.5 on p. 69 (an exponential disk model).

1.4 Dynamical models of galaxies in Milgromian dynamics

Prior research on Milgromian dynamics focussed on static problems, i.e. on computing the static gravitational potentials of galaxies, which can be computed from the distribution of baryonic matter, and which are documented by the velocity dispersions and rotation curves of stars and gas. Only a hand full of N-body codes are available to date that allow investigating the consequences of Milgromian gravity on the formation and dynamical evolution of DM-free galaxies. Most simulation codes (see below) focus on cosmological structure formation, and only three are designed for simulating the dynamics of particles on galactic scales. Only one of those codes is publicly available to date, and limited to close-to-spherical systems. None of the galactic codes allows studying galaxies in as much detail as it is possible with the available, very advanced classical Newtonian codes. As a consequence, only little is known about the dynamics, the formation, and the evolution of galaxies in the Milgromian framework. Although the Milgromian dynamics phenomenology has been impressively successful in the recent 30 years, generic and fully dynamical tests using N-body codes with live particles and a full treatment of hydrodynamics are still missing (see also Chapter 4).

Given the broad success of Milgrom's effective law in galaxies, it is now mandatory to make the step from investigating static problems to developing a fundamental understanding of the dynamical consequences of this framework. While it may be possible to explain the static galactic potentials in both, the standard DM framework and the DM-free Milgromian framework, the *dynamical* properties of galaxies are obviously very different in these frameworks. The following differences to the standard DM model are possibly the most salient ones:

(i) In the standard DM picture of galaxies, the pressure-supported DM halo stabilizes the disk and alleviates disk-instabilities, and accordingly the formation of substructure in that disk. If no pressure-supported DM halo exists, and the galactic potential is defined by the baryons alone, **self-gravity** of baryonic matter becomes more important. This strongly affects the disk stability and the formation of smaller substructures (e.g. Brada and Milgrom, 1999; Tiret and Combes, 2007).

(ii) The absence of a particle DM halo means that **dynamical friction** inside and between galaxies plays a much smaller role. Although dynamical friction between the stars is generally stronger in the DM-free framework (Nipoti et al., 2008), there is no additional dynamical friction between baryons and DM particles. As a consequence, the cross-section of galaxy encounters that lead to the merging of the galaxies is much smaller due to the missing DM halos, implying that the differences concerning dynamical friction affect not only the internal evolution of isolated objects, but also the picture of hierarchical structure formation in the Universe (Nusser, 2002),[12] which is a prediction by the standard model of cosmology, and which is strongly controlled by the dynamical friction of the DM halos (Lacey and Cole, 1993).

(iii) Another difference concerns the non-linearity of Milgromian dynamics, which breaks the strong equivalence principle, and leads to new phenomena such as the external field effect (EFE, for details see Chapter 3, and in particular Section 3.2.2). For example, the EFE affects the effective binding energy of satellite galaxies in the external field of their host galaxies (see e.g. Chapter 3), and the internal dynamics of galaxies in the external field of the galaxy clusters they may reside in.

In the following, difficulties in the development of Milgromian dynamics N-body codes are outlined and discussed, and an overview of existing codes is provided.

[12] Note that the cosmological N-body simulations of Nusser (2002) implement the pristine formulation of Milgromian dynamics, and not a full modified gravity theory as described in Section 1.3. For that reason, the related code is not listed in Section 1.4.

N-body codes

The key of any N-body code is the computation of the accelerations, $\boldsymbol{g}_i$, acting on the individual bodies or particles, m_i, in order to integrate the equations of motion for every particle:

$$\boldsymbol{v}_i(t) = \int_{t_0}^{t} \boldsymbol{g}_i(\tau)\,\mathrm{d}\tau\,, \quad \boldsymbol{x}_i(t) = \int_{t_0}^{t} \boldsymbol{v}_i(\tau)\,\mathrm{d}\tau\,. \tag{1.22}$$

This common procedure requires the field equations to be time-independent, which is the case for classical, Newtonian dynamics, and generally for the non-relativistic modified gravity theories described above.

A large number of methods exist for computing the accelerations, but not every method is ideally suited for any problem. The main criteria are the symmetry of the system (if existing), and its relaxation time scale. If the system's average two-body relaxation time is small (i.e. much smaller than one Hubble time), direct N-body forces are important and have to be taken into account. In the simplest way, the direct *Newtonian* forces are computed by summation of the forces due to individual particles,

$$m_i\,\boldsymbol{g}_i = -G \sum_{\substack{j=1 \\ j\neq i}}^{N} \frac{m_i m_j}{|\boldsymbol{x}_j - \boldsymbol{x}_i|^3}\,(\boldsymbol{x}_j - \boldsymbol{x}_i)\,. \tag{1.23}$$

In that case, $N(N-1) \approx N^2$ forces have to be evaluated at every time step. To reduce the computational expense, neighborhood schemes are used, which compute the direct forces between only the nearest particles and approximate the potential of the other particles by their center of mass systems, in order to still provide a sufficient accuracy and, at the same time, to allow for two-body relaxation effects. The most prominent of these schemes is the tree-code technique by Barnes and Hut (1986). If, on the other hand, the two-body relaxation time is longer than one Hubble time, the system is effectively collisionless and obeys the collisionless Boltzmann equation. In that case, the gravitational potential, $\Phi(\boldsymbol{x})$, is commonly computed from the matter density distribution, $\rho(\boldsymbol{x}) = \sum_i \delta(\boldsymbol{x}_i - \boldsymbol{x}) m_i$, by solving the Poisson equation, which is $\nabla^2\Phi(\boldsymbol{x}) = 4\pi G\rho(\boldsymbol{x})$ in Newtonian dynamics. The resulting acceleration is $\boldsymbol{a}_i = -\nabla\Phi(\boldsymbol{x}_i)$. Such solvers rely on grid techniques, where the matter density distribution, ρ, is discretized with the help of spatial grids. This ansatz allows computing the accelerations of a large number of particles, which is necessary for simulations of large systems, such as galaxies. The number of particles thereby defines the maximum spatial resolution that can be achieved. The most common method solves the Poisson equation in Fourier space using Green's functions (GFs). This procedure is generally very fast, but requires for every grid geometry another GF, and is therefore not suited for arbitrary grids geometries. An alternative method uses a relaxation scheme to find $\phi(\mathbf{x})$. Starting from an initial guess, the iterative relaxation solver corrects the values of the potential until a convergence criterium is fulfilled. The second method is generally computationally more time-consuming compared to the first method (if one neglects the generation of the GFs), but requires less amount of memory and is ideally suited for grids with arbitrarily shaped boundaries.

Most of these techniques are however based on the superposition of gravitational potentials and the according force fields, i.e. the strong equivalence principle, and thus hinge on the linearity of Newtonian dynamics. The non-linear Milgromian dynamics theories pose complications in that respect, and it becomes necessary to solve the Poisson equation for all particles simultaneously.

The following Milgromian dynamics N-body codes have been developed so far, the stars mark codes that are publicly available. **(A)** The single-grid code by Tiret and Combes (2007) implements the AQUAL formulation of Milgromian dynamics. The code has rudimentary treatment of gas dynam-

ics, but has never been made publicly available, and its development has been discontinued. **(B*)** The cosmological N-body code by Llinares et al. (2008), which is based on the Amiga code, is designed specifically for cosmological pure-N-body simulations. It does not take into account magnetohydrodynamics (MHD) or baryonic sub-grid physics (star formation, stellar feedback etc.), contrary to its predecessor, the classical Amiga code, which uses N-body techniques for DM particles and MHD to treat baryonic matter. **(C*)** The Nmody code by Londrillo and Nipoti (2009) uses multipole-expansions to fit the gravitational potential defined by the AQUAL Poisson equation (1.15) in a spherical coordinate system. Through the specific choice of the coordinate system, it is ideally suited for spherical or close-to-spherical problems, but less useful for generic simulations (of e.g. galaxy-galaxy encounters). **(D)** The cosmological N-body code by Angus and Diaferio (2011) is the first code that makes use of the QUMOND formulation, using a single, coarse grid with periodic boundary conditions. **(E)** The galactic N-body code by Angus et al. (2012) uses centered multi-grids to allow a sufficient resolution at the galactic center, and, at same time, a simulation box that is large enough (2^{10} times the size of the innermost grid) to apply the Dirichlet boundary conditions $\partial\Phi = 0$.

In the course of this thesis, I implemented the described QUMOND formulation in the already existing hydrodynamics and N-body code Ramses (Teyssier, 2002). The customized code is referred to as the Phantom of Ramses (POR), and inherits all the already well-established and advanced features that the state-of-the-art parent code Ramses offers. Contrary to earlier Milgromian dynamics codes, POR features a fully adaptive mesh-refinement (AMR, Kravtsov et al., 1997) strategy: starting from a large coarse grid that satisfies the Dirichlet boundary conditions $\partial\phi_\mathrm{N} = GM_\mathrm{b}/r^2_\mathrm{M_b}$ and $\partial|\nabla\phi_\mathrm{N}| \ll a_0$ (see Section 3.3.1), the grid is recursively refined based on the spatial matter density. This mesh refinement is illustrated in Figure 1.7. It allows large simulation boxes (which is important for simulations of e.g. galaxy-galaxy interactions) while achieving a high spatial and temporal resolution in the regions of interest, independent of the simulation box dimensions, and only depending on the particle number density. Moreover, the code includes the common and already established physical sub-grid processes, like gas cooling processes, formation of stellar populations from that gas, stellar feedback, etc. The POR code is very versatile, and is suited for various different contexts. It is capable of handling isolated and interacting systems, and also of investigating the formation of structures in a cosmological context. The code is presented in detail in Lüghausen et al. (2014a) (that is Chapter 4 here), and it will be made publicly available within the standard Ramses package to facilitate the research on this topic.

1.5 Overview of this PhD thesis

In the course of this PhD thesis, I developed a Milgromian dynamics N-body code on the basis of the existing N-body and hydrodynamics code Ramses, and the modified gravity theory QUMOND developed by Milgrom (2010). The code is presented in Chapter 4. The publications that constitute the chapters 2–4 are the scientific outcome that emerged during the different stages of the code development.[13]

In Chapter 2, *Polar ring galaxies as tests of gravity*, a single Cartesian grid is used to compute the static Milgromian acceleration field of polar ring galaxy (PRG) models, and the according rotation curves. Polar ring galaxies are predestinated for testing theories of gravity, because they exhibit two distinct rotation curves, one in the plane of the host galaxy, and a second one in the rotating polar structure, which is oriented perpendicularly to the host, and which is typically dominated by gas. Both rotation curves must be explained by a single gravitational potential. Based on baryonic models that are typical for those objects, the 3-dim. Milgromian potential is computed, and the non-circular rotation

[13] The single, refereed publications are included into this cumulative dissertation without changes. Only the layouts have been adapted.

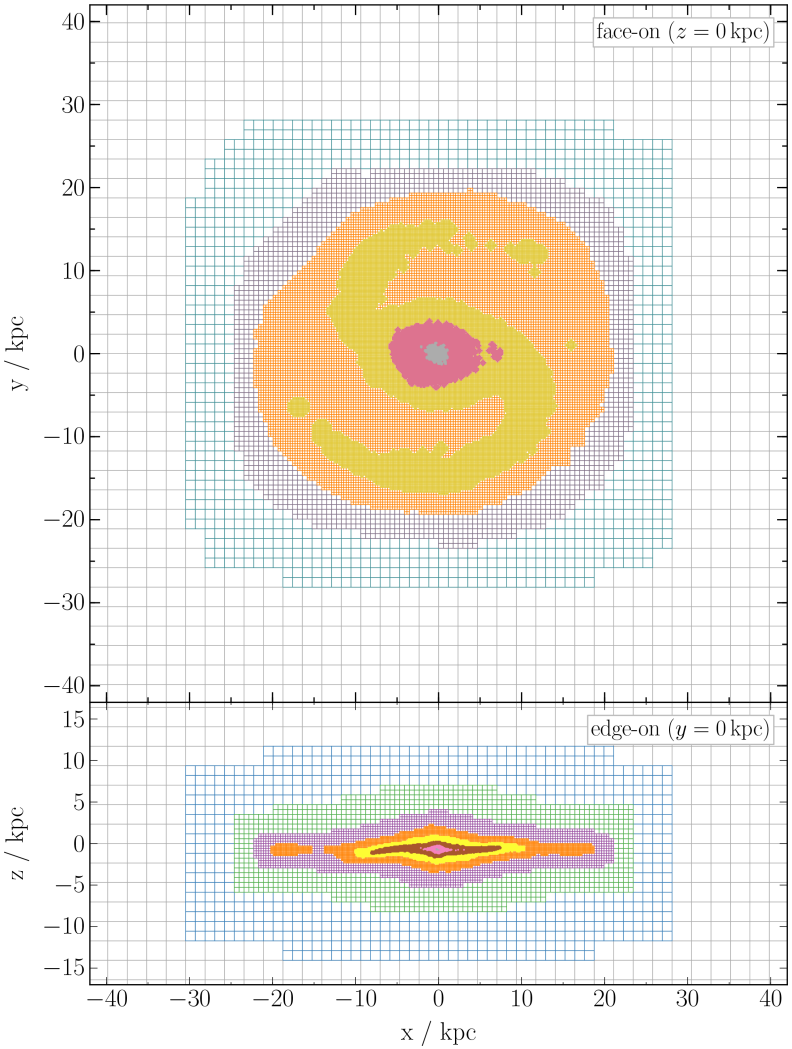

Figure 1.7: The Phantom of Ramses (POR) code makes use of the adaptive mesh refinement (AMR) technique to achive high spatial resolution. On a cell-by-cell and level-by-level basis, coarse cells are recursively refined (i.e. split into 2^{dim} sub-cells) if they exceed a given particle number or mass threshold. This example (cf. p. 73, Figure 4.8, $t = 1200$ Myr) has a box size of $(300\,\mathrm{kpc})^3$, a minimum resolution (outermost, gray cells) of $300\,\mathrm{kpc}/2^7 = 2.34\,\mathrm{kpc}$, and features a rotating disk galaxy that has been evolved in the POR code for 1.2 Gyr. The figure shows the grid structure in the cross sections through the x-y plane ("face-on", $z = 0$) and through the x-z plane ($y = 0$, "edge-on"), and illustrates how the AMR algorithm resolves and adapts to the galactic substructure.

curves therein. In a qualitative analysis, it is shown that Milgromian dynamics generally accounts well for the rotation curves of these objects, which are difficult to reconcile with Newtonian dynamics if the galaxies are embedded in a DM halo, even if the halo is allowed to be non-spherical, because the required distribution of the DM particles leads to unlikely galaxy formation scenarios.[14]

In Chapter 3, *A census of the expected properties of classical Milky Way dwarfs in Milgromian dynamics*, static models of the five most luminous dwarf spheroidal satellite galaxies (dSphs) of the Milky Way are analyzed. Those dSphs are of special interest, because their high velocity dispersion cannot be understood in the standard DM-framework: neither as tidal dwarf galaxies (TDGs), because TDGs cannot contain as much DM, nor as primordial dwarf galaxies (PDGs), because PDGs should be distributed (nearly) isotropically around the DM halo of their hosting galaxy, which is apparently not the case in the Local Group. In the work presented in this chapter, the final QUMOND Poisson solver implemented in the POR code is used. The Milgromian potential of a large computational box, which hosts a realistic model of the Milky Way (MW) and the satellite galaxies at the same time, is evaluated with the help of the adaptive mesh refinement (AMR) technique. This procedure allows the self-consistent modeling of the external field effect (EFE) caused by the potential of the MW model. The EFE has a particular influence on the shape of the effective gravitational potentials of each of the individual satellite galaxies, and therewith adds new interesting aspects to the cusp/core debate of the putative DM halos, and of the effective PDM halos in the case of Milgromian dynamics. It is shown that the inner shape of the (phantom) DM halos predicted by Milgrom's framework is in very good agreement with observations. General predictions of the effective dynamical mass of these objects are made and compared to the literature. While the results for the most luminous satellites, Fornax and Sculptor, agree well with available velocity dispersion data, the estimated dynamical mass-to-light ratios for Sextans, Carina, and Draco are low compared to usually quoted observational estimates, as has already been pointed out in previous work. The possible consequences are discussed.

In Chapter 4, *Phantom of RAMSES (POR): A new Milgromian dynamics N-body code*, the final N-body code is presented, together with tests and sample applications, which are simulations of exponential disk galaxies, with and without initial elliptical bulges. The functionality of the code is proven, and I demonstrate that I have already developed the software tools necessary to set up the basic dynamical models for further, more sophisticated models for use in Milgromian dynamics simulations. While evolving a N-body system is one technical challenge, generating its initial conditions is another. While such tools are publicly available for Newtonian systems, this has not yet been the case for the Milgromian framework. The developed tools allow to generate initial conditions for equilibrium models of (i) isolated, spherically symmetric, pressure-supported objects (e.g., collisionless globular clusters, dwarf galaxies, elliptical galaxies, etc.); (ii) rotating exponential disk galaxies; and (iii) rotating exponential disk galaxies with flattened initial bulge. The disk setup procedures are capable of taking into account additional arbitrary potentials, e.g. for a gaseous disk. These developments constitute the fundament of future work with the code.

[14] See also the conference proceeding, *Polar Ring Galaxies Favor Milgromian Dynamics over Standard Dark-Matter-Based Models* (Lüghausen et al., 2014b).

CHAPTER 2

Polar ring galaxies as tests of gravity

Published in
MNRAS, Volume 432, Issue 4, p. 2846–2853
July 2013

DOI: 10.1093/mnras/stt639

F. Lüghausen, B. Famaey, P. Kroupa, G. Angus, F. Combes, G. Gentile, O. Tiret, and H. Zhao

Abstract

Polar ring galaxies are ideal objects with which to study the three-dimensional shapes of galactic gravitational potentials since two rotation curves can be measured in two perpendicular planes. Observational studies have uncovered systematically larger rotation velocities in the extended polar rings than in the associated host galaxies. In the dark matter context, this can only be explained through dark halos that are systematically flattened along the polar rings. Here, we point out that these objects can also be used as very effective tests of gravity theories, such as those based on Milgromian dynamics (MOND). We run a set of polar ring models using both Milgromian and Newtonian dynamics to predict the expected shapes of the rotation curves in both planes, varying the total mass of the system, the mass of the ring with respect to the host, as well as the size of the hole at the center of the ring. We find that Milgromian dynamics not only naturally leads to rotation velocities being typically higher in the extended polar rings than in the hosts, as would be the case in Newtonian dynamics without dark matter, but that it also gets the shape and amplitude of velocities correct. Milgromian dynamics thus adequately explains this particular property of polar ring galaxies.

2.1 Introduction

Assuming General Relativity to be the correct description of gravity at all scales, data ranging from the largest scales (e.g., the Cosmic Microwave Background) to galactic scales can be interpreted as a Universe dominated by dark energy and dark matter. The nature of these is among the most challenging problems of modern physics. While dark energy is generally assumed to be a non-vanishing vacuum energy represented by a cosmological constant Λ in Einstein's equations, the currently most favored dark matter candidates are neutral fermionic particles, which condensed from the thermal bath of the early Universe (Bertone et al., 2005; Strigari, 2012), known as "cold dark matter" (CDM) particles.

On galaxy scales, predictions of this concordance cosmological model (ΛCDM) are difficult to reconcile with observations (Disney et al., 2008; Peebles and Nusser, 2010; Kroupa et al., 2010; Kroupa, 2012; Kroupa et al., 2012). For instance, many observed scaling relations (see Famaey and McGaugh, 2012, for a review) involve the universal appearance of an acceleration constant $a_0 \approx \Lambda^{1/2} \approx 10^{-10}\mathrm{m\,s^{-2}} \approx 3.6\,\mathrm{pc\,Myr^{-2}}$, whose origin is unknown in the standard context. For instance, this constant defines the zero-point of the Tully-Fisher relation, the transition of the acceleration at which the mass discrepancy between baryonic and dynamical mass appears in the standard picture, the transition central acceleration between dark-matter dominated and baryons-dominated galaxies (within Newtonian gravity), and it defines a critical mean surface density for disk stability (Famaey and McGaugh, 2012). These independent occurences of a_0 are not at all understood in the standard context, whereas, surprisingly, all these relations can be summarized by the empirical formula of Milgrom (1983). For this formula to fit galaxy rotation curves, the above quoted value of a_0 can vary only between 0.9 and $1.5 \times 10^{-10}\mathrm{m\,s^{-2}}$, but once a value is chosen, all galaxy rotation curves must be fitted with a single value (Gentile et al., 2011). We choose here the median value $a_0 = 1.2 \times 10^{-10}\mathrm{m\,s^{-2}}$, as per Gentile et al. (2011).

The success of Milgrom's empirical formula lends weight to the idea that the gravitational field in galaxies can be described by Milgromian Dynamics (also known as Modified Newtonian Dynamics or MOND). Milgromian dynamics naturally explains the intimate relation between the distribution of baryons and the gravitational field in galaxies, and explains all the aforementioned occurrences of a_0 in galactic dynamics without any fine-tuning. Given the predictive nature of Milgromian dynamics on galaxy scales, it is of great interest to test whether the formula can explain all probes of galactic gravitational potentials, beyond spherical and axisymmetric systems where it has mostly been tested up to now.

Polar ring galaxies (PRGs) are non-axisymmetric systems featuring an outer ring of stars and gas rotating over the poles. The host galaxy is usually characterized by a compact bulge and a small bright gas-poor disk, while the gas-rich polar structure has photometric properties roughly similar to those of gas-rich spirals (e.g., Whitmore et al., 1990). The observer can typically measure two perpendicular rotation curves (Schweizer et al., 1983; Sackett and Sparke, 1990; Sackett et al., 1994; Reshetnikov and Combes, 1994; Combes and Arnaboldi, 1996; Iodice et al., 2003, 2006; Iodice, 2010), one in the host, often by deriving an asymmetric-drift corrected rotation curve from the observed stellar kinematics (see, e.g., Combes and Arnaboldi, 1996), and one in the polar ring, by directly measuring the velocity of the HI gas. This makes PRGs ideal test objects for gravity theories, because any given theory of gravity then has to explain two rotation curves in two perpendicular planes, both derived from the same baryonic mass density distribution. Interestingly, observational studies (Iodice et al., 2003; Moiseev et al., 2011) consistently show rotational velocities in the polar rings to be systematically larger than in the hosts. These observations may only be explained in the standard context by dark halos systematically flattened along the polar rings (see Iodice et al., 2003). In any case, given these specific observational properties of PRGs, it is of great interest to investigate whether the general predictions of Milgromian dynamics for such objects would conform with these observational properties, namely whether larger velocities in

the extended polar rings than in the hosts are a generic prediction of Milgromian dynamics, by exploring a wide range of baryonic mass distributions.

In Sect. 3.2, we recall the basics of Milgromian dynamics and the specific quasi-linear formulation we are dealing with. We then present a grid-based prescription to solve the modified Poisson equation (Sect. 2.3) and an iterative method to find rotation curves of non-circular orbits (Sect. 2.4), and apply it to a set of models in Sect. 2.5. Results are presented and discussed in Sect. 2.6 and we conclude in Sect. 2.7.

2.2 Milgromian dynamics

In recent years, a plethora of generally covariant modified gravity theories have been developed, yielding a Milgromian behavior in the weak-field limit (Famaey and McGaugh, 2012). One such recent formulation (Milgrom, 2009a) has a non-relativistic quasi-static weak field limit, for a specific given set of parameters, yielding the following Poisson equation:

$$\nabla^2\Phi = 4\pi G\rho_\mathrm{b} + \nabla\cdot\left[\nu\left(|\nabla\phi|/a_0\right)\nabla\phi\right], \tag{2.1}$$

where Φ is the total (Milgromian) potential, ρ_b is the baryonic density, ϕ the Newtonian potential such that $\nabla^2\phi = 4\pi G\rho_\mathrm{b}$, and where $\nu(x) \to 0$ for $x \gg 1$ and $\nu(x) \to x^{-1/2}$ for $x \ll 1$. One family of functions that fulfills the definition of $\nu(x)$ (see, e.g. Famaey and McGaugh, 2012) is

$$\nu(x) = \left[1 + (1 + 4x^{-n})^{1/2}/2\right]^{1/n} - 1. \tag{2.2}$$

Hereafter, when not stated otherwise, we use $n = 1$, a function which is known to reproduce well the rotation curves of most spiral galaxies[1] (Gentile et al., 2011).

This means that the total gravitational potential $\Phi = \phi + \Phi_\mathrm{ph}$ can be divided into a classical (Newtonian) part, ϕ, and a Milgromian part, Φ_ph. The matter density distribution ρ_ph that would, in Newtonian gravity, yield the additional potential Φ_ph, and therefore obeys $\nabla^2\Phi_\mathrm{ph} = 4\pi G\rho_\mathrm{ph}$, is known in the Milgromian context as the "phantom dark matter" (PDM)[2] density,

$$\rho_\mathrm{ph} = \frac{\nabla\cdot\left[\nu\left(|\nabla\phi|/a_0\right)\nabla\phi\right]}{4\pi G}. \tag{2.3}$$

This is the density of dark matter that would boost the Newtonian gravitational field to give precisely the same effect as the boost of gravity predicted by Milgromian dynamics. For a disk galaxy, it will typically resemble a round isothermal halo at large radii, but exhibits an additional disk of phantom dark matter aligned with the baryonic disk (but with a different scale length and height) most prominent at smaller radii (Milgrom, 2001). At each spatial point, ρ_ph is a non-linear function of the Newtonian potential. As the non-linearity of Eq. 2.1 is only present on the right-hand side of the equation, it is called the quasi-linear version of Modified Newtonian dynamics (Milgrom, 2010) whereas in older versions of Milgromian dynamics theories the Laplacian operator on the left-hand side was replaced by a non-linear one (Bekenstein and Milgrom, 1984). In the next section, we present a grid-based prescription to

[1] Nowadays, galaxy data still allow some, but not much, wiggle room on choosing the interpolating function $\nu(x)$ (Eq. 3.3): they tend to favor the $n = 1$ function from the family used here; some interpolation between $n = 1$ and $n = 2$; or functions from other families which actually reduce, for accelerations typical of galaxies, to the $n = 1$ case used here. See, e.g., Sect. 6.2. of Famaey and McGaugh (2012) for a review.

[2] In the Milgromian context, PDM is not real matter but a numerical ansatz which helps to compute the additional gravity predicted by Milgromian dynamics and gives it an analog in Newtonian dynamics.

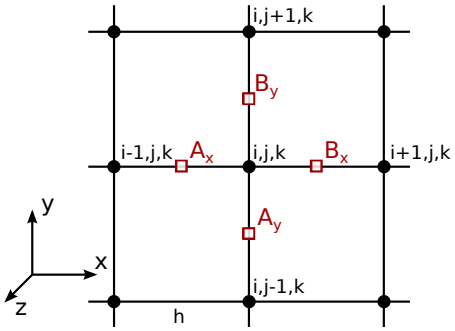

Figure 2.1: Illustration of the discretisation scheme in the x-y plane, referring to Eq. 2.4. The grid has N^3 nodes (i, j, k) with i, j, k $\in \{1 \dots N\}$ that are separated by a constant grid step size h. The values of $\nu(x)$ are evaluated at the points A_k and B_k in k-direction using Eq. 2.5.

calculate the PDM density. We will then be able to compute the rotation curves from the velocity of the closed orbits crossing the planes of symmetry of the non-axisymmetric system (i.e. the plane of the host galaxy and of the polar ring).

2.3 Grid-based calculation of the phantom dark matter density

The PDM density that would source the Milgromian force field in Newtonian gravity is defined by Eq. 2.3 and can be calculated from the known classical (Newtonian) potential ϕ. To evaluate this term, we devise a numerical, grid-based scheme that calculates $\rho_{\rm ph}$ from any (discrete) Newtonian potential $\phi^{\rm i,j,k}$ (see Famaey and McGaugh, 2012, Eq. 35; Angus and Diaferio, 2011; Angus et al., 2012).

The discrete form of Eq. 2.3 then reads

$$\rho_{\rm ph}^{\rm i,j,k} = \frac{1}{4\pi G}\frac{1}{h^2}\Big[\left(\phi^{\rm i+1,j,k}-\phi^{\rm i,j,k}\right)\nu_{\rm Bx} - \left(\phi^{\rm i,j,k}-\phi^{\rm i\text{-}1,j,k}\right)\nu_{\rm Ax} + \left(\phi^{\rm i,j+1,k}-\phi^{\rm i,j,k}\right)\nu_{\rm By} - \left(\phi^{\rm i,j,k}-\phi^{\rm i,j\text{-}1,k}\right)\nu_{\rm Ay} + \left(\phi^{\rm i,j,k+1}-\phi^{\rm i,j,k}\right)\nu_{\rm Bz} - \left(\phi^{\rm i,j,k}-\phi^{\rm i,j,k\text{-}1}\right)\nu_{\rm Az}\Big], \tag{2.4}$$

with h being the constant one-dimensional grid step size. The whole discretization scheme is illustrated in Fig. 4.1. Note that this equation was first derived for older versions of Milgromian dynamics by Brada and Milgrom (1999) and Tiret and Combes (2007) and we derive it for the quasi-linear formulation here (see also Angus and Diaferio, 2011; Angus et al., 2012). The function $\nu(x)$ is evaluated at the points marked by squares in Fig. 4.1. The gradient of ϕ in $\nu\left(|\nabla\phi|/a_0\right)$ at the point B_x has been approximated by

$$\nabla\phi = \frac{1}{4h}\begin{pmatrix} 4\left(\phi^{\rm i+1,j,k}-\phi^{\rm i,j,k}\right) \\ \phi^{\rm i+1,j+1,k} - \phi^{\rm i+1,j\text{-}1,k} + \phi^{\rm i,j+1,k} - \phi^{\rm i,j\text{-}1,k} \\ \phi^{\rm i,j,k+1} - \phi^{\rm i,j,k\text{-}1} + \phi^{\rm i+1,j,k+1} - \phi^{\rm i+1,j,k\text{-}1} \end{pmatrix}. \tag{2.5}$$

Having evaluated this field, the Newtonian Poisson equation, $\nabla^2\Phi = 4\pi G\left(\rho_{\rm b}+\rho_{\rm ph}\right)$, can be solved to find the effective Milgromian force field. This can be done using the same grid. In the present paper,

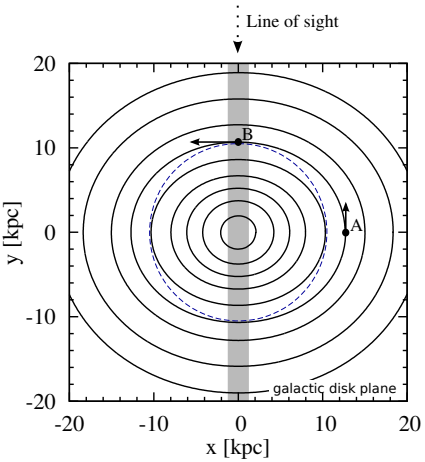

Figure 2.2: Closed orbits (black, solid lines) within the potential of the benchmark model (Seq. 1, $M_{\rm PR} = 1.45\,M_{\rm disk}$) in the plane of the host galaxy. The polar ring, which is located in the y-z plane, is illustrated by the thick, grey line. The blue, dashed line is a circle which, by comparison, demonstrates the non-circularity of the closed-loop orbits. The major axis of the eccentric orbits points in the x-direction, because the test particles orbiting in the galactic disk (x-y) plane "fall" through the polar ring (y-z) plane, i.e. they feel a stronger acceleration in x than in y direction. However, to fulfill closed orbits, the oscillation period in both directions must be the same, which means that the oscillation amplitude in the x direction must be larger (major axis) than that in the y direction (minor axis). The rotation velocity thus is minimal at point A (along the line of sight) and maximal at point B.

grids with a resolution of $h = 0.23$ kpc are used to calculate the rotation curves (see next section) from 2 to 16 kpc, and grids with $h = 0.47$ kpc for radii larger than 16 kpc. The resolution was chosen such that it is sufficiently fine that the form of the rotation curves does not change if the resolution is further increased.

2.4 Calculation of rotation curves

From a given Milgromian potential Φ (see next section for detailed description of PRG models), rotation curves (or rather, their non-circular equivalent in non-axisymmetric configurations) can be calculated. In an axisymmetric potential, the circular rotation velocity $v(r)$, which results in closed orbits with radius r, readily follows as $v(r) = \sqrt{-r\,\mathrm{d}\Phi/dr}$ in the plane of the galactic disk. This equation however loses validity in a non-axisymmetric potential like the one of a PRG, because the closed orbits are generally not circular. The existence of two massive systems in perpendicular orientations means that circular orbits do not exist in either system, neither the equatorial nor the polar one: in each plane, the potential well corresponding to the other perpendicular system produces the equivalent of a (non-rotating) bar along the line of nodes. In that case, it becomes necessary to obtain the velocities in the disk and polar ring in a more general way. In the present work, an iterative method is applied: test stars are shot through the galactic potential, which is computed numerically from analytical density distributions following the prescription in Sect. 2.3. The initial velocity (perpendicular to the radius) of these test

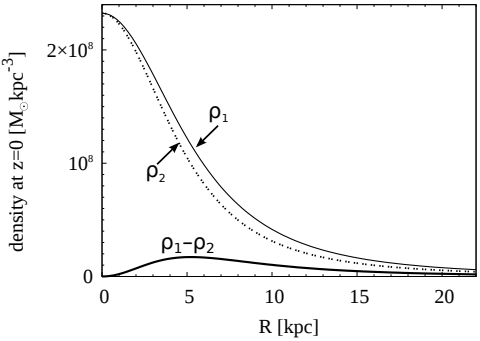

Figure 2.3: The polar ring density profile is made from the difference of two Miyamoto-Nagai density profiles (ρ_1 and ρ_2). Its density is zero at the centre. This example is a demonstration of a ring with a total mass $M = 9.5 \times 10^9\,\mathrm{M}_\odot$, a scale height $h_z = 0.3\,\mathrm{kpc}$ and scale radii $h_{r_1} = 6.8\,\mathrm{kpc}$ and $h_{r_2} = 5.95\,\mathrm{kpc}$

particles is adjusted until a closed orbit is found. The orbit is integrated using the simple leapfrog integration scheme. Typical closed orbits in a PRG potential are shown in Fig. 2.2 (detailed description of the model in the next section).

2.5 Models

In order to explore the consequences of Milgromian dynamics for the rotation curves in polar rings, we start from a benchmark model adopted from Combes and Arnaboldi (1996), which represents a prototypical example of polar ring galaxy (NGC 4650A). From this model, we will construct a Milgromian potential in which the orbits of test particles will be computed. The host galaxy is made of a small Plummer bulge (Plummer, 1911) weighing $M_\mathrm{b} = 0.2 \times 10^9\,\mathrm{M}_\odot$, with a Plummer radius $r_\mathrm{p} = 0.17\,\mathrm{kpc}$,

$$\rho_\mathrm{b}(r) = \left(\frac{3M_\mathrm{b}}{4\pi r_\mathrm{p}^3}\right)\left(1+\left(\frac{r}{r_\mathrm{p}}\right)^2\right)^{-5/2}, \tag{2.6}$$

and of a Miyamoto-Nagai disk (Miyamoto and Nagai, 1975) with disk mass $M_d = 11 \times 10^9\,\mathrm{M}_\odot$, scale-length $h_r = 0.748\,\mathrm{kpc}$ and scale-height $h_z = 0.3\,\mathrm{kpc}$,

$$\rho_\mathrm{d}(R,z) = \left(\frac{{h_z}^2 M_\mathrm{d}}{4\pi}\right) \times \frac{h_\mathrm{r}R^2 + (h_\mathrm{r} + 3\sqrt{z^2+{h_z}^2})\left(h_\mathrm{r} + \sqrt{z^2+{h_z}^2}\right)^2}{\left[h_\mathrm{r}^2 + \left(h_\mathrm{r} + \sqrt{z^2+{h_z}^2}\right)^2\right]^{5/2}\left(z^2+{h_z}^2\right)^{3/2}}. \tag{2.7}$$

To this parent galaxy a polar ring of stars and another one of gas is added[3]. Each ring is built by the difference of two Miyamoto-Nagai density distributions of scale height $h_z = 0.3\,\mathrm{kpc}$, and with scale radii h_{r_1} and h_{r_2} (see Fig. 2.3 for an illustration, where one sees that the baryonic density is precisely

[3] We do not consider the possibility of two gaseous disks to avoid orbits crossing, unless there is a very small gas disk and a much larger gaseous polar ring which never intersect. In our models, we make no distinction between gas and stars in the host disk.

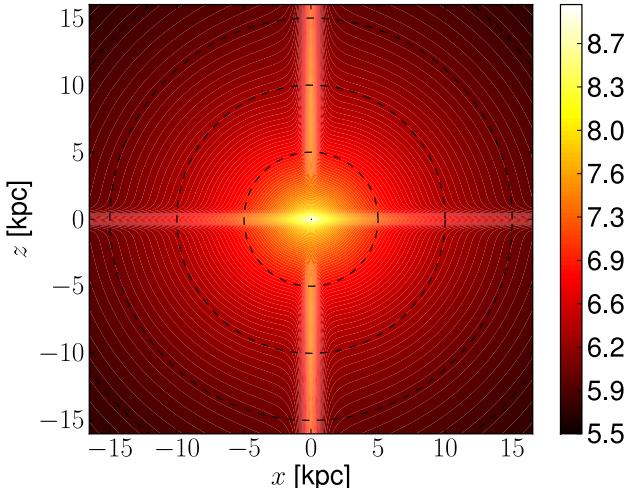

Figure 2.4: The figure shows contours of the mass density of the phantom dark matter of the benchmark model seen edge-on (x-z plane, $y = 0$). The colour bar shows the logarithm of the PDM density in $M_\odot\,kpc^{-3}$. In addition to the oblate phantom dark matter (PDM) halo, the horizontal overdensity shows clearly the PDM in the host disk and the vertical over density shows the PDM in the polar ring. The dashed circles are to demonstrate that the phantom halo is nearly spherical and slightly oblate.

zero at the center and positive elsewhere). The masses of these two disks are chosen such that their difference equals the total mass of the ring and that the central mass density of the ring is zero. The stellar ring weighs $9.5 \times 10^9\,M_\odot$, and has $h^{st}_{r_1} = 6.8\,kpc$ and $h^{st}_{r_2} = 5.95\,kpc$, while the gaseous ring weighs $6.4 \times 10^9\,M_\odot$, and has $h^{gas}_{r_1} = 15.3\,kpc$ and $h^{gas}_{r_2} = 3.4\,kpc$. The parameters of these rings are such that the density in the center is zero and positive everywhere else. Note that these parameters are adopted exactly as per Combes and Arnaboldi (1996), but that in reality, some freedom on the mass of the stellar components in both the host and ring of NGC 4650A is possible. As we do not intend here to make a full detailed fit of the rotation curves of NGC 4650A, which will be the topic of a following paper, including other individual polar ring systems observed in HI with the WSRT (Westerbork Synthesis Radio Telescope), we keep the benchmark model as such. From this density of baryonic matter, we compute the corresponding PDM density using Eq. 2.4. The computed distribution of PDM in the plane orthogonal to both the disk and ring is plotted in Fig. 2.4. This figure illustrates that, in addition to the oblate PDM halo (isothermal at large radii), there are also two PDM disks aligned with the baryonic disks of the host and of the polar ring.

To investigate whether the results we obtain (see Sect. 2.6) for this benchmark model are actually a generic prediction of Milgromian dynamics, we will then vary the parameters of this benchmark model in 5 different ways (including changing the ring into a Miyamoto-Nagai disk) computing a total of 45 models spanning a wide range of parameters. All models and their different parameters are summarized in Table 2.1.

- First, the density of the polar rings and accordingly their mass, M_{PR}, relative to the mass of the

Seq.	M_d [$10^9\,\mathrm{M}_\odot$]	$M_\mathrm{PR}/M_\mathrm{d}$	$h_{\mathrm{r}_1}^{\mathrm{gas}}$ [kpc]	$h_{\mathrm{r}_2}^{\mathrm{gas}}$ [kpc]	$h_{\mathrm{r}_1}^{\mathrm{st}}$ [kpc]	$h_{\mathrm{r}_2}^{\mathrm{st}}$ [kpc]
1	11.0	0.1, 0.25, 0.33, 0.5, 0.75, 1, 1.45	6.8	5.95	15.3	3.4
2	33.0	0.1, 0.25, 0.33, 0.5, 0.75, 1, 1.45	6.8	5.95	15.3	3.4
3	11.0	0.1, 0.25, 0.33, 0.5, 0.75, 1, 1.45	0.748	–	0.748	–
4	11.0	1.45	15.3	3.4	15.3	3.4
			7.8	4.95	15.3	3.4
			5.8	4.95	15.3	3.4
			6.8	5.95	15.3	3.4
			6.8	5.95	11.3	7.4
			6.8	5.95	6.8	5.95
			10.8	9.95	10.8	9.95
5	2.8, 3.7, 5.6, 7.5, 8.4, 11.2, 13.0, 14.6, 16.4, 18.4, 20.7, 23.7, 30.6, 33.6, 36.8, 41.3	1.45	6.8	5.95	15.3	3.4

Table 2.1: Model parameters. In the presented models of PRGs, each ring is built by the difference of two Miyamoto-Nagai disks (see the text for more details), whose radial parameters are h_{r_1} and h_{r_2}. Model 7 of Seq. 1 and Model 4 of Seq. 4 equal the benchmark model. The models of Seq. 3 do not feature a polar ring but a polar disk of stars and gas with radial parameters $h_{\mathrm{r}_1}^{\mathrm{gas/st}}$. Seq. 6 is not included in this table, it corresponds to the benchmark model with 4 different ν-functions.

host galaxy is varied. The resulting models are collected into two sequences: Sequence 1 and Sequence 2. Starting from $M_\mathrm{PR} = 0$, the ring mass is increased to $M_\mathrm{PR} = (0.1, 0.25, 0.33, 0.5, 0.75, 1$ and 1.45 M_disk. Sequence 1 has a constant disk mass of $M_\mathrm{disk} = 11 \times 10^9\,\mathrm{M}_\odot$, Sequence 2 has $M_\mathrm{disk} = 33 \times 10^9\,\mathrm{M}_\odot$.

- To obtain Sequence 3, Sequence 1 is repeated while replacing the polar ring by a polar disk of mass M_PD. This polar disk is shaped like a Miyamoto-Nagai density distribution with $h_\mathrm{r} = 0.748\,\mathrm{kpc}$ and $h_\mathrm{z} = 0.3\,\mathrm{kpc}$. The polar disk mass, M_PD, is varied analogously to Sequence 1 and 2.
  In this sequence, the model with $M_\mathrm{PD}/M_\mathrm{disk} = 1$ is symmetric, the rotation curves in the galactic plane and in the polar plane are consequently identical.

- To investigate the influence of the polar ring shape, we vary the shape of the ring in Sequence 4. The size parameters of the gaseous ring ($h_{\mathrm{r}_1}^{\mathrm{gas}}$ and $h_{\mathrm{r}_2}^{\mathrm{gas}}$) and of the stellar ring ($h_{\mathrm{r}_1}^{\mathrm{st}}$ and $h_{\mathrm{r}_2}^{\mathrm{st}}$) are summarized in Table 1.

- Models of Sequence 5 have again the same structural parameters as the benchmark model, but their densities are scaled such that their total masses (of the whole system) range from $6.8{\times}10^9\,\mathrm{M}_\odot$ to $10^{11}\,\mathrm{M}_\odot$. The size parameters remain unchanged.

- Sequence 6 is a series of four different Milgromian potentials computed for the benchmark model for $n = 1, 2, 3, 4$ in Eq. 3.3, to check whether the qualitative results are independent of the ν-function.

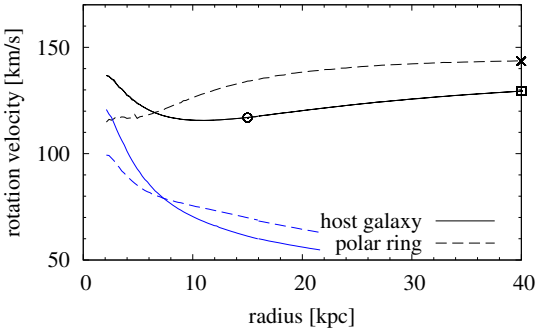

Figure 2.5: Rotation curves of the host galaxy (black, solid line) and polar ring (black, dashed line) for the benchmark model. These rotation curves are derived from the Milgromian potential. For comparison, the blue lower lines show the rotation curves derived from the Newtonian potential of the same model. Observationally, the rotation velocity in the host is generally obtained indirectly from the measured stellar velocity dispersion, which means that the maximum velocity is most likely not measured in the very flat part. To account for this issue, the theoretical rotation velocity from the models are computed at both $r = 40\,\mathrm{kpc}$ and $r = 15\,\mathrm{kpc}$. The circle and cross at these two radii thus mark the rotation velocities that are summarized in Fig. 2.8. In the case where both the host and PR are gas-rich, the PR curve should start where the host curve ends (e.g., at 15 kpc) to avoid collisional orbit crossing.

2.6 Results

The rotation curves of the benchmark model are presented in Fig. 2.5, both in Newtonian without dark matter and Milgromian dynamics. In both cases, the velocity is higher in the ring, but of course, Milgromian dynamics is needed to get the amplitude and shape of the rotation curves right. This is a key result for Milgromian dynamics, since observational studies (Iodice et al., 2003) have measured rotation velocities in extended polar rings being systematically larger than in the host galaxies when both systems are seen roughly edge-on. If this result is generic, it means that this particular property of polar ring galaxies does not exclude Milgromian dynamics. To investigate whether this is indeed a generic prediction of Milgromian dynamics, we vary the parameters of this benchmark model as explained in Sect. 2.5. Altogether, the rotation velocities, corresponding to the line-of-sight velocities that would be measured when observing the PRG edge-on, of 45 models in total are evaluated. The rotation curves of the benchmark model are presented in Fig. 2.5. Fig. 2.6 contains all evaluated rotation curves of Sequences 1-4. See the caption for more details. Sequence 6 is plotted in Fig. 2.7. Finally, the shape of the rotation curves of Seq. 5 are all similar to the benchmark model, but their amplitude varies as in Fig. 2.8.

2.6.1 Newtonian dynamics

Fig. 2.5 and the first column of Fig. 2.6 show the rotation curves computed using standard *Newtonian* dynamics without dark matter for Sequence 1. As we can see, the velocities at radii larger than approximately 6 kpc are larger in the polar plane. The reason for this is that the closed orbits are much more eccentric in the host galaxy than in the plane of the polar ring due to the compact host galaxy and the extended ring (see Fig. 2.2), and when observing the polar ring galaxy edge-on, the minimum velocities of these eccentric orbits (point A in Fig. 2.2) are measured. The eccentricity can be explained as follows.

The potential due to the compact host galaxy component appears nearly spherical at large[4] radii for test particles in both the plane of the host galaxy and the plane of the polar ring. The potential generated by the extended polar ring, however, does appear spherical to particles orbiting within the ring, but not to particles orbiting in the host plane.[5] This gives rise to lower line-of-sight velocities when the host disk and polar rings are seen edge-on.

At radii smaller than the size of the hole (the region where the density increases with radius), the eccentricity argument turns around. The test particles are near the center of the galaxy and accordingly near the center of the hole of the polar ring. At these radii, all test particles experience the gravitational field caused by the polar ring rather spherically, while the potential by the galactic disk appears spherical only to the test objects orbiting within the disk, not to those moving in the polar plane. The transition appears around approximately 6 kpc, i.e. between the radial size of the galactic disk, which is smaller than 6 kpc, and that of the polar ring, which is larger than 6 kpc.

This ellipticity of the orbits in the host is enhanced by the actual presence of the hole at the center of the polar ring, because, in order to have the same mass in the polar structure as in a corresponding disk, one needs to increase the density at large r in the polar plane, making it more extended (see Fig. 2.3).

2.6.2 Milgromian dynamics

In Milgromian dynamics, all investigated models (see Fig. 2.6) that (i) feature a polar ring (i.e. Sequences 1, 2, 4, 5 and 6), that (ii) has a total mass (i.e. gaseous plus stellar mass) comparable to the mass of the host galaxy (within a factor of ∼2), show higher velocities in the polar plane at radii larger than approximately 6 kpc. Indeed, the reason is the same as in Newtonian dynamics without dark matter, and is even boosted by the additional gravity provided by Milgromian dynamics. Because the host is more compact than the ring, it appears more spherical to particles orbiting in the ring at large radii than the ring appears to particle orbiting in the host at the same radii. Hence, also in Milgromian dynamics, the closed orbits are in the galactic disk more eccentric than in the plane of the polar ring. This gives rise to lower line of sight velocities in the host for typical observed systems where the host and polar rings are seen approximately edge-on. Because Milgromian dynamics adds a disk component of PDM to the host and to the ring (see Fig.2.4), this effect is even amplified compared to Newtonian dynamics.

In Sequence 1 (Fig. 2.6, 1st column), one can see that decreasing the polar ring mass compared to the host gradually cancels the above effect, because the gravity generated by the polar ring becomes more and more negligible when decreasing its mass. For the benchmark model, at a radius of less than approximately 6 kpc, test stars orbiting in the polar ring have smaller velocities than those at the same radius in the host disk, because they are close to or in the polar hole and the mass enclosed by their orbits is comparably small. This transition radius changes to larger radii when decreasing the polar ring mass, to gradually arrive at the situation of no polar ring, where polar orbits have velocities systematically lower than those in the disk (equal at large radii).

The same effect is observed in Sequence 2 (Fig. 2.6, second column) for more massive systems. Note that the velocities in the host decrease with declining polar ring mass, due to the decreasing gravity of the polar ring, but less so than the velocities in the ring. The reason for this slower decrease is that the effect of decreased gravity is compensated by the effect of decreasing eccentricity for particles orbiting in the host.

On the other hand, in Sequence 3 (Fig. 2.6, 3rd column), the rotation velocities are, at radii larger than 15 kpc, very similar in both planes, because of the special symmetry of these models. This emphasizes

[4] In the context of investigated PRG models, large means larger than the size of the host galaxy.

[5] We know this because in Newtonian dynamics the linearity of Poisson's equation allows us to separate and linearly add the different potentials.

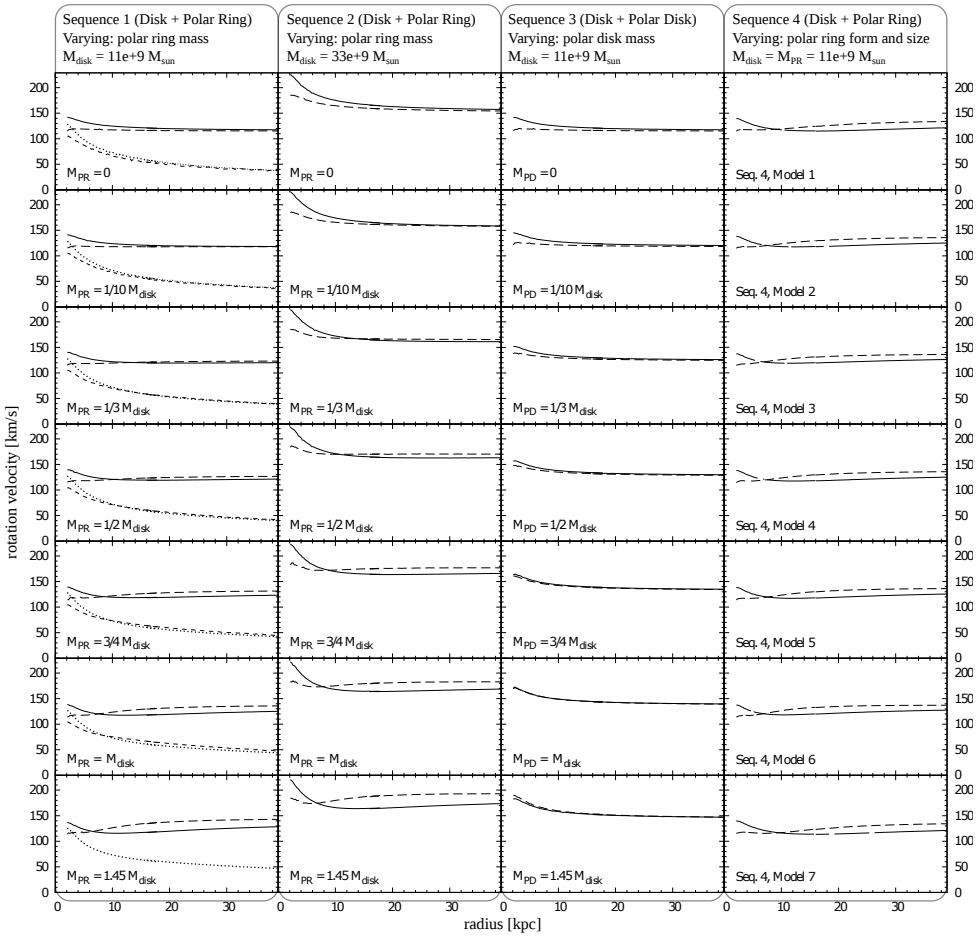

Figure 2.6: The figure presents the rotation curves of all models of Sequence 1 to 4. Solid lines refer to Milgromian rotation velocities in the host galaxy, long-dashed lines to the polar plane. In Seq. 1 also the Newtonian rotation curves are shown (dotted lines: host galaxy; short-dashed: polar ring; no dark matter halo). Sequence 1 features a host disk, a bulge and a polar ring. While the disk mass $M_{\rm disk} = 11 \times 10^9\,{\rm M}_\odot$ is constant, the mass of the polar ring is varied from $M_{\rm PR} = 0 \ldots 1.45\,M_{\rm disk}$ (the bottom left panel shows the benchmark model, see also Fig. 2.5). Sequence 2 is similar to Sequence 1 but is three times as dense and consequently massive ($M_{\rm disk} = 33 \times 10^9\,{\rm M}_\odot$). Sequence 3 features a host disk, a bulge and a polar disk instead of a ring. Models of this sequence have a disk mass of $M_{\rm disk} = 11 \times 10^9\,{\rm M}_\odot$, the mass of their polar component is again variable. Sequence 4 features a host disk, a bulge and a polar ring. Models of this sequence have a fixed total mass $M = 27.1 \times 10^9\,{\rm M}_\odot$ and the size parameters of their polar ring components are variable.

the role played by the hole at the center of the ring in the other Sequences.

Varying the form and size of the stellar and gaseous holes in the polar ring in Sequence 4 (Fig. 2.6, 4th column) shows that for a host and ring of comparable mass, the effect is quite generic in the presence of a hole.

The shape of the rotation curves of Sequence 5 are all similar to the benchmark model, but their amplitude varies and is discussed in Sect. 6.3. Sequence 6 is a series of four different Milgromian potentials computed for the benchmark model for $n = 1, 2, 3, 4$ in Eq. 3.3, and confirms that the qualitative results are independent of the ν-function as illustrated on Fig. 2.7.

Let us finally note that if the host galaxy, here represented by a Miyamoto-Nagai disk, is replaced by a disk that falls off exponentially and therefore much faster, the host galaxy would appear more compact and the described effect would therefore be even stronger at small and intermediate radii, and unchanged at large radii.

2.6.3 Tully-Fisher relation

We compare our theoretically obtained rotation curves to the observed PRGs of Iodice et al. (2003), showing, in Fig. 2.8, the maximal rotational velocities of both the host and polar ring. This gives rise to a luminous Tully-Fisher relation. For the baryonic Tully-Fisher relation (BTFR), we note that Milgromian dynamics predicts $V^4 = a_0 G M_\mathrm{b}$ for spherical systems (McGaugh, 2011b) where V is the asymptotic circular velocity, and M_b the baryonic mass. However, polar ring galaxies are not only non-spherical but also non-axisymmetric objects. Because of this, there is no iron-clad prediction for the BTFR in such objects: our models indicate that the hosts typically exhibit asymptotic velocities below this value of V, while the polar rings are closer to the prediction, but can typically also exceed this velocity.

In order to explore the relevant mass range in our models, the corresponding data points in absolute B-band magnitude vs. rotation velocity are compared to the models of Sequence 5 (which varies the total mass), by assuming a mass to light ratio of $M/L_\mathrm{B} = 4$ as in Combes and Arnaboldi (1996). We assume that the line width $\Delta v_{20} = W_{20} = 2v_\mathrm{max}$ equals twice the maximum line of sight velocity[6].

From observations, the polar rings are generally very extended and feature large quantities of HI gas. The rotation curve in this polar plane can therefore observationally be measured even at large radii where it is very flat. Compared to the ring, the host galaxy is usually rather small and has relatively little gas. The rotation velocity in the host is generally obtained indirectly from the measured stellar velocity dispersion (Iodice et al., 2003, 2006; Iodice, 2010), which means that the maximum velocity is most likely not measured in the very flat part and does therefore not equal the maximum velocity of the theoretical potential derived from the observed density distribution. To account for this issue, the theoretical rotation velocity from the models are computed at both $r = 40\,\mathrm{kpc}$ and $r = 15\,\mathrm{kpc}$, where $v(r = 15\,\mathrm{kpc}) \leq v(r = 40\,\mathrm{kpc})$ (see Fig. 2.5).

In Fig. 2.8, the circles show the rotation velocity measured in the hosts, the arrow heads the ones measured in the polar rings, both for some observed PRGs and for the models of Sequence 5 (circles and squares as per Fig. 2.5). We see that our models reproduce fairly well the observations, with velocities systematically larger in the rings, but also with comparable offsets. Since the benchmark model on which the Sequences are based was inspired from the prototypical PRG galaxy NGC4650A, it comes as no surprise that this PRG is best fitted by these models.

[6] Note that the observed line widths Δv_{20} are converted into velocities by assuming $\Delta v_{20} = 2v_\mathrm{max}$ (e.g. Verheijen, 2001). Depending on line width broadening effects, the actual velocities may be systematically smaller than $\Delta v_{20}/2$. In the context of the theoretical data this would imply that NGC 4650A had actually a smaller mass to light ratio.

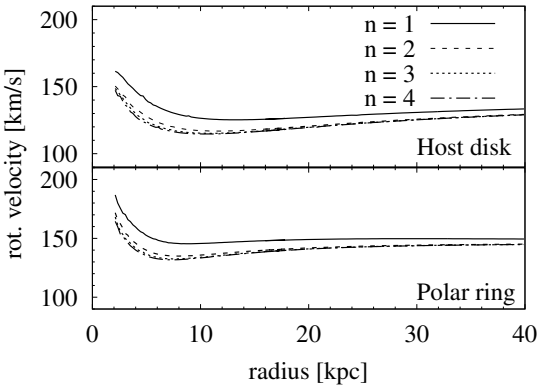

Figure 2.7: Rotation curves of the benchmark model in Milgromian dynamics applying different ν-functions, $\nu_n(x)$ with $n = 1, 2, 3, 4$ in Eq. 3.3.

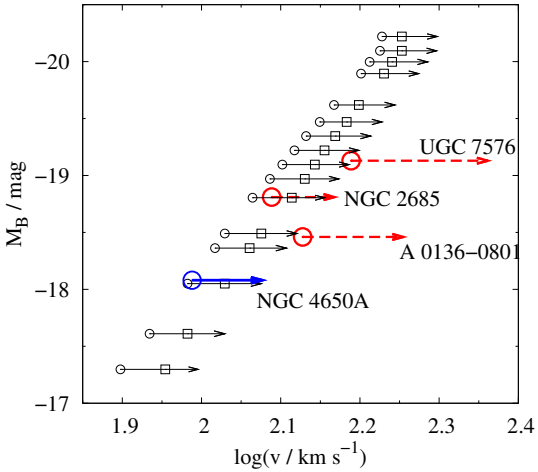

Figure 2.8: Comparison of observational data of PRGs with our numerical results using the luminous Tully-Fisher relation. The plot shows the the absolute B-band luminosity in magnitudes vs. the rotation velocity. Each arrow refers to one galaxy or galaxy model. The blue and red data points are adopted from Iodice et al. (2003) and represent measurements of various PRGs. The circles show the rotation velocity measured in the hosts, the arrow heads the ones measured in the polar rings. The blue data correspond to NGC 4650A. For the theoretical data points (black), the squares show the rotation velocity in the host galaxy at $r = 40$ kpc, the circles show the rotation velocity in the host at $r = 15$ kpc (where it is actually measured), the arrow heads point to the polar ring rotation velocity at $r = 40$ kpc. The theoretical data are obtained from models of Sequence 5. The absolute B-band magnitude is calculated from the total mass using a mass to light ratio of $M/L_B = 4$ like was assumed by Combes and Arnaboldi (1996).

2.7 Conclusions

The conclusion from all the investigated models, and the bottom line of this study, is that Milgromian dynamics naturally predicts that rotation velocities would be higher in the polar rings than in the hosts. This generically happens when the ring is more extended than the host and of comparable mass and both are observed approximately edge-on. It does not apply to faint polar rings, or to polar rings of similar radial size as the host. Given the wide range of model parameters covered within this study, this general result appears quite robust in Milgromian dynamics. What is more, the magnitude of the velocity offset predicted by the models is also comparable to the observed one (see Fig. 2.8). We however did not attempt to precisely fit the full rotation curves of individual polar ring galaxies, which will be the subject of future work, based on observations performed on a sample of 10 such systems at the Westerbork Synthesis Radio Telescope (WSRT).These and other upcoming precise measurements of rotation curves of individual polar ring galaxies (e.g. the future measurements announced in Iodice, 2010) should thus allow more stringent tests, and these will become benchmark objects with which to test gravity in the coming years.

CHAPTER 3

A census of the expected properties of classical Milky Way dwarfs in Milgromian dynamics

Published in
MNRAS, Volume 441, Issue 2, p. 2497–2507
May 2014

DOI: 10.1093/mnras/stu757

F. Lüghausen, B. Famaey, and P. Kroupa

Abstract

Prompted by the recent successful predictions of the internal dynamics of Andromeda's satellite galaxies, we revisit the classical Milky Way dwarf spheroidal satellites Draco, Sculptor, Sextans, Carina, and Fornax in the framework of Milgromian dynamics (MOND). We use for the first time a Poisson solver with adaptive mesh refinement (AMR) in order to account simultaneously for the gravitational influence of the Milky Way and its satellites. This allows us to rigorously model the important external field effect (EFE) of Milgromian dynamics, which can reduce the effective acceleration significantly. We make predictions on the dynamical mass-to-light ratio ($M_{\rm dyn}/L$) expected to be measured by an observer who assumes Newtonian dynamics to be valid. We show that Milgromian dynamics predicts typical $M_{\rm dyn}/L \approx 10$–$50\,{\rm M}_\odot/{\rm L}_\odot$. The results for the most luminous ones, Fornax and Sculptor, agree well with available velocity dispersion data. Moreover, the central power-law slopes of the dynamical masses agrees exceedingly well with values inferred observationally from velocity dispersion measurements. The results for Sextans, Carina and Draco are low compared to usually quoted observational estimates, as already pointed out by Angus. For Milgromian dynamics to survive further observational tests in these objects, one would thus need that either (a) previous observational findings based on velocity dispersion measurements have overestimated the dynamical mass due to, e.g., binaries and contaminant outliers, (b) the satellites are not in virial equilibrium due to the Milky Way tidal field, or (c) the specific theory used here does not describe the EFE correctly (e.g., the EFE could be practically negligible in some other theories), or a combination of (a)–(c).

3.1 Introduction

Data on large scale structures, when interpreted in terms of Einstein's field equations, point towards a Universe dominated by dark energy and dark matter. Dark energy is generally represented by a cosmological constant, Λ, and dark matter (DM) is most often assumed to be made of hitherto undetected massive elementary particles, the so-called cold dark matter (CDM). Models based on less massive particles, so-called warm dark matter (WDM) lead largely to the same results, apart from some mild differences in the minimum mass of DM haloes and the presence of small constant density cores at their centre (Macciò et al., 2012). However, at galaxy scales, the observations are in disagreement with many predictions based on particle DM (e.g. Kroupa et al., 2010; Kroupa, 2012), whilst the observation of a tight correlation between the distribution of baryonic and missing mass seems to indicate that the effective law of gravity is well-described by Milgromian dynamics particularly in rotationally supported galaxies (Milgrom, 1983, see Famaey and McGaugh, 2012 for a major review, and also Hernandez et al., 2014, Trippe, 2014), rather than Newtonian dynamics plus DM.

The specific observed dynamics of spiral galaxies can be interpreted as becoming scale-invariant under transformations $(t, \boldsymbol{x}) \rightarrow (\lambda t, \lambda \boldsymbol{x})$ with $\lambda \in \mathbb{R}$ when the accelerations fall well below the threshold acceleration $a_0 \approx 10^{-10}\,\mathrm{m\,s^{-2}} \approx \Lambda^{1/2}$. This is mostly equivalent to stating that, in spherical symmetry, the gravitational attraction then approximately approaches $(g_{\rm N} a_0)^{1/2}$, where $g_{\rm N}$ is the classical Newtonian gravitational acceleration due to the baryonic matter. This prescription, known as Milgromian dynamics, leads to a large body of remarkable predictions in galaxies (Famaey and McGaugh, 2012). A general consequence of such dynamics is that, unlike Newtonian dynamics, it is nonlinear even in the nonrelativistic regime, meaning that it cannot satisfy the strong equivalence principle. For example, in the case of a satellite galaxy orbiting a more massive host galaxy, the satellite's internal dynamics is not independent from the acceleration it feels due to the external field of the host galaxy. The effect of this external acceleration on the internal dynamics of a system is known as the external field effect (EFE), and is very different from the tidal effect. For objects such as satellite galaxies, rigorously taking into account the EFE requires to account simultaneously for the gravitational influence of the host and the internal gravitational field of the satellites. In this work, we revisit the dynamics of dwarf spheroidal satellites of the Milky Way (MW) by making use of an advanced Poisson solver with adaptative mesh refinement (AMR).

Such dwarf spheroidal galaxies orbiting around more massive hosts range from 10^3 to $10^7\,\mathrm{L}_\odot$ with half-light radii of about 500 pc to 1 kpc. Two kinds of dwarf galaxies must exist in the framework of the standard cosmological model (Kroupa, 2012, and the references therein): primordial dwarf galaxies (PDGs) and tidal dwarf galaxies (TDGs). PDGs formed early in the universe and are supposed to be embedded in small CDM haloes. Cosmological simulations have shown that a large number of PDGs as massive as $10^8\,\mathrm{M}_\odot$ and more should have formed as satellites orbiting the MW (Klypin et al., 1999; Moore et al., 1999). These primodial galaxies do not have preferred orbits and are thus roughly spherically distributed around the host, or only moderately flattened (Wang et al., 2013), and move in arbitrary directions. Even accretion from cold filaments has been demonstrated to not yield significant anisotropies (Pawlowski et al., 2012a). TDGs on the other hand are dwarf galaxies resulting from major encounters of galaxies. In such encounters, gas and stars are stripped off the galaxies through tidal forces and form large tidal debris tails within which dwarf galaxies can form. Contrary to PDGs, TDGs can have only little or no cold or WDM (Barnes and Hernquist, 1992; Bournaud, 2010) and are clearly correlated in phase-space if they originate from the same event. They typically form vast disc-like structures around their past-encounter hosts.

Because the found dwarf spheroidal galaxies around the MW are observed to have extraordinary high dynamical mass-to-light ratios (e.g., Mateo et al., 1991; Strigari et al., 2008; Walker et al., 2009; Walker,

2013; Battaglia et al., 2013), they are generally thought to be PDGs enclosed in CDM subhaloes (e.g., Belokurov, 2013). There are, however, a number of problems with this interpretation. The oldest one is known as the missing satellite problem: while there should be more than 500 nearly isotropically distributed CDM subhaloes with bound masses of $\gtrsim 10^8\,M_\odot$ with a tidally limited size of $\gtrsim 1\,\mathrm{kpc}$ (Moore et al., 1999), only 11 bright satellites have been detected (and only about 26 are known in total). It has been subsequently assumed that gas had collapsed to form substantial stellar populations only in some 'lucky' CDM subhaloes, whilst the others would have lost their baryons or had stellar formation quenched for a variety of reasons (e.g. Brooks et al., 2013), ranging from stellar feedback to tidal forces and reionization. Nevertheless, even in semi-analytical models taking such effects into account, there remain problems at the low-mass and high-mass end (e.g., Kroupa et al., 2010). For instance, the most massive subhaloes of the MW in CDM simulations are too dense to host any of its bright satellites (this is known as the 'too big to fail' problem; Boylan-Kolchin et al., 2011), leaving as a mystery why these massive haloes failed to form galaxies.

Moreover, a second and even more problematic observation is that the dwarf spheroidal satellite galaxies of the MW are arranged in a corotating, vast polar structure (VPOS, Pawlowski et al., 2012b), which is completely incompatible with the predictions from CDM simulations. The same problem arises in the Andromeda galaxy (Ibata et al., 2013) where half of the satellites are rotating in an extremely thin planar structure oriented towards the MW.

The strong phase-space correlation of the satellites suggests that the observed satellites are not PDGs but TDGs. While this conclusion seems natural, it is in contradiction with CDM, because the dwarf satellites of the MW are observed to have very high dynamical mass-to-light ratios. The observations by Bournaud et al. (2007) also emphasize this conflict around external galaxies: they observe currently forming TDGs in the tidal debris of a galactic encounter, and these TDGs also possess a large amount of missing mass. This missing mass can, in the standard picture, only be explained by large amounts of unseen, presumably cold, molecular gas. The flat rotation curves of these dwarfs on the other hand are inconsistent with this expedient as they would require this baryonic DM to be distributed in an isothermal fashion. On the contrary, these rotation curves are well explained by Milgromian dynamics without any free parameters (Gentile et al., 2007).

So, if the conclusion that the MW dSphs are of tidal origin is true, the observed high dynamical mass-to-light ratios would imply that these objects are either out of equilibrium (Kroupa, 1997; Klessen and Kroupa, 1998; Casas et al., 2012) or that a modified gravity scheme, such as those based on Milgromian dynamics, applies, or both. In the latter case, only those galaxies that appear to be in dynamical equilibrium should be compared to the static predictions of Milgromian dynamics (McGaugh and Wolf, 2010).[1] In the view of Milgromian dynamics, the tidal scenario seems very natural. Timing arguments suggest that M31 and the MW must have had a close tidal encounter, likely 7–11 Gyr ago (Zhao et al., 2013). In the standard model, this simple tidal encounter scenario is not possible at all, because the dynamical friction between the CDM haloes of the two encountering galaxies would lead to a galactic merger. The formation of TDGs around the MW could however be explained by other scenarios, e.g. the one modelled by Hammer et al. (2013), but it is still in contradiction to the observed high amount of missing matter in these objects.

Since apparent high dynamical masses[2] (deduced when using classical Newtonian dynamics) are a natural property of Milgromian dynamics for objects of low surface density (Famaey and McGaugh, 2012), it is thus of high interest to predict what should be expected for the MW dwarf satellites in this

[1] While the faintest dwarf spheroidals show clear sign of being out of equilibrium, this is not the case for the most massive ones.

[2] The dynamical mass is the mass derived from the measured velocity dispersion under certain assumptions, e.g. dynamical equilibrium, while applying Newtonian dynamics.

context. This was pioneered for the MW dwarf spheroidals by Milgrom (1995), Brada and Milgrom (2000), Angus (2008) and Hernandez et al. (2010), while predictions for the Andromeda dwarfs were made by McGaugh and Milgrom (2013a) and McGaugh and Milgrom (2013b). Correct a priori predictions were for instance made for the velocity dispersions of AndXVII, AndXIX, AndXX, AndXXI, AndXXIII, AndXXV, AndXXVIII. Among these, some are seen as outliers from the mass–luminosity–radius relations within the CDM paradigm because of their large size and low velocity dispersions, for instance AndXIX, AndXXI and AndXXV. On the contrary, these low velocity dispersions were correctly predicted a priori in Milgromian dynamics thanks to the EFE (McGaugh and Milgrom, 2013b).

All these studies had the drawback of having to treat the EFE of Milgromian dynamics in a non-self-consistent manner. The external field indeed has a major influence on the predicted effective dynamical mass and has to be taken into account very carefully. This has recently been done properly in the work of Angus et al. (2014) but without AMR, not allowing as much flexibility to study the various effects on vastly different scales. Here, we take advantage of the Milgromian Poisson solver with AMR, which we developed in the course of a larger project, in order to account simultaneously for the gravitational influence of the MW and its satellites. As a first application, we thus revisit the predictions for the brightest MW dwarfs, making predictions on the objects' dynamical mass-to-light ratios ($M_{\rm dyn}/L$) expected to be measured when assuming Newtonian dynamics to be valid.

3.2 Milgromian dynamics

Milgrom's simple formula, that is

$$g = (g_{\rm N} a_0)^{1/2} \tag{3.1}$$

if $g_{\rm N} \ll a_0$ (Milgrom, 1983), as such cannot be a final theory of gravity (e.g., no conservation of momentum). This formula arises from the approach of scale-invariance symmetry of the equations of motion under transformation $(t, r) \rightarrow (\lambda t, \lambda r)$ with $\lambda \in \mathbb{R}$ (Milgrom, 2009d), and applies to spherically symmetric systems only. One can however derive theories of gravity that yield Milgrom's formula in spherical symmetry. To date, many different generally covariant modified gravity theories reproducing Milgromian dynamics have been developed (Bekenstein, 2004; Zlosnik et al., 2007; Milgrom, 2009a), and even at the classical level, various modified Poisson equations exist. While they could slightly differ out of spherical symmetry (Zhao and Famaey, 2010), the general predictions for dwarf spheroidal galaxies should be similar in all of these. One recent formulation (Milgrom, 2010) has the following Poisson equation:

$$\nabla^2\Phi = 4\pi G\rho_{\rm b} + \nabla \cdot \left[\nu\left(|\nabla\phi|/a_0\right)\nabla\phi\right], \tag{3.2}$$

where $\rho_{\rm b}$ is the baryonic density, Φ is the total (Milgromian) potential, ϕ is the Newtonian potential such that $\nabla^2\phi = 4\pi G\rho_{\rm b}$, and $\nu(x) \rightarrow 0$ for $x \gg 1$ and $\nu(x) \rightarrow x^{-1/2}$ for $x \ll 1$. A family of functions fulfilling this definition of $\nu(x)$ (see, e.g. Famaey and McGaugh, 2012) is

$$\nu(x) = \left[1 + (1 + 4x^{-n})^{1/2}/2\right]^{1/n} - 1. \tag{3.3}$$

In the following, when not stated otherwise, we use the $n = 1$ function, which is known to reproduce well the rotation curves of most spiral galaxies.

The second term in equation (4.2) can be thought to be the matter density distribution $\rho_{\rm ph}$ that would, in Newtonian gravity, yield the Milgromian boost to gravity, and is known as the "phantom dark matter" (PDM) density:

$$\rho_{\rm ph} = \frac{\nabla \cdot \left[\nu\left(|\nabla\phi|/a_0\right)\nabla\phi\right]}{4\pi G}. \tag{3.4}$$

This PDM density is not a real physical object but is only a mathematical description that allows us to solve the Poisson equation for Milgromian dynamics with only linear differential equations and one simple, algebraic step. In the framework of Newtonian dynamics, this mathematical source of gravity would be interpreted as missing matter or DM.

3.2.1 Computing the effective dynamical masses predicted by Milgromian dynamics

The PDM density that would source the Milgromian force field in Newtonian gravity is defined by equation (3.4) and can be computed from the known classical (Newtonian) potential $\phi(\boldsymbol{x})$. To evaluate this term on a Cartesian grid, we make use of the grid-based scheme that has been devised by Lüghausen et al. (2013).

In order to treat the host and the satellite galaxies simultaneously, we implemented this scheme into the Ramses code (Teyssier, 2002): in this work, we make use of its Poisson solver (see Guillet and Teyssier, 2011, for a detailed description) and the available AMR infrastructure (AMR, Kravtsov et al., 1997; Teyssier, 2002) to compute the effective Milgromian potential from the given distribution of baryonic matter. Starting from a coarse Cartesian grid, the AMR technique allows us to refine this grid on a cell-by-cell and level-by-level basis in the regions of interest: each cell which exceeds a given particle density (or equivalently barynonic mass density) is split into 2^3 sub cells. This way, the potential of a large physical box containing structures of very different mass densities and sizes can be computed efficiently at a single time. In this work, we make use of this benefit and start with a bounding box that has a size that is large enough to host a Galaxy model at the centre as well as the satellite galaxies at their known positions. At the centre of this box, we place a three-dimensional mass density model of the MW determined by McGaugh (2008b). At the box boundaries, we use the Dirichlet boundary conditions $\phi(r) = GM_\mathrm{b}/r$ with $\phi(r)$ being the Newtonian potential at the distance r to the centre of mass (of the whole baryonic density grid), and total baryonic mass M_b, to solve the Poisson equation for the Newtonian potential $\phi_N(\boldsymbol{x})$. From this discrete potential, we compute the PDM density (equation 3.4) using the prescription from Lüghausen et al. (2013, their equation 4).

To find the gravitational potential $\Phi(\boldsymbol{x})$ predicted by Milgromian dynamics, the resulting PDM density, $\rho_\mathrm{ph}(\boldsymbol{x})$, is added to the baryonic mass density, $\rho_\mathrm{b}(\boldsymbol{x})$. Poisson's equation, $\nabla^2\Phi(\boldsymbol{x}) = 4\pi G(\rho_\mathrm{b}(\boldsymbol{x}) + \rho_\mathrm{ph}(\boldsymbol{x}))$, now with the total effective dynamical mass (baryonic matter + PDM), is solved a second time, now using the boundary condition (see Eq. 20 in Famaey and McGaugh, 2012)

$$\Phi(r) = (GM_\mathrm{b}a_0)^{1/2}\ln(r) \tag{3.5}$$

on the last grid point at the distance r to the centre of mass of the *baryonic* density grid with total baryonic mass M_b.

In this work, we consider only static models of the MW satellites and use the PDM density to predict the effective dynamical mass[3] of these satellite galaxies. The grid is resolved to a resolution of 10 pc and less (the typical half-mass radius of the considered dSphs is of the order of $500 - 1000$ pc). The resolution limit is visible in the logarithmic plots at small radii, r.

[3] We prefer to use the term 'dynamical mass-to-light ratio' rather than classically just 'mass-to-light ratio', because in the Milgromian picture, PDM is not real matter but a mathematical construction. Dynamical mass however makes clear that we refer to the baryonic mass plus the DM equivalent as deduced by a Newtonian observer in a Milgromian universe.

3.2.2 External field effect (EFE)

Contrary to classical, linear, Newtonian dynamics, Milgromian dynamics is described by a non-linear theory and breaks the strong equivalence principle. As a consequence, the internal dynamics of a satellite system (e.g. dSphs around the MW, or galaxies in the external field of a galaxy cluster) does not decouple from the external field produced by its mother system. This means, the external field can drastically reduce the 'acceleration boosting effect' of Milgromian dynamics with respect to classical dynamics, it can even break it completely down to Newtonian behaviour if the external acceleration (and thus the 'total' acceleration) is larger than a_0. If $g_{\rm N,ext}$ is the external (Newtonian) acceleration, and $g_{\rm N,int}$ the internal one, then the EFE does not play a role if

$$g_{\rm N,ext} \ll g_{\rm N,int} \,.$$

In this case, the system is in the Newtonian or Milgromian regime, and its dynamics depends only on $g_{\rm N,int}$.[4] On the other hand, if the acceleration due to the external field dominates and is in the Newtonian regime,

$$g_{\rm N,int} < a_0 \ll g_{\rm N,ext} \,,$$

the external acceleration field takes over and the internal dynamics appear purely Newtonian even when $g_{\rm N,int} < a_0$. In between these extreme cases, i.e. if the external field dominates but is itself well below a_0,

$$g_{\rm N,int} < g_{\rm N,ext} < a_0 \,,$$

the system is then Newtonian with a renormalized gravitational constant (Famaey and McGaugh, 2012). That is, in the framework of QUMOND, the spatial distribution of the PDM density is proportional to that of the baryons, $\rho_{\rm ph}(\boldsymbol{x}) \propto \rho_{\rm b}(\boldsymbol{x})$. This is referred to as the quasi-Newtonian regime. The exact behaviour of the EFE finally depends on the particular theory, and particularly on the applied ν-function. This peculiar property of any theory implementing Milgromian dynamics is in contrast to the experience of our classical Newtonian thinking and challenges our intuition.

The EFE has another remarkable consequence that concerns the cusp/core problem (de Blok, 2010): while simulations show that haloes made of CDM have cuspy profiles with a central matter density profile, $\rho(r) \propto r^{\alpha}$, that has a power-law slope of approximately $\alpha_{\rm NFW} = {\rm d}\log\rho_{\rm NFW}(r)/{\rm d}\log r|_{r\to 0} = -1$, the profiles of the effective dynamical mass (observationally inferred from measured velocity dispersions) of observed dSphs appear to be cored[5] (e.g., Walker and Peñarrubia, 2011), i.e. $\alpha_{\rm DM/ph} \approx 0$. In Milgromian dynamics, the power-law slope is expected to be ≈ -0.5 if the model is isolated (i.e. without external field) and if the baryonic matter density distribution itself is cored (Milgrom, 2009c). The EFE can however reduce this slope from ≈ -0.5 to ≈ 0 if the galaxy's dynamics are dominated by the external field, because in this case the PDM profile has the same shape as the baryonic matter profile with a different normalization constant (see above), i.e. $\alpha = {\rm d}\log\rho_{\rm ph}(r)/{\rm d}\log r|_{r\to 0} \approx {\rm d}\log\rho_{\rm b}(r)/{\rm d}\log r|_{r\to 0} \approx 0$. We discuss in the results section how this applies to each object individually. In Section 3.4.1 and Fig. 3.1, we demonstrate how an example model of a MW satellite is affected by the gravitational potential of its host galaxy.

In the course of this work, the EFE is self-consistently implemented, because the computed models contain the MW and its satellite all at one time.

[4] However, even in this regime, the external field induces a small quadrupole which can, e.g., be measured with high-precision experiments in the Solar system (Milgrom, 2009b; Hees et al., 2014).

[5] In the literature, the term "cuspy" is commonly used if the powerlaw slope is steeper (i.e. less) than the inner slope of the NFW profile, $\alpha < -1$, while "cored" refers to $\alpha > -1$.

	$r_{\rm king}$/kpc	$r_{\rm lim}$/kpc	$L_V/(10^5\,{\rm L}_\odot)$	D/kpc	$D_{\rm min}$/kpc	$D_{\rm max}$/kpc
Fornax	0.429	2.972	188	151.9	140.3	164.6
Sculptor	0.305	1.773	25.4	87.0	81.8	92.6
Sextans	0.432	4.321	5.8	92.9	81.1	96.9
Carina	0.281	0.919	5.0	109.2	103.2	115.7
Draco	0.173	0.894	2.4	76.9	71.3	82.9

Table 3.1: List of all King models used. The model parameters (King radius, limiting radius and luminosity) are adopted from Strigari et al. (2008) and are scaled appropriately for the considered distances D, $D_{\rm min}$ and $D_{\rm max}$, where D is the most likely distance (between the object and the Sun) and $D_{\rm min}$ and $D_{\rm max}$ are the minimum and the maximum distances (1-σ deviation of D along the line of sight). The distances are adopted from the compilation of McConnachie (2012). The respective Galactocentric distances and positions are provided in Table 3.2.

	Position $[x, y, z]$/kpc	R/kpc	$R_{\rm min}$/kpc	$R_{\rm max}$/kpc
Fornax	$-41.5, -51.0, -134.1$	149.4	162.0	137.7
Sculptor	$-5.4, -9.8, -85.3$	86.0	91.7	80.7
Sextans	$-36.9, -56.9, 57.8$	89.1	93.1	85.2
Carina	$-25.2, -95.9, -39.8$	106.8	113.4	100.8
Draco	$-4.6, 62.2, 43.2$	75.9	70.2	82.0

Table 3.2: List of all positions in Galactic coordinates (MW centre at $[0, 0, 0]$, Sun at $[8.5\,{\rm kpc}, 0, 0]$) from McConnachie (2012). R is the according distance to the Galactic Centre. The satellite positions are varied along the line of sight within the 1σ measurement errors (see also McConnachie, 2012). $R_{\rm min}$ and $R_{\rm max}$ are the distances to the Galactic Centre at the positions closest to and farthest away from the Sun respectively.

3.3 Models

3.3.1 Dwarf spheroidal models

Dwarf spheroidals are quasi-spherical galaxies, the observed density profiles are mostly well fitted by King density models (King, 1966),

$$\rho(r) \propto \frac{\arccos(z)/z - \sqrt{1-z^2}}{\pi r_{\rm king}\left[1 + \left(r_{\rm lim}/r_{\rm king}\right)^2\right]^{3/2} z^2} \tag{3.6}$$

with $z^2 = \left(1 + r/r_{\rm king}\right)^2 / \left(1 + r_{\rm lim}/r_{\rm king}\right)^2$ (King, 1962). King model fits have been performed for the classical dSphs e.g. by Strigari et al. (2008), for reviews see Ferguson and Binggeli (1994) and Mateo (1998). We adopt the King models and scale the given luminosities and size parameters to the recent distances compiled by McConnachie (2012). The model parameters are listed in Table 3.1, their positions in Galactocentric coordinates in Table 3.2.

In this work, we consider the so-called classical (luminous) dwarf spheroidal galaxies, ordered by decreasing total luminosity. We do not include Ursa Minor (UMi), because it appears to be out of equilibrium (Kleyna et al., 2004). For each object, we investigate the following 11 models.

- At the most likely distance to the Sun (given by McConnachie, 2012), we provide models with $M_*/L = 1, 2, 3, 4,$ and $5\,{\rm M}_\odot/{\rm L}_\odot$. These models are plotted with black solid lines (Figs 3.5–3.9).

- At the minimum and maximum distance (given by the 1-σ errors), we provide models with $M_*/L = 1$ and $5\,\mathrm{M}_\odot/\mathrm{L}_\odot$ to demonstrate how the distance error transfers to the results. These models are plotted with purple ($D_{\max}$) and orange ($D_{\min}$) solid lines (Figs 3.5–3.9).

- We further provide isolated models without external field with $M_*/L = 1$ and $5\,\mathrm{M}_\odot/\mathrm{L}_\odot$ (grey solid lines in Figs 3.5–3.9). For each galaxy, the isolated model with $M_*/L = 5\,\mathrm{M}_\odot/\mathrm{L}_\odot$ represents the upper limit of $M_{\rm dyn}/L$ that can be achieved with this implementation of Milgromian dynamics.[6]

3.3.2 MW model

We use one of the MW mass model from McGaugh (2008a). The model features a stellar exponential disc with scale length of $R_{\rm d} = 2.3\,\mathrm{kpc}$, scaleheight of 0.3 kpc, and a total mass of $4.9 \times 10^{10}\,\mathrm{M}_\odot$. Moreover, it has a thin gaseous disc of $1.2 \times 10^{10}\,\mathrm{M}_\odot$ and a bulge made of a Plummer model with $0.6 \times 10^{10}\,\mathrm{M}_\odot$ and a half-mass radius of 1 kpc.

Although the MW potential is modelled in much detail, this is not crucial, because the spatial size of the satellites is much smaller than the size of the MW disc and their Galactocentric distances (which are 80 kpc and more). More important are the total masses of the individual Galactic components.

In the Galactocentric coordinate system we use, the Sun is located at the x-axis at 8.5 kpc. All specified Galactocentric coordinates are given with respect to this system. The positions of the satellite galaxy models are varied along their line of sight as seen from the position of the Sun.

3.4 Discussion of the model variables

The used dSph models are determined by (i) the density model and its parameters, (ii) the total luminosity, (iii) the stellar mass-to-light ratio[7] and (iv) the position with respect to the Galactic Centre which specifies the external gravitational field felt by the satellite galaxy. In the literature, a large number of different models with different parameters can be found for each of the dSphs. In the following subsections, we start with toy models based on the Sculptor model (see Section 3.5.2) to investigate and discuss in which way the available variables affect the dynamical mass-to-light ratio, $M_{\rm dyn}/L$, as expected by the applied formulation of Milgromian dynamics. Remember that $M_{\rm dyn}/L$ is the dynamical mass-to-light ratio deduced from the dynamics of the stars by an observer when using Newtonian dynamics. This approach is intended to provide the reader a basic understanding of how the model parameters (particularly the external field and the stellar mass-to-light ratio) affect the PDM halo in the Milgromian picture of galactic dynamics.

3.4.1 The external field

Because Milgromian dynamics is, by virtue of its scale-invariant property, acceleration-based, the external gravitational field plays always a prominent role (see Section 3.2.2). Fig. 3.1 demonstrates how the external field affects the shape of the PDM halo of a sample dSph model. The thick solid lines shows the Sculptor model (with $D = 87\,\mathrm{kpc}$, $M_*/L = 3\,\mathrm{M}_\odot/\mathrm{L}_\odot$; see Section 3.5.2) in isolation or without external field, i.e. at infinite Galactocentric distance. If the distance of this satellite model to the centre of the Galactic potential is decreased, i.e. the strength of the external gravitational field is increased,

[6] Under the aforementioned assumptions/simplifications like spherical symmetry and dynamical equilibrium.

[7] In the more general context, “stellar mass-to-light ratio" should actually mean “baryonic mass"-to-“stellar light" ratio, because it relates the stellar luminosity to the baryonic mass of an object, which includes not only stellar mass, but all kind of baryonic matter. In the case of the dSphs, this is the same, because there is essentially no gas.

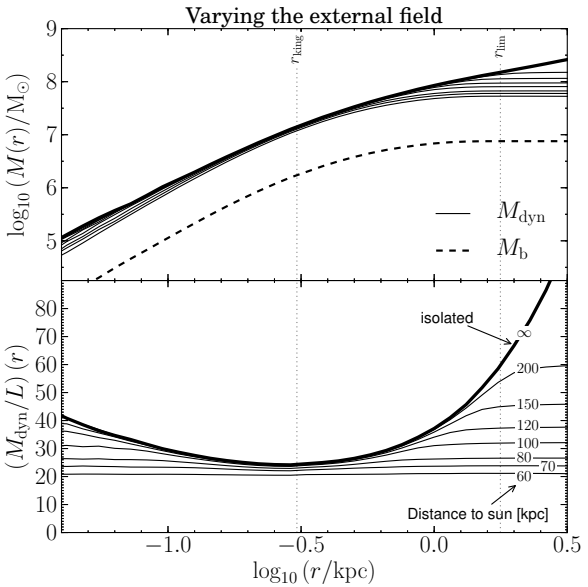

Figure 3.1: The lines show the cumulative mass profiles of the same King model (based on Sculptor with $M_*/L = 3\,\mathrm{M}_\odot/\mathrm{L}_\odot$, $D = 87\,\mathrm{kpc}$) at different Galacticocentric distance to illustrate the effect of the external field (see Section 3.4.1). Top panel: the cumulative mass (the assumed baryonic mass and the predicted dynamical mass) enclosed within the radius r is shown. Bottom panel: the ratio of the effective dynamical mass (phantom DM + baryonic matter) to the baryonic matter content are presented as a function of distance r to the centre of the dwarf galaxy. The thick solid line shows the model in isolation, i.e. without external Galactic field. For the detailed description see Section 3.4.1.

the total mass of its PDM halo decreases (i.e. the effect of Milgromian dynamics weakens). This is because the overall acceleration in the satellite galaxy is enhanced by the external field, which affects particularly the central and outer regions (where the internal Newtonian acceleration, $g_{\rm N}$, is low) because of the non-linearity of $\nu(x)$. As the external field increases, it "cuts off" the PDM density in the lowest-internal-acceleration parts (see the upper panel of Fig. 3.1), making the PDM density follow the baryonic density, until the dynamical mass-to-light ratio appears nearly constant at all r (see the lower panel of Fig. 3.1). In the latter case, the external field of the MW dominates the satellite's internal dynamics ($g_{\rm N,int} < g_{\rm N,ext} < a_0$). Consequently, in this case the satellite's effective dynamical mass profile follows its baryonic mass profile, $\rho_{\rm dyn}(r) \propto \rho_{\rm ph}(r) \propto \rho_{\rm b}(r)$. Moreover, this means that, if the shape of the baryonic matter density is cored, also the PDM halo has to be cored in this external field-dominated case (cf. Section 3.2.2).

As the internal + external acceleration approaches the limit $g_{\rm N,int} + g_{\rm N,ext} \gg a_0$, the dynamical mass to light ratio approaches the stellar one, $M_{\rm dyn} \to M_*$.

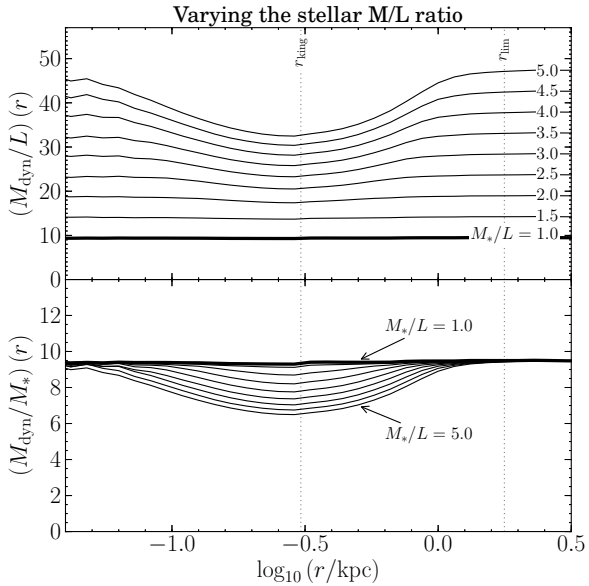

Figure 3.2: Each line shows the same model (based on Sculptor) with different stellar mass-to-light ratios, M_*/L (the total stellar luminosity, L, is kept constant, $D = 87\,$kpc). This sequence of models demonstrates the impact of the M_*/L uncertainty on the $M_{\rm dyn}/L$ ratio predicted by Milgromian dynamics. Top panel: the cumulative mass (the assumed baryonic mass and the predicted dynamical mass) enclosed within the radius r is shown. Bottom panel: the ratio of the effective dynamical mass (phantom DM + baryonic matter) to the baryonic matter content are presented as a function of distance r to the centre of the dwarf galaxy. The thick solid line shows the model in isolation, i.e. without external Galactic field. For the detailed description see Section 3.4.2.

3.4.2 Stellar mass-to-light ratio, M_*/L

The total mass of a stellar system is commonly inferred from the total luminosity, L, by knowing the or assuming a reasonable stellar mass-to-light ratio, M_*/L. In most cases, the value of this variable is not well constrained and left as a fit parameter. The dynamical mass-to-light ratio prediction (within the framework of Milgromian dynamics viewed by a Newtonian observer) however is very sensitive to this quantity, because the dynamical mass density distribution is computed from the baryonic density distribution. We evaluate all models with $M_*/L = 1$ and $5\,{\rm M}_\odot/{\rm L}_\odot$ to provide lower and upper limits on $M_{\rm dyn}/L$.

Again based on the Sculptor model, Fig. 3.2 shows how the predicted dynamical mass-to-light ratio, $M_{\rm dyn}/L$, changes with M_*/L, where $1, \ldots, 5\,{\rm M}_\odot/{\rm L}_\odot$ is a reasonable range for the stellar mass-to-light ratio for these dwarf spheroidals.

If $M_*/L = 1\,{\rm M}_\odot/{\rm L}_\odot$, the satellite galaxy is dominated by the external field of the MW but is still in the deep Milgromian regime ($g_{\rm N,int} < g_{\rm N,ext} \ll a_0$, cf. Section 3.2.2),[8] and the satellite's effective dynamical mass profile thus follows its baryonic mass profile, so that the dynamical mass-to-light ratio, $M_{\rm dyn}/L$, is constant at all radii r, and $M_{\rm dyn}/L \propto M_*/L$.

[8] In this particular model, this is the case if $M_*/L \lesssim 2$.

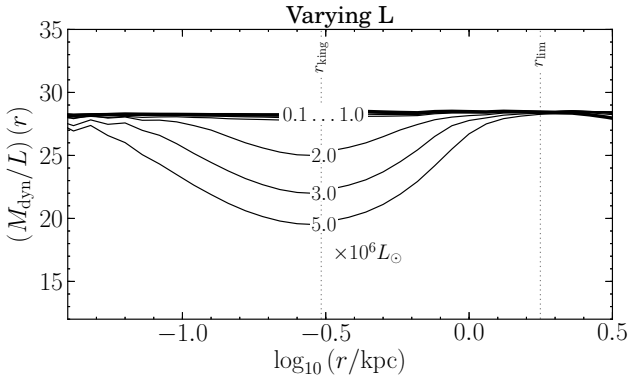

Figure 3.3: The ratio of the predicted effective dynamical mass to baryonic matter is plotted as a function of radius. The shown models are based on Sculptor ($M/L = 3\,\mathrm{M}_\odot/\mathrm{L}_\odot$, $D = 87\,\mathrm{kpc}$), the total luminosity, L, is varied. See also the description in Section 3.4.3.

If M_*/L (and thus the baryonic density and accordingly $g_{\rm N,int}$) is increased ($M_*/L \gtrsim 2$), the external field becomes less dominant, $g_{\rm N,ext} < g_{\rm N,int} < a_0$, while staying in the deep Milgromian regime. The strength of the EFE is decreased and the observable dynamical mass-to-light ratio (observationally inferable from velocity dispersion measurements) would then become radius-dependant (see Fig. 3.2).

3.4.3 Total luminosity, L

Varying the total luminosity, L, means varying the total mass (because the stellar mass-to-light ratio is kept constant) and thus varying the average density (because the size parameters are kept constant as well) and accordingly $g_{\rm N,int}$ varies. Fig. 3.3 shows the dynamical mass-to-light ratio of the Sculptor model for different L. As long as the total mass is small such that the internal dynamics is dominated by the external field, the dynamical mass-to-light ratio predicted by Milgromian dynamics does not depend on L. But as the baryonic mass increases and the internal accelerations get to the order of a_0, this degeneracy vanishes and $M_{\rm dyn}/L$ becomes radius-dependant.

3.4.4 Density model and its radial parameters

For each dSph galaxy, a number of different models and fits can be found in the literature. These are Plummer and King models, exponential profiles, power-law profiles and also the profile derived by Zhao (1997). In most cases, the truncated King model provides the best fit to the observed luminosity profiles.

To demonstrate visually the influence of the external field on the dynamical mass-to-light ratio (see Fig. 3.4), we vary, as before based on the Sculptor model, the radial size paramters from $r_{\rm king} = 0.1$ to 5 kpc while setting the limiting radius to $r_{\rm lim} = 5.3\,r_{\rm king}$. The actual King radius is $\approx 0.3\,\mathrm{kpc}$. The total luminosity and the stellar mass-to-light ratio are kept constant. Fig. 3.4 shows the resulting $M_{\rm dyn}/L$ ratios.

If the King radius is large (in this particular model $\approx$ 0.5–1 kpc), the system has a low density, therefore low internal accelerations $g_{\rm N}$, and the internal dynamics are dominated by the external field. In this case, the total effective mass profile follows the baryonic mass profile and $M_{\rm dyn}/L$ is independent of the exact radial density model.

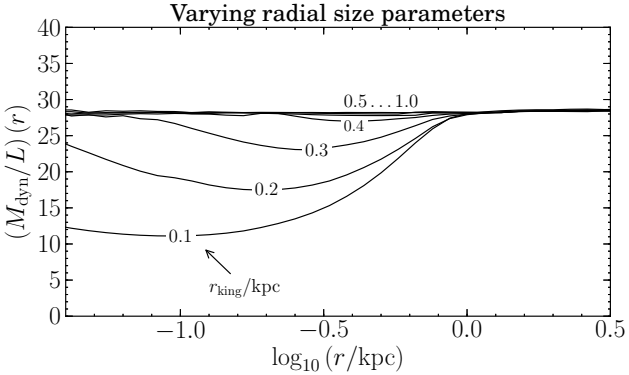

Figure 3.4: The ratio of the predicted effective dynamical mass to baryonic matter is plotted as a function of radius. The presented models are based on Sculptor ($M/L = 3\,\mathrm{M}_\odot/\mathrm{L}_\odot$, $D = 87\,\mathrm{kpc}$), the radial model paramters (King radius and limiting radius) are variied. The King radius, $r_{\rm king}$, is located at the local minimum of $M_{\rm dyn}/L$. See also the description in Section 3.4.4.

If however the baryonic matter density becomes compact/dense enough such that the internal accelerations, $g_{\rm N,int}$, become large enough to leave the external field-dominated regime (here $r_{\rm king} < 0.5\,\mathrm{kpc}$), the density model becomes important and sensitively affects the dynamical mass-to-light ratio at $r \ll r_{\rm lim}$.

3.5 Results

Figs 3.5–3.9 present the results for the considered dSph satellite galaxies. The top panels show the cumulative mass profiles of the baryonic matter (dashed lines) and the resulting effective dynamical mass (i.e. mass of baryonic matter + PDM, solid lines). The bottom panels show the dynamical mass-to-light ratio as function of the distance r to the respective satellite galaxy's centre. The black lines represent models at the most likely distance, D (see Table 3.2). Purple lines show models at the maximum distance to the Sun, $D_{\rm max}$, orange lines those at the minimum distance, $D_{\rm min}$. All lines are marked with their model-specific values of M_*/L in units of $\mathrm{M}_\odot/\mathrm{L}_\odot$.

3.5.1 Fornax

Due to its large distance to the Galactic Centre and its large total luminosity (i.e. mass), Fornax (see Fig. 3.5) is effectively isolated and unaffected by the EFE. The resulting dynamical mass-to-light ratio, which is presented in the lower panel of Fig. 3.5, depends on the radius, r, and ranges between 10 and $50\,\mathrm{M}_\odot/\mathrm{L}_\odot$ depending on the model. Contrary to the external field-dominated dSphs, the accuracy of the model has a strong influence on the resulting $M_{\rm dyn}/L$ as a function of radius.

Because this dSph is effectively isolated and has a cored baryonc matter density distribution, the central shape of the PDM profile has a power-law slope of $\alpha = \mathrm{d}\log\rho_{\rm ph}(r)/\mathrm{d}\log r|_{r\to 0} \approx -0.5$. This is consistent with the inference[9] by Walker and Peñarrubia (2011), who find $\alpha = -0.39^{+0.43}_{-0.37}$. Although

[9] Walker and Peñarrubia (2011) derive the quantity $\Gamma = \alpha + 3$.

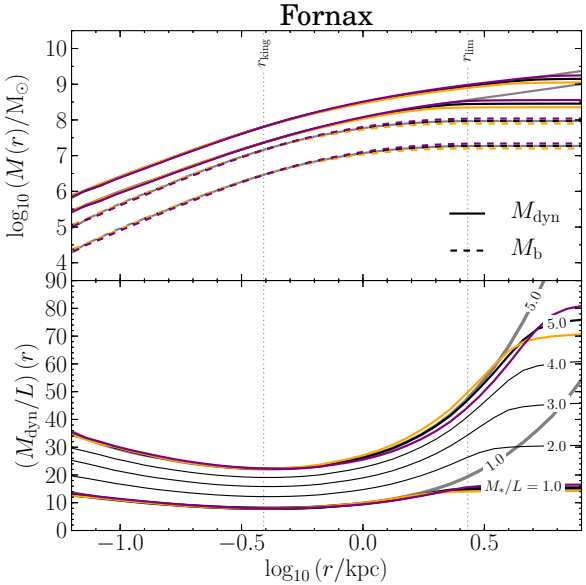

Figure 3.5: Results for Fornax. Top panel: cumulative profiles of the assumed baryonic mass (dashed line) and the predicted effective dynamical mass (solid line) as a function of distance from Fornax's centre. The corresponding mass model paramters are detailed in Table 3.1. The lower dashed lines belong to the $M_*/L = 1\,\mathrm{M}_\odot/\mathrm{L}_\odot$ model, the upper dashed lines to the $M_*/L = 5\,\mathrm{M}_\odot/\mathrm{L}_\odot$ one. Bottom panel: the ratio of effective dynamical mass (baryonic matter + PDM) to baryonic mass with radius r are plotted for each Fornax model. The results are discussed in Section 3.5.1. Colour coding: the black lines correspond to models at their most likely ("normal") distances (D, see Table 3.2). Purple lines represent the models at the maximum distances to the Sun, $D_{\rm max}$, and orange lines at $D_{\rm min}$, respectively. Grey lines show the models in isolation, i.e. without external field. All lines are marked with the individual values of M_*/L in units of $\mathrm{M}_\odot/\mathrm{L}_\odot$. The values of $r_{\rm king}$ and $r_{\rm lim}$ are given for the normal distances, D.

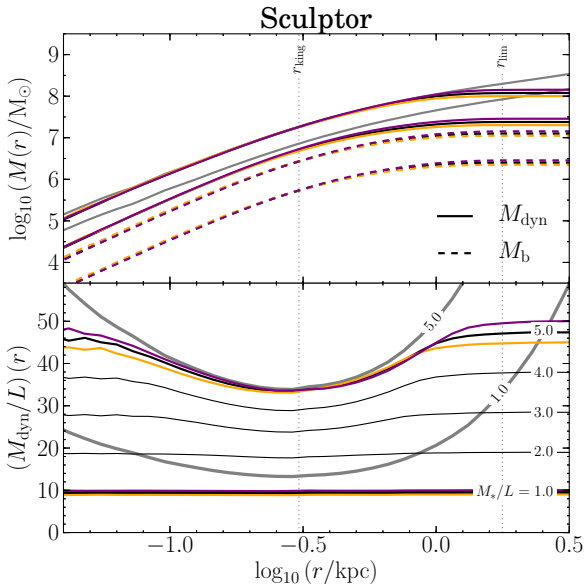

Figure 3.6: Results for Sculptor. See the caption of Fig. 3.5 for an explanation. The results for this object are discussed in Section 3.5.2.

the external field has almost no influence on Fornax' internal dynamics, it truncates the PDM halo at $r \gtrsim r_{\rm lim}$.

Values of $M_{\rm dyn}/L$ found in the literature are remarkably small compared to those of other dSphs. Their observational errors cover a range from $6.1\,\mathrm{M}_\odot/\mathrm{L}_\odot$ to only $20.4\,\mathrm{M}_\odot/\mathrm{L}_\odot$. These values agree well with our results if $M_*/L \approx 1\,\mathrm{M}_\odot/\mathrm{L}_\odot$.

3.5.2 Sculptor

Sculptor's dynamics is on the verge to being in the external field-dominated regime. It is external field-dominated if $M_*/L = 1\,\mathrm{M}_\odot/\mathrm{L}_\odot$, but it is clearly not if $M_*/L = 5\,\mathrm{M}_\odot/\mathrm{L}_\odot$ (see Fig. 3.6, and also the discussion of model parameters in Section 3.4 based on Sculptor). Fig. 3.6 illustrates that $M_{\rm dyn}/L \approx 9.5\,M_*/L$ if $M_*/L \lesssim 2$. For larger stellar mass-to-light ratios, $M_*/L > 2$, we find that the EF becomes less dominant and the dynamical mass-to-light ratio becomes radius-dependant, most prominently at the core radius $r_{\rm king}$.

In general, the relation $M_{\rm dyn}/L \approx 9.5\,M_*/L$ therefore holds true only at the limiting radius, $r_{\rm lim}$. In contrast to fully EFE-dominated galaxies, the results for Sculptor are sensitive not only to M_*/L and $g_{\rm N,ext}$, but also to the exact density model and total luminosity. One has to be careful with radial dependences. The central density profile of the PDM halo is cored or very close to be cored (i.e. $\alpha \approx 0$, depending on the exact model). This slope is well consistent with the inference by Walker and Peñarrubia (2011), who find $\alpha = -0.05^{+0.51}_{-0.39}$.

The Sculptor results agree very well with the values found in the literature if $M_*/L \approx 4\,\mathrm{M}_\odot/\mathrm{L}_\odot$.

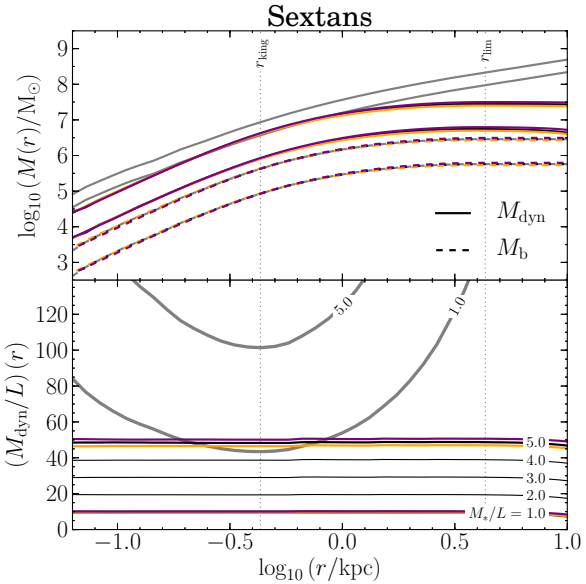

Figure 3.7: Results for Sextans. See the caption of Fig. 3.5 for an explanation. The results for this object are discussed in Section 3.5.3.

Notably, the literature values show the expected trend that the dynamical mass-to-light ratio is similar at small radii (0.1 kpc) and large ($r_{\rm max}$) radii, and lower in between (even though this is only a trend given the large observational errors).

3.5.3 Sextans

Sextans' distance to the Galactic Centre is not much larger than that of Scuptor, but in comparison it is much fainter (by a factor of $\approx 1/5$), bringing it into the external field-dominated regime: The effective dynamical mass follows the baryonic mass and

$$M_{\rm dyn}/L \approx 9.7\, M_*/L \quad \text{[for Sextans]}.$$

The choice of the exact density model and the exact total luminosity are of minor importance (within certain limits of course), and the stellar mass-to-light ratio as well as the strength of the external field are entirely determining the resulting effective dynamical mass-to-light ratio. Also Sextans' PDM density profile is clearly cored.

The dynamical mass-to-light ratios we derived for Sextans under the assumptions of Milgromian dynamics to describe gravity correctly are far below the values found by Walker et al. (2007) and Strigari et al. (2008), whose errors cover the wide range from 108 to 373 $\mathrm{M}_\odot/\mathrm{L}_\odot$. These values are even far above the computed upper Milgromian limit (if the satellite is assumed to be isolated).

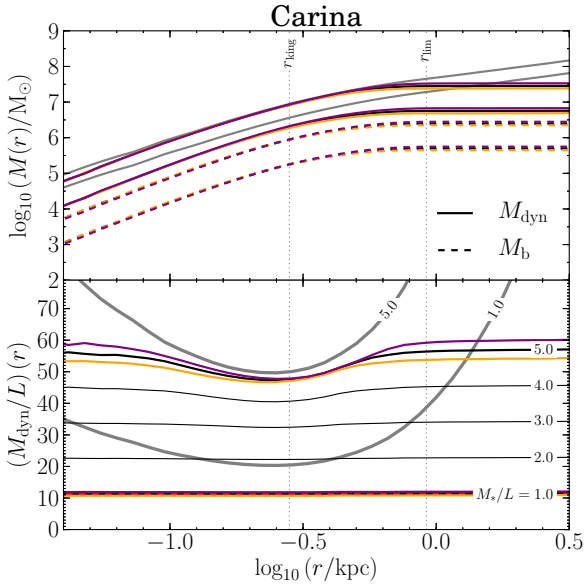

Figure 3.8: Results for Carina. See the caption of Fig. 3.5 for an explanation. The results for this object are discussed in Section 3.5.4.

3.5.4 Carina

Although Carina is clearly more distanced from the Galactic Centre than Sculptor, the effect of the external field on the internal dynamics appears very similar, because in both galaxies the ratio of $g_{\rm N,int}$ to $g_{\rm N,ext}$ is similar. Also Carina appears clearly external field-dominated if $M_*/L = 1\,\mathrm{M}_\odot/\mathrm{L}_\odot$, but partly overcomes this effect if the actual M_*/L is high (e.g. $5\,\mathrm{M}_\odot/\mathrm{L}_\odot$, as shown in Fig. 3.8). The average dynamical mass-to-light ratio is relatively high compared to the other dSphs, it is $\approx 11.2\,M_*/L$ if $M_*/L \lesssim 2.5\,\mathrm{M}_\odot/\mathrm{L}_\odot$. The central shape of Carina's PDM halo is cored or *very* close to be cored (closer than in the case of Sculptor), as can be seen in the bottom panel of Fig. 3.8: $\mathrm{d}(M_{\rm dyn}/L)/\mathrm{d}r|_{r\to 0} \approx 0$.

In the literature, we again find much larger values for $M_{\rm dyn}/L$. These cover the range from $336\,\mathrm{M}_\odot/\mathrm{L}_\odot$ in the central region to $81\,\mathrm{M}_\odot/\mathrm{L}_\odot$ in the outer region. The inferred values therefore indicate a cuspy DM profile, whereas we expect the PDM profile to be cored in theory. However, given the large scatter of these values which are inferred from observations, one should use them with much care, because the dynamical mass is estimated from the velocity dispersion, and large velocity dispersions can have various origins. Altogether, our determined values for $M_{\rm dyn}/L$ are however a bit too low compared to those inferred from observations (Angus et al., 2014).

3.5.5 Draco

Draco is the faintest of the classical satellites, and it is located at a small Galactic distance and is thus strongly influenced by the gravitational potential of the MW. As a consequence, its internal dynamics are dictated by this external field, and the dynamical mass-to-light ratio (see Fig. 3.9) is thus radius

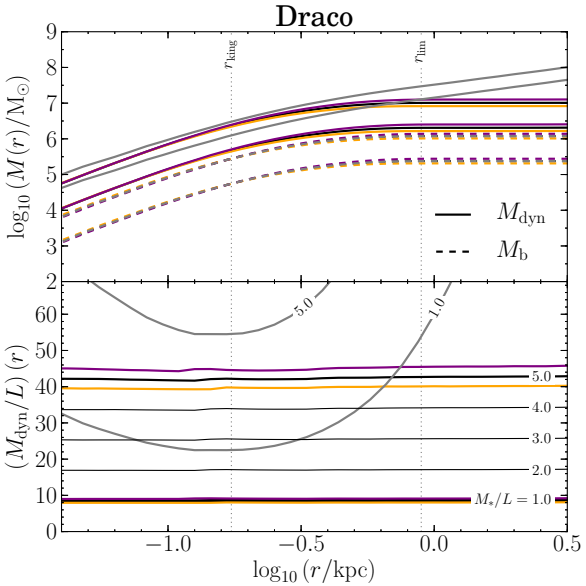

Figure 3.9: Results for Draco. See the caption of Fig. 3.5 for an explanation. The results for this object are discussed in Section 3.5.5

independent: $\rho_{\rm dyn}(r) \propto \rho_{\rm b}(r)$, and $M_{\rm dyn}/M_* \approx 8.5$. Thus

$$M_{\rm dyn}/L \approx 8.5\, M_*/L \quad \text{[for Draco]}.$$

The central shape of the PDM halo is thus cored, because the baryonic density profile is cored. Furthermore, the predicted $M_{\rm dyn}/L$ are neither sensitive to the exact density model (see Section 3.4.4) nor to the observational uncertainty of Draco's total luminosity (see Section 3.4.3). What matters are the stellar mass-to-light ratio and the strength of the external field.

The dynamical mass-to-light ratios we found for Draco are very small compared to those available in the literature (cf. Table 3.3). For example, Strigari et al. (2008) find $M_{\rm dyn}/L_{\rm V} = 55^{+122}_{-12}\,\mathrm{M}_\odot/\mathrm{L}_\odot$ within $r = 0.1\,\mathrm{kpc}$, and $137^{+15}_{-21}\,\mathrm{M}_\odot/\mathrm{L}_\odot$ within $r = 0.3\,\mathrm{kpc}$.[10] Walker et al. (2007) find $346\,\mathrm{M}_\odot/\mathrm{L}_\odot$ within $r = r_{\rm max}$.[11] While the first value agrees fairly with our findings, the overall conclusion is that our results are in contradiction with either the values of $M_{\rm dyn}/L$ from velocity dispersion measurements (which could be contaminated by binaries and outliers) or with the assumption that Draco is in dynamical equilibrium, or both.

[10] These values for the dynamical mass-to-visible light ratios are deduced from the density models and luminosities given by Strigari et al. (2008), see their table 1.

[11] We combine the dynamical mass measured by Walker et al. (2007) with the stellar luminosity given by Strigari et al. (2008). The results are compiled in Table 3.3.

	$M_{0.1}/L_{V,0.1}$		$M_{0.3}/L_{V,0.3}$		$M_{r_{\max}}/L_{V\mathrm{tot}}$		
	predicted with EFE	observ. inferred	predicted with EFE	observ. inferred	predicted with EFE	predicted without EFE	observ. inferred
Fornax	[10.9, 29.9]	$12.9^{+7.5}_{-4.3}$	[8.1, 22.8]	$6.8^{+0.5}_{-0.7}$	[14.3, 47.9]	[21.2, 51.6]	12
Sculptor	[8.9, 40.5]	40^{+74}_{-26}	[8.9, 33.7]	23^{+2}_{-7}	[8.9, 50.1]	[33.3, 78.7]	38
Sextans	[9.5, 50.3]	280^{+93}_{-47}	[9.5, 50.3]	143^{+113}_{-35}	[9.5, 50.3]	[163.8, 370.6]	108
Carina	[10.7, 54.5]	293^{+43}_{-37}	[10.7, 48.0]	81^{+10}_{-5}	[10.7, 59.4]	[38.6, 90.5]	81
Draco	[8.0, 44.7]	55^{+122}_{-12}	[8.0, 44.7]	137^{+15}_{-21}	[8.0, 44.7]	[53.8, 125]	346

Table 3.3: A compilation of dynamical mass-to-light ratios from the literature is listed (in units of $\mathrm{M}_\odot/\mathrm{L}_\odot$) side by side with the predictions made in this paper applying Milgromian dynamics. $M_{0.1}$ and $M_{0.3}$ are the total dynamical masses within 0.1 and 0.3 kpc from the dSph's centre, as found by Strigari et al. (2008) from velocity dispersion measurements when applying Newtonian dynamics. These masses are divided by the respective luminosities, $L_{\mathrm{V},0.1}$ and $L_{\mathrm{V},0.3}$, provided by the same authors. $M_{r_{\max}}$ is the total dynamical mass within the limiting radius as provided by Walker et al. (2007) (see Table 3.1). The total V-band luminosity, $L_{V,\mathrm{tot}}$, is again adopted from Strigari et al. (2008).

3.6 Summary and conclusions

The problem of the nature and dynamics of the dwarf spheroidal satellite galaxies is a vivid one. As highlighted in numerous recent studies, their phase-space distribution around the MW and the Andromeda galaxy is not compatible with them being primordial galaxies embedded in CDM haloes (e.g., Ibata et al., 2014; Pawlowski et al., 2014). On the contrary, if they are of tidal origin, they can contain only little or no DM. In this case, the observed high velocity dispersions conclude either that *all* these objects must be out of equilibrium, or that Newtonian dynamics fails on this scale and that a different theory of gravity must apply (e.g., Milgromian dynamics). In spiral galaxies, the correlation between the mass discrepancy and the gravitational acceleration has long been known to hold for orders of magnitude in mass, and can be interpreted as evidence for Milgromian dynamics. Such dynamics naturally predicts that the MW and Andromeda must have had a close tidal encounter, likely 7–11 Gyr ago (Zhao et al., 2013), leading to the formation of at least a significant fraction of today's satellites of the Local Group galaxies. Recent predictions of internal velocity dispersions of Andromeda's satellites within Milgromian dynamics have proven very successful (McGaugh and Milgrom, 2013a,b). For the MW dwarfs, the situation is less clear. It has long been known that ultra-faint dwarfs cannot be accounted for in Milgromian dynamics if they are in dynamical equilibrium (McGaugh and Wolf, 2010): these objects are close to fully filling their Milgromian tidal radii, and therefore are likely out of equilibrium. For classical dwarfs, we revisited the dynamics here (apart from UMi which also appears out of equilibrium), by taking advantage of the AMR Poisson solver to solve for the MW and the dwarf satellites simultaneously. We produced a table of predicted dynamical mass-to-light ratios which can be useful for observers (Table 3.3).

We find typical M_{dyn}/L of ≈ 8 to $50\,\mathrm{M}_\odot/\mathrm{L}_\odot$ (depending on model parameters, particularly the stellar mass-to-light ratio). In the case of Sculptor and Fornax, these values agree well with observations. In the case of Draco, Sextans, and Carina, these values are low compared to todays observational findings. This is in accordance with what Angus (2008) had found, and it can mean that

1. the satellites are not in virial equilibrium due to the MW tidal and external field,

2. past observational findings are incorrect due to outliers and binary contamination, or

3. that the specific modified gravity theory used[12] is not the theory that describes the EFE correctly. For the latter case, we provide for each satellite upper limits of $M_{\rm dyn}/L$ possible in Milgromian dynamics, in case the external field turns out to be negligible.

It has already been argued in the past that the EFE might be an observational problem of Milgromian dynamics as formulated here, when confronting predictions to data (Scarpa, 2006; Hernandez et al., 2010; Hernandez and Jiménez, 2012; Hernandez et al., 2012, 2013). The argument is that, often, when the EFE starts playing a role, the agreement of Milgromian dynamics with observational data becomes marginal, while it remains good if the EFE is neglected: this might indeed be true for the dwarf spheroidals of the MW considered here. However, it is not necessarily the case in general. For instance, the escape speed from the MW can be determined from the EFE and agrees well with observations (Famaey et al., 2007), and nearby open clusters having internal accelerations below a_0 do not exhibit large mass discrepancies. Also, in the CDM context, some dwarfs close to M31 have been pointed out as outliers because of their low velocity dispersions, while with Milgromian dynamics, such small velocity dispersions are naturally predicted (McGaugh and Milgrom, 2013b): this prediction relies on the EFE being non-negligible as in this paper. Nevertheless, we should point out that, even though the EFE is a necessary consequence of Milgromian dynamics, in some implementations of the theory, it could be negligible in practice: this can be the case for instance in time-nonlocal modified inertia theories (Milgrom, 2011). Computations of, e.g., the escape speed from the MW would in this case become more complicated and many concepts such as the escape speed could have to be fully redefined. In view of the current inferences of dynamical masses of the MW dwarfs, this absence of EFE should certainly be kept as a possibility, as advocated in Scarpa (2006); Hernandez et al. (2010, 2012, 2013); Hernandez and Jiménez (2012).

Kroupa (1997) has shown that it is possible to achieve high $M_{\rm dyn}/L \approx 100$ even in DM-free dSphs by assuming purely classical Newtonian dynamics. The reason is that the satellites that were set up with spherical phase-space distribution functions evolve away from this state by losing particles from outer regions of phase-space due to the Galactic tides. The assumption made by the observer who assumes spherically symmetric equilibrium structures is then wrong, leading to very high apparent $M_{\rm dyn}/L$ values, despite the models not having any DM. This finding also applies to Milgromian dynamics (and of course also to PDGs embedded in CDM haloes), although we expect that the effect is less strong (Hernandez and Jiménez, 2012).

That observational findings of the measured dynamical mass are not as correct as we think today is also one possibility which should not be excluded a priori. Dynamical masses are derived from the velocity dispersion, which is usually based on measurements that are very sensitive to effects that have not been taken into account yet, e.g. the number of binary stars, or plain outliers from the background. Serra et al. (2010) have for instance shown that taking into account outliers was bringing Sextans back on the Milgromian prediction. A similar expectation can be made for Draco and Carina. Interestingly, it has recently been shown that the tidal effects are not significantly changing the predictions for Carina (Angus et al., 2014).

We note that the predictions of Milgromian dynamics are most accurate for the most luminous satellites, and least for the less luminous ones. The most luminous dwarf galaxies likely have had the highest star formation rates (SFRs) in the past. High SFRs result in high minimum embedded star cluster masses, making the embedded clusters denser and thus destroying binaries more efficiently (Marks and Kroupa, 2011). It is therefore likely that the velocity dispersion measurements of the less luminous dwarfs are more affected by unresolved binaries than those of the most massive dwarfs. If one finds that the dynamical masses computed here (which are predictions of Milgromian dynamics based on

[12] Note also that we implemented here only one particular ν-function

static equilibrium models, and taking into account the EFE) are compatible with future, more precise measurements of the velocity dispersions in these dwarf galaxies, this would strengthen the notion that the MW dSph satellite galaxies are TDGs that have been formed $7 - 11$ Gyr ago as a consequence of a close encounter between M31 and the MW. In this case, N-body computations based on Milgromian dynamics of the MW–M31 encounter should further test this tidal scenario.

If it however turns out that all measured velocity dispersions are correct and that the considered dwarf galaxies *are* in virial equilibrium, then the computed dynamical masses based on Milgromian dynamics tell us that the specific implementation used here can be excluded, and one has to consider other theories, such as modified inertia theories in which the EFE can be practically negligible (Milgrom, 2011).

CHAPTER 4

Phantom of RAMSES (POR): A new Milgromian dynamics N-body code

Published in
Canadian Journal of Physics (in press)
June 2014

DOI: 10.1139/cjp-2014-0168

F. Lüghausen, B. Famaey, and P. Kroupa

Abstract

Since its first formulation in 1983, Milgromian dynamics (MOND) has been very successful in predicting the gravitational potential of galaxies from the distribution of baryons alone, including general scaling relations and detailed rotation curves of large statistical samples of individual galaxies covering a large range of masses and sizes. Most predictions however rely on static models, and only a handful of N-body codes have been developed over the years to investigate the consequences of the Milgromian framework for the dynamics of complex evolving dynamical systems. In this work, we present a new Milgromian N-body code, which is a customized version of the Ramses code (Teyssier 2002) and thus comes with all its features: it includes particles and gas dynamics, and importantly allows for high spatial resolution of complex systems due to the adaptive mesh refinement (AMR) technique. It further allows the direct comparison between Milgromian simulations and standard Newtonian simulations with dark matter particles. We provide basic tests of this customized code and demonstrate its performance by presenting N-body computations of dark-matter-free spherical equilibrium models as well as dark-matter-free disk galaxies in Milgromian dynamics.

4.1 Introduction

The large-scale structure of the Universe reveals a dark sector generally supposed to be made of dark energy (e.g. Komatsu et al., 2011; Planck Collab., 2013b) and hitherto undetected missing matter or dark matter (DM), the physical nature of both still being unexplained to date. In the current standard model of cosmology, DM is assumed to be made of non-baryonic particles, the so-called 'cold dark matter' (CDM). Whilst successful on large scales, this interpretation leads to a long list of problems on the scales of galaxies and the Local Group (Kroupa et al., 2010, 2012; Ibata et al., 2013, 2014; Pawlowski et al., 2014; Bournaud et al., 2007; Gentile et al., 2007). One of the biggest challenges for the DM-based model may be the tight scaling relations which galaxies follow (Famaey and McGaugh, 2012), the tightness of which cannot be unterstood in the DM context. These relations can all be well summarized by Milgrom's formula, devised more than 30 years ago (Milgrom, 1983),

$$g = (g_{\rm N} a_0)^{1/2} \ \text{for}\, g \ll a_0 \simeq 10^{-10}\text{ms}^{-2}\,. \tag{4.1}$$

This is equivalent to stating that, for $g \ll a_0$, (i) the dynamics becomes scale-invariant under space-time transformations $(t, \boldsymbol{x}) \rightarrow (\lambda t, \lambda \boldsymbol{x})$ with $\lambda \in \mathbb{R}$ (Milgrom, 2009d), or (ii) gravity is anti-screened with a 'gravitational permittivity' equal to $g/a0$ in some gravitationally polarizable medium (Blanchet and Bernard, 2014). On cosmological scales the formula does not work, meaning that Milgromian dynamics is only an effective description of dynamics on galaxy scales, and is probably part of a yet incomplete paradigm. But on galaxy scales, the formula is extremely succesful: not only were galaxy scaling relations correctly predicted by this formula (e.g., the baryonic Tully-Fisher relation, McGaugh, 2005b, 2011b), some were actually found because they were pointed to by the formula (e.g., the mass discrepancy-acceleration relation, Sanders, 1990; Scarpa, 2006; McGaugh, 2012). So, independently of its deepest physical meaning, Milgrom's formula already achieved one of the most important roles of a theoretical idea, i.e. to direct posterior experiments or observations, and correctly predict their outcome. For a complete and up-to-date review of Milgromian dynamics, see Famaey and McGaugh (2012).

However, applying Eq. 4.1 into a N-body code would lead to dramatically unphysical predictions. It can readily be seen that, in a two-body configuration, the force is not symmetric (Milgrom, 1983). This means that Newton's third law (the action and reaction principle) does not hold in this framework, and as a consequence the momentum is not conserved. Instead of Eq. 4.1, one thus has to use a non-linear generalization of Poisson's equation leading precisely to Eq. 4.1 in one-dimensional-symmetric configurations such as spherical symmetry. Two such classical modifications of the Poisson equation have been proposed (Bekenstein and Milgrom, 1984; Milgrom, 2010), and have subsequently been shown to be natural weak-field limits of relativistic modified gravity theories (Bekenstein, 2004; Milgrom, 2009a). Because these modified Poisson equations all necessarily involve at least one non-linear step, the total force on each particle cannot be obtained by summing the individual forces from all the other particles as in Newtonian gravity. This means that one must rely on particle-mesh techniques to develop Milgromian N-body codes.

Only a handful of such Milgromian codes have been developed over the years. This field was pioneered by Brada and Milgrom (1999), who studied the stability of galaxy disks, the formation of warps and the dynamics of satellite galaxies orbiting a host (gas dynamics was not considered). More recent codes, like N-MODY (Londrillo and Nipoti, 2009), solve the Milgromian Poisson equation in spherical coordinates and are therefore predestinated for close to spherically symmetric problems, but do not allow generic simulations of flattened and multicentered stellar systems on galactic and sub-galactic scales. Other codes are rather designed only for cosmological simulations (Llinares et al., 2008). The most precise N-body computations for disk galaxies have been made by Tiret and Combes (2007, 2008), but

only with rudimentary treatment of hydrodynamics and very low resolution. The most recent code has been developed by Angus et al. (2012, 2014), based for the first time on the modified Poisson equation of Milgrom (2010).

To date, with so few codes and simulations at hand, only very little is actually known about the time-evolution of dynamical objects within Milgromian dynamics. Generic, fully dynamical tests using N-body codes with live particles and a full treatment of hydrodynamics are still missing. Testing Milgromian dynamics in dynamical N-body systems is however fundamental, because the implications of Milgrom's force law on the time-evolution of dynamical systems are not trivial, and analytic approaches with static realizations of galactic potentials are not sufficient to understand those implications. Even though the Milgromian force law mimics the potential of an effective DM halo, the physical properties of this effective DM halo are very different from those of the classical, pressure-supported DM halos, because it is, contrary to CDM halos, directly connected to the distribution of baryonic matter,[1] and is affected by non-trivial phenomena such as the so-called external field effect. What is more, this effective halo does not lead to any kind of dynamical friction.

Therefore, it is still unclear whether the Milgromian framework can successfully explain all dynamical probes of the gravitational potential on galactic scales, such as the geometry of tidal streams or even a vast topic like the formation of galaxies in general. Here we present a new Milgromian dynamics N-body code, which is a customized version of the Ramses code (Teyssier, 2002) based on the modified Poisson equation of Milgrom (2010). It comes with all its features, including adaptative mesh refinement, particle and gas dynamics, and it is suited for various different contexts such as the simulations of isolated systems, interacting systems, as well as the formation of structures in a cosmological context.

4.2 Milgromian dynamics and QUMOND

Since its first formulation in 1983 (Milgrom, 1983), many relativistic and non-relativistic Milgromian gravity theories have been developed, yielding the scale-invariant property of Milgrom's empirical formula (Eq. 4.1) in the weak-field limit and in spherical symmetry. One such theory is the so called quasi-linear formulation of MOND (QUMOND; Milgrom, 2010), having the following Poisson equation:

$$\nabla^2\Phi(\boldsymbol{x}) = 4\pi G\rho_\mathrm{b}(\boldsymbol{x}) + \nabla\cdot\left[\nu\left(|\nabla\phi|/a_0\right)\nabla\phi(\boldsymbol{x})\right] \tag{4.2}$$

or

$$\nabla^2\Phi(\boldsymbol{x}) = 4\pi G\left(\rho_\mathrm{b}(\boldsymbol{x}) + \rho_\mathrm{ph}(\boldsymbol{x})\right) . \tag{4.3}$$

In this equation, $\rho_\mathrm{b}(\boldsymbol{x})$ is the baryonic density, and $\phi(\boldsymbol{x})$ the Newtonian potential such that $\nabla^2\phi(\boldsymbol{x}) = 4\pi G\rho_\mathrm{b}(\boldsymbol{x})$. The function $\nu(y)$ is defined by the limits $\nu(y) \to 0$ if $y \gg 1$ (Newtonian regime) and $\nu(y) \to y^{-1/2}$ if $y \ll 1$ (Milgromian regime). We write the second term on the right hand side of Eq. 4.2 as

$$\rho_\mathrm{ph}(\boldsymbol{x}) = \frac{\nabla\cdot\left[\nu\left(|\nabla\phi(\boldsymbol{x})|/a_0\right)\nabla\phi(\boldsymbol{x})\right]}{4\pi G} \tag{4.4}$$

in order to emphasize the quasi-linearity of this Poisson equation. It tells us that the Milgromian gravitational potential, Φ, is defined by the baryonic matter density distribution, ρ_b, plus one additional term, noted as ρ_ph, which also has the unit of matter density and which is defined by the Newtonian potential, ϕ, i.e. by the distribution of baryonic matter through Eq. 4.4. In other words, the total gravitational potential, $\Phi = \phi + \Phi_\mathrm{ph}$, can be divided into two parts: a classical (Newtonian) part, ϕ, and an additional Milgromian part, Φ_ph.

[1] This applies particularly to the formation of structure and substructure (e.g. the instability of rotating disk as in Sect. 4.5).

The additional matter density distribution, $\rho_{\rm ph}(\boldsymbol{x})$, that would, in Newtonian gravity, yield the additional potential $\Phi_{\rm ph}(\boldsymbol{x})$, and therefore obeys $\nabla^2\Phi_{\rm ph}(\boldsymbol{x}) = 4\pi G\rho_{\rm ph}(\boldsymbol{x})$, is known as the 'phantom dark matter' (PDM) density (Eq. 4.4). This PDM is not real matter but a mathematical ansatz that allows to compute the additional gravitational potential predicted by the Milgromian framework. Furthermore, it gives it an analogue in Newtonian dynamics and allows a convenient comparison of the predictions of Milgromian dynamics to those of the CDM-based standard model: the mathematical PDM density is exactly the density that would be interpreted as unseen or dark matter in the context of the standard model of cosmology.

In the following Sect 4.3.1, we explain in three simple steps how Eq. 4.2 can be solved in general. In Sect. 4.3.2, we exhibit a numerical scheme that allows to evaluate Eq. 4.4 on a diskrete grid.

4.3 The 'Phantom of RAMSES' (POR) code

The goal of any N-body code is the computation of the force acting on the individual particles in order to integrate these particles through phase-space. In the simplest case, that is a system made of N particles with known masses, positions and velocities, $N(N-1)$ forces have to be evaluated (if no simplifications are made). With modern computer technology, this is feasable for systems with $N \lesssim 10^6$, but computationally too expensive for systems with $N \gtrsim 10^6$. However, in collisionless systems, i.e. systems which have relaxation time-scales longer than one Hubble time (this is by definition the case for galaxies), the potential is smooth and direct N-body forces can be neglected. This allows us to make a variety of simplifications to compute the accelerations for a large number of particles. For instance tree-codes use a hierarchical spatial tree to define localized groups of particles whose contribution to the local gravitational field is calculated all at once. However, due to the non-linearity of Milgromian dynamics, this type of technique is in principle difficult to apply here. So the general approach used here is to map the particles (positions and masses) on a diskrete grid in order to determine the smoothed matter density distribution $\rho_{\rm b}(\boldsymbol{x})$ of the particles. From that, the gravitational potential $\phi(\boldsymbol{x})$ is derived by solving the Poisson equation,

$$\nabla^2\phi(\boldsymbol{x}) = 4\pi G\rho_{\rm b}(\boldsymbol{x})\,. \tag{4.5}$$

From this grid-based potential, the acceleration $\boldsymbol{a}(\boldsymbol{x}) = -\nabla\phi(\boldsymbol{x})$ can be computed. The acceleration is then interpolated at the positions of the individual particles, and the equations of motion for each particle are integrated. These integrals can be approximated numerically in various ways.

The POR code is a customization of the Ramses code (Teyssier, 2002) and therefore comes with all its features. Ramses implements an adaptive mesh refinement (AMR) strategy (Kravtsov et al., 1997). Starting with a coarse Cartesian grid, the grid is recursively refined on a cell-by-cell and level-by-level basis. If a cell fulfills certain refinement-criteria, e.g. exceeds a minimum particle number density, the cell is split up into 2^3 sub-cells. This technique allows to use large simulation boxes and still to achieve high spatial resolution in the regions of interest. This makes the code particularly interesting not only for cosmological simulations, but also for e.g. galaxy-galaxy interactions, satellite galaxies in the field of a host galaxy, and more. The Poisson equation is solved using a multi-grid relaxation scheme (Kravtsov et al., 1997; Guillet and Teyssier, 2011): the residual $\nabla^2\phi - 4\pi G\rho$ is minimized iteratively using the Gauss-Seidel method. This approach has the advantage of allowing arbitrarily shaped domain boundaries and can therefore save a lot of work overhead. What is more, the convergence rate does not depend on the number of cells. This makes it particularly interesting for runs with a large number of particles/cells. Once the Poisson equation is solved and the gravitational acceleration of each particle is known, a predictor-corrector scheme with adaptive time steps is used to move the particles through phase-space.

To solve Eq. 4.2 on the adaptive grid, the Poisson solver has been patched to implement the procedure described in the following subsection. The user can decide whether the Newtonian or the Milgromian force should be computed and applied by setting a flag in the project's configuration file without the need of recompiling the code. Having a code that can run Newtonian (Ramses) and Milgromian (POR) N-body simulations at the same time is important, because it allows a side-by-side comparison of Newton+DM on one hand and Milgromian dynamics (without DM) on the other hand. We expect from this direct comparison to find qualitative differences between both scenarios leading to observationally testable predictions that can clearly distinguish between both cases.

4.3.1 The modified Poisson solver

Solving the QUMOND Poisson equation (Eq. 4.2) requires solving two linear differential equations and one additional algrebraic step.

1. As before, the classical Poisson equation,

$$\nabla^2\phi(\boldsymbol{x}) = 4\pi G\rho_{\mathrm{b}}(\boldsymbol{x})\,, \tag{4.6}$$

   is solved to compute the Newtonian potential, ϕ, and its gradient, $\nabla\phi$, from the given matter density distribution defined by the particles and the gas. At the coarse grid boundary, the condition $\phi(r) = GM_{\mathrm{b}}/r$ is applied. M_{b} is the total baryonic mass, and r the distance to its center.[2]

2. The PDM density $\rho_{\mathrm{ph}}(\boldsymbol{x})$ (Eq. 4.4) is calculated applying the diskrete scheme which is described in detail in Sect. 4.3.2.

3. Then, the Poisson equation is solved a second time, now with the baryonic matter plus PDM density,

$$\nabla^2\Phi(\boldsymbol{x}) = 4\pi G\left(\rho_{\mathrm{b}}(\boldsymbol{x}) + \rho_{\mathrm{ph}}(\boldsymbol{x})\right)\,, \tag{4.7}$$

   to obtain the Milgromian potential $\Phi(\boldsymbol{x})$. This time, the boundary condition

$$\Phi(r) = (GM_{\mathrm{b}}a_0)^{1/2}\ln(r) \tag{4.8}$$

   is applied (Eq. 20 in Famaey and McGaugh, 2012), with r again being the distance to the center of baryonic mass. This boundary condition holds true if $|\nabla\phi(r)|/a_0 \ll 1$.

This realization of Milgromian dynamics is very efficient from a code-developing point of view, because it allows us to make use of already existing classical Poisson solvers and thus of existing grid-based codes.[3] Nevertheless, a larger number of changes – apart from adding the PDM density routine – had to be made for technical reasons. The code will be made publicly available as a patch of Ramses in the future.

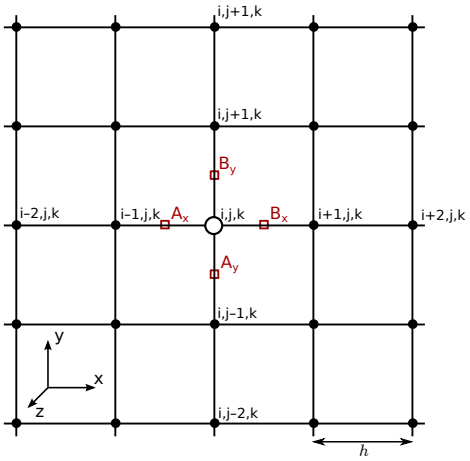

Figure 4.1: Illustration of the discretisation scheme in the x-y plane, referring to Sect. 4.3.2. The grid cells are of equal size with a constant cell with h. The values of $\nu(y)$ are evaluated at the points A and B.

4.3.2 Phantom dark matter density: the diskrete scheme

The PDM density (Eq. 4.4) is approximated at the center of the grid cell (i, j, k) at the position $\boldsymbol{x}_{i,j,k}$ by

$$\begin{aligned}\rho_{\rm ph}^{i,j,k} = \frac{1}{4\pi G h}\Big[& \nu_{\rm B_x}\,(\nabla\phi)_{\rm B_x,x} - \nu_{\rm A_x}\,(\nabla\phi)_{\rm A_x,x} \\ & + \nu_{\rm B_y}\,(\nabla\phi)_{\rm B_y,y} - \nu_{\rm A_y}\,(\nabla\phi)_{\rm A_y,y} \\ & + \nu_{\rm B_z}\,(\nabla\phi)_{\rm B_z,z} - \nu_{\rm A_z}\,(\nabla\phi)_{\rm A_z,z} \Big].\end{aligned} \tag{4.9}$$

See also Lüghausen et al. (2013). Here, ϕ is the classical Newtonian potential computed in the first step, h is the cell width (see Fig. 4.1). $\nu_{\rm A_x}$ is the value of $\nu(|\nabla\phi|/a_0)$ at the point $\rm A_x$. $(\nabla\phi)_{\rm A_x,x}$ is the x-component of $\nabla\phi$ at the point $\rm A_x$ and is approximated by the following finite difference approximation:[4]

$$\begin{aligned}(\nabla\phi)_{\rm A_x,x} &= \frac{\phi^{-2,0,0} - 27\phi^{-1,0,0} + 27\phi^{0,0,0} - \phi^{1,0,0}}{24h} \\ (\nabla\phi)_{\rm A_x,y} &= 0.5\left[(\nabla\phi)_{\rm y}^{-1,0,0} + (\nabla\phi)_{\rm y}^{0,0,0}\right] \\ (\nabla\phi)_{\rm A_x,z} &= 0.5\left[(\nabla\phi)_{\rm z}^{-1,0,0} + (\nabla\phi)_{\rm z}^{0,0,0}\right]\end{aligned} \tag{4.10}$$

[2] The simulation box has to be chosen large enough to fulfill this condition at the coarsest level boundary.
[3] The only limitation is that this scheme can not be implemented into codes which require to linearly add accelerations. This applies to a number of available codes using nested grids (e.g. the SUPERBOX code), and also tree-codes.
[4] We abbreviate $\phi^{i+\Delta i,j+\Delta j,k+\Delta k}$ by $\phi^{\Delta i,\Delta j,\Delta k}$.

with

$$(\nabla\phi)_y^{i,j,k} = \frac{\phi^{0,-2,0} - 8\phi^{0,-1,0} + 8\phi^{0,1,0} - \phi^{0,2,0}}{12h} \qquad (4.11)$$
$$(\nabla\phi)_z^{i,j,k} = \frac{\phi^{0,0,-2} - 8\phi^{0,0,-1} + 8\phi^{0,0,1} - \phi^{0,0,2}}{12h} .$$

This scheme applies to the other points analogously. At the fine levels' grid boundaries, the Newtonian potential ϕ is interpolated from the next coarse grid level.

4.4 Testing

The Ramses code has already been tested extensively (see Teyssier, 2002; Guillet and Teyssier, 2011). Here, we present tests of the POR code to show that the QUMOND extension works correctly and no bugs have been implanted. We start with checking the distribution of PDM to make sure that the QUMOND routine is well implemented. If this test is passed, we proceed to dynamical models that are known to be dynamically stable and check the stability of these in the POR code. We finally compare the results to those obtained by the N-mody code (Londrillo and Nipoti, 2009) using the same initial conditions.

If not stated otherwise, we apply the following ν-function:[5]

$$\nu(y) = \frac{1}{2}\left(1 + \frac{4}{y}\right)^{1/2} - 1 . \qquad (4.12)$$

The code is however not limited to this particular ν-function, the implementation of this formula can be changed readily in POR.

4.4.1 Static tests

The heart and soul of the POR code (and the major change to the original Ramses code) is the routine that computes the PDM density from the Newtonian potential to obtain the Milgromian potential. If we assume the rest of the code to work correctly, as it has done before being customized, it should be sufficient to ensure that the PDM density and subsequently the resulting Milgromian acceleration is computed correctly at every time step. To test this critical routine, we ran the code with models having known analytical solutions. In this paper, we present the results for a single point mass and a Plummer model.

PDM density and acceleration

We set up two spherical models: a) a point-mass with $10^5\,M_\odot$ which is located at the box center. And b) a Plummer model with a total mass of $10^5\,M_\odot$ and a Plummer radius of 10 pc. The Plummer model is populated with 10^5 particles. We execute the code using the following parameters:
- simulation box size: $(100\,\mathrm{kpc})^3$,
- minimum resolution: $100\,\mathrm{kpc}/2^8 = 0.39\,\mathrm{kpc}$,
- maximum resolution: $100\,\mathrm{kpc}/2^{17} = 0.76\,\mathrm{pc}$.

The resolution of the point-mass model is fixed to 0.39 kpc. The grid of the Plummer model is adaptively

[5] This particular ν-function reproduces well the observed gravitational field in galaxies, nevertheless it fails in the Solar System (Hees et al., 2014).

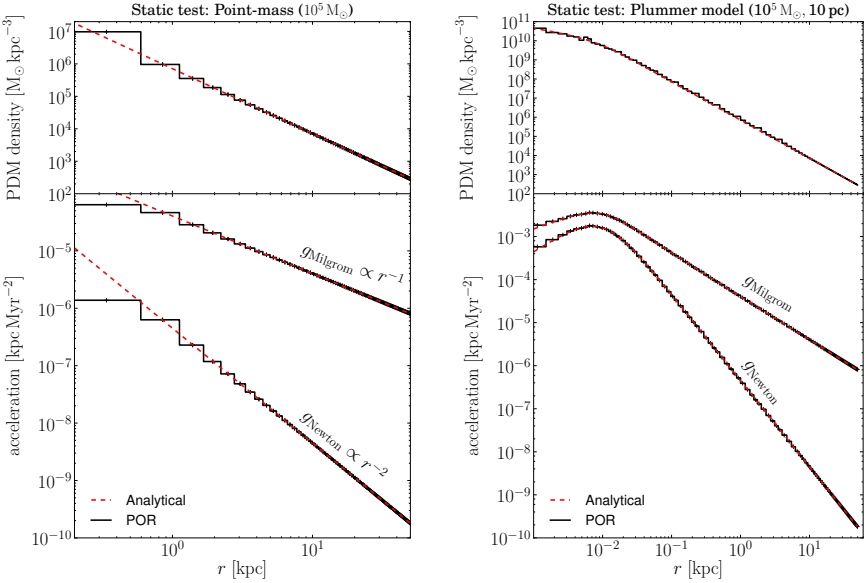

Figure 4.2: The figure shows the PDM density distribution (upper panels) and the Newtonian and Milgromian accelerations (lower panels) computed by the POR code for (a) a point mass (left-hand side) and (b) a Plummer model (right-hand side). The steps (black solid lines) represent the values of individual cells along the diagonal ($x = y = z > 0$). The ticks on the steps mark the cell centers. The red dashed lines are derived analytically. Both models are in the deep Milgromian regime, i.e. $g_N \ll a_0$. The grid resolution of case (a) is fixed to 2^8 cells at a box length of 100 kpc, i.e. 0.39 kpc. The grid resolution of model (b) is variable and ranges from 0.39 kpc (coarsest grid level, i.e. outer regions) to 0.76 pc (finest grid level, i.e. box center), the box size is again $(100\,kpc)^3$.

refined. We plot the resulting PDM density distribution as a function of radius along the diagonal ($x = y = z > 0$) as well as the resulting effective acceleration g in Fig. 4.2. Both, $\rho_{\rm ph}$ and g, agree well with the analytical solution. The PDM density shows little scatter, particularly at the level boundaries (top right panel in Fig. 4.2). This is because the second order of ϕ enters in Eq. 4.4. This scatter is however averaged out in the final acceleration, g. In the case of the point-mass model which has a fixed cell width, one can see that the acceleration $g_{\rm N}$ is smoothed in the innermost cell.[6] As a side effect, the PDM density is slightly off in this cell. In a model made of particles or gas, the smoothing is however negligible if the resolution is sufficient, which is generally the case and can well be seen in Fig. 4.2.

For comparison, also the Newtonian acceleration $g_{\rm N}$ is plotted and compared to its analytical pendant to stress the quality of the resulting Milgromian acceleration g.

Dependence on spatial resolution

The Ramses code works with a so called one-way interface scheme (Kravtsov et al., 1997; Teyssier, 2002). This means it starts solving the Poisson equation at the coarsest level, and uses this coarse level solution of the potential as the boundary condition at the next finer grid level, but not vice versa. I.e., it does not use the solutions of the finer levels to correct the coarse level solution (this would be referred to as a two-way interface scheme). For the POR code, this means that the PDM density distribution on the coarse level alone defines this level's Milgromian potential. A lack of resolution of the PDM density could however result in a non-accurate acceleration on the not so well refined grid level, particularly on the coarse grid level.

However, in Fig. 4.2 one sees no such dependence on the resolution. To quantify this finding, we compare the PDM mass of the coarse grid to the PDM mass of the completely refined grid (i.e. of the leaf cells). In order to get a meaningful result, we only consider the regions that are refined, i.e. are having sub-cells. We find that the difference between the PDM mass of the coarse level cells and the related leaf cells is tiny. For the presented Plummer model, the relative difference is $\approx 4\times10^{-5}$, although the spatial resolution of the finest grid is 32 times as high as the coarse grid resolution.

4.4.2 Dynamical tests

As the PDM density, $\rho_{\rm ph}$, and the resulting Milgromian acceleration, $g = -\nabla\Phi$, have been shown to perform well, we proceed to evolving the Plummer model dynamically. To do so, we set up initial conditions that are, in Milgromian dynamics, in dynamical equilibrium. To find such initial conditions, we use the following distribution function (Eddington's formula; Eddington, 1916).

$$f(E) = \frac{1}{\sqrt{8}\pi^2}\left[\int_0^E \frac{{\rm d}\Phi}{\sqrt{E-\Phi}}\frac{{\rm d}^2\hat{\rho}_{\rm b}}{{\rm d}\Phi^2} + \frac{1}{\sqrt{E}}\left(\frac{{\rm d}\hat{\rho}_{\rm b}}{{\rm d}\Phi}\right)_{\Phi=0}\right] \tag{4.13}$$

with $\hat{\rho}_{\rm b}(r)$ being the normalized density distribution of baryonic matter, $\Phi(r)$ the Milgromian potential energy, and E the kinetical energy. $\Phi(r)$ is computed from the baryonic matter density plus PDM density, $\rho_{\rm b}(r) + \rho_{\rm ph}(r)$, by solving Eq. 4.3 in spherical coordinates. The spherical PDM density distribution,

$$\rho_{\rm ph}(r) = \frac{1}{4\pi G}\frac{1}{r^2}\frac{\rm d}{{\rm d}r}\left(r^2\,\nu(|{\rm d}\phi/{\rm d}r|/a_0)\frac{{\rm d}\phi}{{\rm d}r}\right), \tag{4.14}$$

has been computed numerically for this symmetric model.

[6] The effective resolution of such a grid code is approximately twice the fine level cell width.

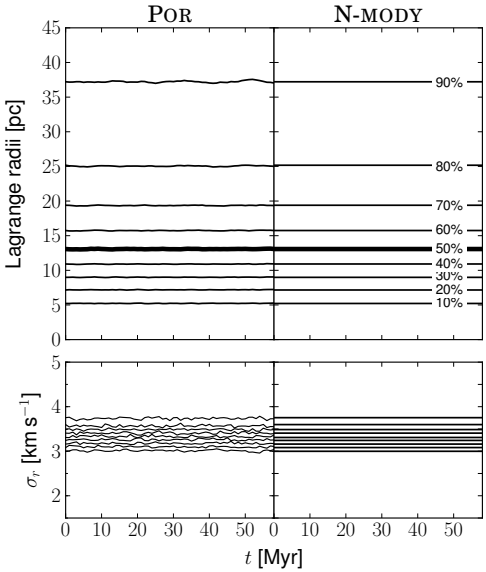

Figure 4.3: The stability of a Plummer model is tested and compared to N-MODY. The Lagrangian radii (10%, 20%, ..., 30%) and radial velocity dispersion (in the radial bins defined by the Lagrangian radii, 0–10%, 10–20%, ..., 80–90%) are plotted vs. time. The Plummer model has a Plummer radius of 10 pc and a total mass of 10^5 $M_\odot$ (deep Milgromian regime). The N-body model is made of 10^5 particles, and exactly the same initial conditions are used for both runs (POR and N-MODY). See Sect. 4.4.2 for details. The plot covers a time range of more than 100 crossing times of this system.

Stability of a spherical model in dynamical equilibrium: Lagrangian radii and radial velocity dispersion

We evolve the Plummer model using the POR code and plot the Lagrangian radii (10%, 20%, ..., 90%) vs. time in Fig. 4.3 (left hand side panels). We find that the Lagrangian radii and consequently the density profile stay constant with time.

Moreover, we compute the radial velocity dispersion within the radial bins defined by the Lagrangian radii (0–10%, 10–20%, ..., 80–90%) and plot them in the bottom left panel of Fig. 4.3. Also the radial velocity dispersions do not change with time, meaning that the test model is shown to be dynamically stable, as expected from theory.

Comparison to the N-MODY code

We execute the N-MODY code using exactly the same initial conditions we used in Sect. 4.4.2. The simple ν-function, $\nu(y) = 0.5(1+4/y)^{1/2}$, is used in the POR code and the related μ-function, $\mu(x) = x/(1+x)$, in N-MODY. We find that the results of both codes are in agreement (see Fig. 4.3, compare the panels on the left hand side to those on the right). The radial velocity dispersion appears to be more stable in N-MODY. This is due to the spherical grid architecture, which is ideally suited for such spherical problems and allows resolving the spherical potential better than the Cartesian cell-based grid in the POR or RAMSES code.

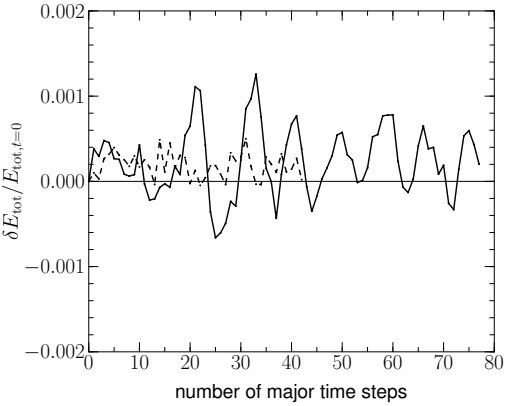

Figure 4.4: The relative energy error is visualized for the Plummer model described in Sect. 4.4. The solid curve shows the relative energy error from the POR code. As a benchmark, we plot this error as the dashed curve also for the Ramses code (using a Plummer model with same size/mass parameters, but with initial velocities yielding virial equilibrium in Newtonian dynamics). One course time step is $\approx$ 1.24 Myr in the Milgromian model and $\approx$ 2.34 Myr in the Newtonian one.

Conservation of energy

Because the QUMOND Poisson equation (Eq. 4.2) is derived from an action with a modified Lagrangian (see Milgrom, 2010, and Sect. 6.1.3 in Famaey and McGaugh, 2012), the related equations of motion obey conservation of energy and angular momentum.

At each time step, we compute the total kinetic energy,

$$T = \sum_{i=1}^{N_{\rm part}} m_i v_i^2, \tag{4.15}$$

of the $N_{\rm part}$ particles having the masses m_i and the velocities v_i. The virial, W, (with units of potential energy) is computed on the grid (leaf) cells,

$$W = -\int_{\mathbb{R}^3} \rho(\boldsymbol{x})\,(\boldsymbol{x}\cdot\nabla\Phi(\boldsymbol{x}))\,d^3x = \sum_{i=1}^{N_{\rm cells}} \rho_i h_i^3\,(\boldsymbol{x}_i\cdot\boldsymbol{g}_i) \tag{4.16}$$

(see Binney and Tremaine, 1987), where ρ_i is the baryonic mass density distribution and Φ_i the Milgromian gravitational potential at the center of the i-th cell (with the cell width h_i). $\boldsymbol{g}_i = -\nabla\Phi_i$ is the acceleration.[7]

We print out the change of total energy, $\delta(T+W)$, with time, the so called numerical 'energy error', at each time step. This energy error always plays a role in numerical experiments, because the complexity of reality forces us to make simplifications to keep the numerical effort at a feasible level, inevitably resulting in such numerical errors. We find that the energy is well conserved within the common toler-

[7] The integration over particles instead of grid cells, $W = -\sum_{i=1}^{N_{\rm part}} m_i\,(\boldsymbol{x}_i\cdot\boldsymbol{g}_i)$, with m_i being the mass of the i-th particle, which is located at position $\boldsymbol{x}_i$ and feels the acceleration $\boldsymbol{g}_i$, yields the same result, but is computationally more expensive.

ances and on approximately the same level (although very slightly higher) as the original or Newtonian Ramses code. To back up the latter statement, we set up a Plummer model similar to that described here in Sect. 4.4, but under the assumption of Newtonian dynamics to be valid. In this Newtonian model, the virial is approximately half of that of the Milgromian model. We evolve this model in the Newtonian Ramses code and plot the resulting energy error of both codes in Fig. 4.4. The average amplitude of the energy errors of both codes are similar. It is however noticeable that the variation of the error is slightly larger in the Milgromian code, which is due to the fact that the numerical error induced by the computation of the PDM density adds to the energy error.

General note on the overall code efficiency: RAMSES vs. POR

The title of this subsection could also have been "simple Poisson solver + DM particles vs. more sophisticated Poisson solver without the need of DM particles". On the one hand, this particular implementation of Milgromian dynamics requires solving the Poisson equation two times instead of only once per time step, making the force computation less efficient compared to the classical Newtonian Poisson solver of Ramses, assuming that both codes run with the same number of particles. On the other hand, Milgromian dynamics does not require any DM particles. If we take into account that a large fraction of particles used in galactic dynamics computations are DM particles, this advantage compensates (and even overcompensates) the handicap that comes with the more expensive QUMOND solver. Computations with the same number of baryonic particles are therefore generally faster in the DM-free framework.

4.5 Application

Beside the testing of the POR code, we demonstrate its functionality on the basis of basic dynamical applications. Besides the spherical equilibrium models in Sect. 4.4.2, these applications are (a) rotating disk galaxies and (b) disk galaxies with an initial bulge. We developed the software tools necessary to set up these components in Milgromian dynamics, which is generally not trivial. Having these basic tools at hand, we can construct initial conditions for more sophisticated models, e.g. galaxy-galaxy interactions, dwarf spheroidal galaxies orbiting a host galaxy, etc.

Disk galaxies, as rotation-supported objects, are known to be well described by Milgromian dynamics (Famaey and McGaugh, 2012). These objects obey the baryonic Tully-Fisher relation,

$$V_{\rm flat}^4 = G a_0 M_b \tag{4.17}$$

with a_0 being Milgrom's constant. This relation follows directly from Eq. 4.1, and holds true over more than five orders of magnitude in mass (Verheijen, 2001; McGaugh, 2011b, 2012). The observation of this relation is however in contradiction with the DM-hypothesis, because it in fact states that the flat rotation velocity, $V_{\rm flat}$, depends only on the total baryonic mass, although the mass of the dark matter does, in the standard model, constitute the largest fraction of the total mass ($\approx$ 80–90%). What is more, $V_{\rm flat}$ does not depend on the surface density. Given the available large statistical sample of galaxies with rotation curves (e.g. more than 100 objects analyzed by McGaugh, 2011b), this conflict with DM-based theories can be solved only with a large and thus unlikely amount of fine-tuning.

Also the mass discrepancy-acceleration (MDA) relation predicted by Milgromian dynamics, relating the observed rotation velocity $V_{\rm obs}$ to the theoretical rotation velocity $V_{\rm b}$ as deduced from the distribution

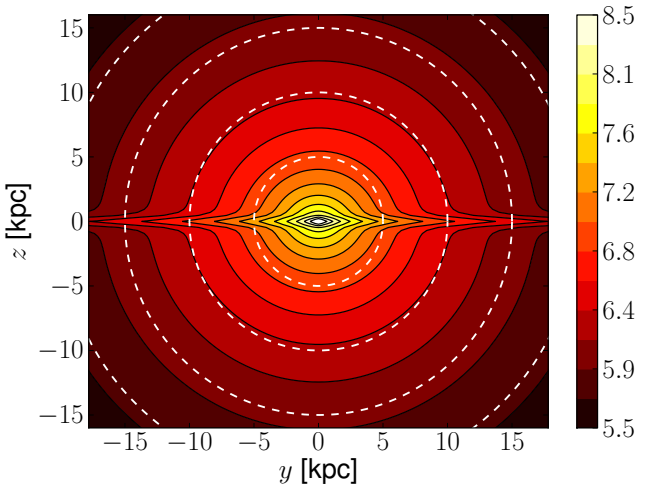

Figure 4.5: Phantom dark matter (PDM) density distribution of the exponential disk model described in Sect. 4.5.1 (logarithmic scale), $\log_{10}\left(\rho_{\rm ph}/\left(\mathrm{M}_\odot\,\mathrm{kpc}^{-3}\right)\right)$. The PDM distribution of a disk typically features a close-to-spherical (slightly oblate) halo component which has an isothermal density profile at large radii, $\rho_{\rm ph}(r) \propto r^{-2}$, and a dark disk component which is aligned with its baryonic counterpart, but has a different scale length. The phantom dark disk is one of the outstanding differences to the standard DM halo model.

of baryonic matter under the assumption of Newtonian gravity,

$$V_{\rm obs}^2/V_{\rm b}^2 = M_{\rm dyn}/M_{\rm b} = \nu(|g_{\rm N}|/a_0)\,, \tag{4.18}$$

is significantly visible in the data of rotation-supported galactic systems (Sanders, 1990; Scarpa, 2006; McGaugh, 2012). In this relation, $M_{\rm b}(r)$ is the baryonic mass enclosed in the galactocentric radius r, and $M_{\rm dyn}(r) = V_{\rm obs}^2(r)r/G$ is the related enclosed 'dynamical' mass inferred from the observed rotation velocity at radius r under the assumption of Newtonian dynamics to be valid. In the standard model, this dynamical mass would be interpreted as sum of the masses of baryonic and dark matter. Particularly the fact that the MDA relation includes also individual wiggles in the rotation curves is interesting, because such wiggles would be washed out by a existing CDM halo. The existence of either of these two relations, involving the *same* acceleration constant a_0, is not understood in the standard model, and is without reasonable argumentation claimed to emerge from not yet explored galactic feedback processes (McGaugh, 2011a; Foreman and Scott, 2012). On the other hand, these relations are natural consequences of the Milgromian framework. The observational data is perfectly in agreement with these relations, thus motivating to explore the Milgromian framework and its consequences in more detail.

To date, most predictions are based on static models simply using Eq. 4.1. Only few studies investigated the dynamical evolution of galaxies, and so the dynamical consequences of this DM-free framework are widely unexplored. The stability of stellar disks has been studied by Brada and Milgrom (1999) and more recently by Tiret and Combes (2007). As expected, the recent study shows that exponential disk galaxies qualitatively behave dynamically differently in the Newtonian+DM vs. Milgromian frameworks. While in the standard model disks are stabilized by pressure-support haloes made

of dissipationless DM particles, this is not the case in the Milgromian framework in which self-gravity plays a much larger role. It has been shown that disks are, in Milgromian dynamics, more sensitive to instabilities resulting in the formation of galactic bars. While galactic bars grow slowly in a DM-stablized halo, they form quickly in a DM-free Milgromian universe. Also dynamical friction behaves very differently. When the bar has formed in the DM-based model, it is subjected to dynamical friction with the DM particles, thus exchanging angular momentum and slowing down its pattern speed. This is not the case for the DM-free Milgromian dynamics, where the pattern speed stays constant for many Gyr.

Another difference between both models is that the Milgromian disk potential has, contrary to close-to-spherical particle DM haloes, a phantom dark disk component which is aligned with its baryonic counter-part (see Fig. 4.5), providing e.g. a stronger azimuthal force than the baryonic component alone. The scale lengths and heights of the phantom dark disk and the baryonic disk are however generally different.

Here, we create N-body models of disk galaxies, with and without a bulge, and compare them to those investigated in Tiret and Combes (2007) to demonstrate the performance of this code. While our computations are based on the QUMOND formulation, Tiret and Combes (2007) base their work on a different Milgromian dynamics theory, AQUAL (Bekenstein and Milgrom, 1984). Although both theories are similar, small quantitative differences are expected.

4.5.1 Rotating stellar disk

We set up a rotating exponential disk having the density distribution

$$\rho_{\rm b,disk}(R,z) = \rho_0 \exp(-R/R_{\rm d}) \,{\rm sech}^2(z/z_0)\,, \tag{4.19}$$

with $R_{\rm d}$ being the radial scale length and z_0 the azimuthal one. The model is initially in virial equilibrium.

To find matching initial conditions, we adapt the already available software by W. Dehnen, which is available with the Nemo (Barnes et al., 2010) software package and which is detailed in Dehnen (1999) and McMillan and Dehnen (2007). In the first step, we solve Eq. 4.2 with the density distribution ρ given by Eq. 4.19 using the POR code. We store the solution of the Milgromian potential and acceleration in a temporary file and provide it in the next step to the galaxy setup routine as external potential, and thereby replace the potential of the DM halo by the Milgromian equivalent.

We choose the radial velocity dispersion using Toomre's stability criterion (Toomre, 1964),

$$\sigma_{\rm r}(R) = Q\,\Sigma_{\rm crit}(R) = Q\frac{3.36\,G\,\Sigma_{\rm b}(R)}{\kappa(R)}\,. \tag{4.20}$$

Q is the Toomre parameter, G the gravitational constant, $\Sigma_{\rm b}(R)$ the surface density at galactic radius R, and $\kappa(R)$ the epicyclic frequency at the same radius. Q is supposed to be constant everywhere. $\Sigma_{\rm crit}$ is the so called critical surface density. The tangential velocity dispersion is set to

$$\sigma_\theta(R) = \frac{\kappa(R)}{2\Omega(R)}\sigma_r(R) \tag{4.21}$$

(e.g., Hernquist, 1993; Tiret and Combes, 2007), where $\Omega(R)$ is the angular frequency. The azimuthal velocity dispersion is defined by

$$\sigma_{\rm z}(R) = (R_{\rm d}\pi G\Sigma(R))^{1/2} \tag{4.22}$$

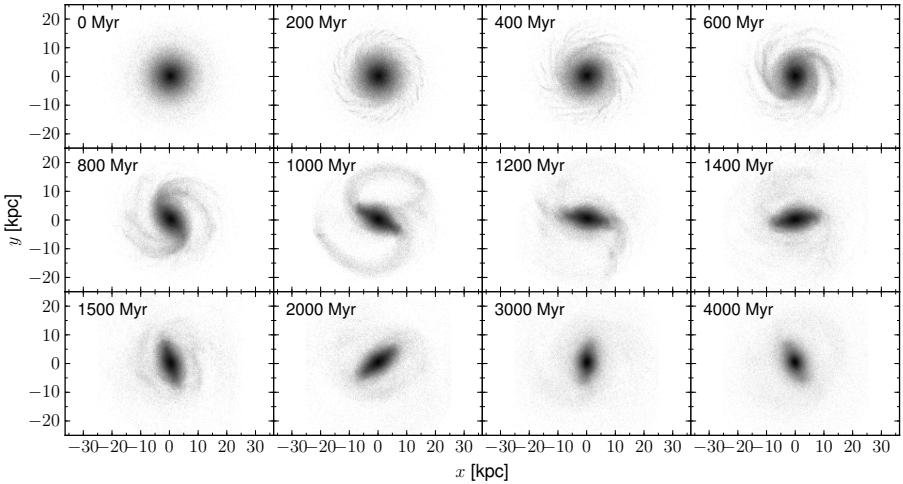

Figure 4.6: Evolution of an exponential disk with time in the new Milgromian N-body code, POR. The disk contains only stellar particles and is not embedded in a dark matter halo. It forms substructure within a few 100 Myr due to self-gravity. From these instabilities, a galactic bar grows within ≈ 1 Gyr. This bar rotates with a constant angular frequency for several billion years.

(e.g., Hernquist, 1993; Tiret and Combes, 2007). We initialize this model with 10^6 particles, total baryonic disk mass $M_\mathrm{d} = 5.4 \times 10^{10}\,\mathrm{M}_\odot$, $R_\mathrm{d} = 2.3\,\mathrm{kpc}$, $z_0 = 0.1 R_\mathrm{d}$, and $Q = 2$.[8] The disk is placed at the center of a box of the size $(1000\,\mathrm{kpc})^3$. The minimum grid resolution is $1000\,\mathrm{kpc}/2^7 = 7.8\,\mathrm{kpc}$, the maximum resolution is limited by the number of particles. In this case, this is $1000\,\mathrm{kpc}/2^{15} = 0.031\,\mathrm{kpc}$.

We let the model evolve for a few billion years and visualize the results in Fig. 4.6. The disk starts forming substructure quickly in the outer regions where the velocity dispersion is relatively small compared to the inner regions. After ≈ 500 Myr, the disk forms larger substructures in the form of spiral arms. And within 1 Gyr, it happens to form a rotating galactic bulge, which rotates with a constant angular frequency. After two more billion years, the bar weakens and a central spherical component forms, giving the galaxy the typical peanut-like shape.

To compare to the results of Tiret and Combes (2007), we compute at each time step the average absolute value of the ratio of azimuthal acceleration, g_ϕ, to radial acceleration, g_R,

$$\left\langle \left| g_\phi / g_\mathrm{R} \right| \right\rangle = \frac{1}{N_\mathrm{cells}} \sum_{i=1}^{N_\mathrm{cells}} \left| \frac{g_\phi}{g_\mathrm{R}} \right|_{i\text{-th cell}} , \tag{4.23}$$

assuming that all cells are of equal size.[9] Note that this definition is not exactly the same as the one applied by Tiret and Combes (2007), but it allows a meaningful comparison, keeping in mind that also the models are not exactly the same. The quantity defined by Eq. 4.23 is zero in spherical or cylindrical symmetry and increases when the bar forms. It is a useful indicator of the strength of the galactic bar,

[8] This model has been inspired by the Milky Way, it is however not intended to fit the original exactly.

[9] In Eq. 4.23, we restrict to cells that have a distance to the galactic center of $1.5\,\mathrm{kpc} < R < 25\,\mathrm{kpc}$ and which are located close to the galactic plane, $|z| \leq 0.5\,\mathrm{kpc}$. These parameters appeared to give a useful description of the bar strength.

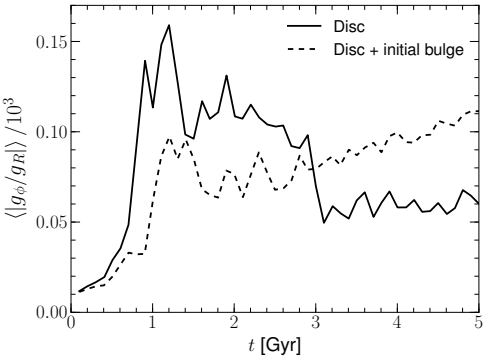

Figure 4.7: Evolution of the galactic bar strength or asymmetry of the galactic potential, $\left\langle\left|g_\phi/g_R\right|\right\rangle$ (see Eq. 4.23). In the case of the disk-only model, the bar grows within 1 Gyr, remains until $t \approx 3$ Gyr, and finally partly dissolves. What remains is a typical peanut-shaped galaxy. In the case of the disk model with initial bulge, the asymmetry of the galactic potential grows more slowly and continuously. The most prominent peak, which occurs between 1 Myr and 1.5 Myr is due to the formation of spiral arms.

or more generally the strength of non-axisymmetries. We plot this quantity vs. time in Fig. 4.7. In this plot, we see what we already noticed visually: the asymmetry grows quickly within ≈ 1 Gyr, stays until $t \approx 3$ Gyr, and then partly dissolves again. This is also what we see in figure 21 of Tiret and Combes (2007).

4.5.2 Adding a bulge to the rotating disk

Setting up a spheroidal bulge in a non-spherical potential is not trivial. One method to address this challenge is described in McMillan and Dehnen (2007). The bulge is initially set up in the spherical monopole expansion of the axissymmetric disk potential, and is then evolved in a N-body simulation, whereby the external spherical monopole potential is adiabatically transformed into the final non-spherical disk potential, to let the bulge settle in the actual potential of the axisymmetric galactic disk.

In the Milgromian framework, this is even more tricky, because the superposition of gravitational potentials is not applicable. To work around this limitation, we make the assumption that the Newtonian acceleration is, at the center of the galactic model, much larger than a_0, so that the dynamics breaks down to simple Newtonian dynamics locally. We thus set up the bulge as described in McMillan and Dehnen (2007) under the assumption of Newtonian dynamics to be valid.[10] For the disk setup, the full Milgromian gravitational potential of both, the disk and the bulge, is needed. Eq. 4.2 therefore needs to be solved for the disk+bulge density distribution. This is again performed using the POR code.

Because the critical suface density, $\Sigma_{\rm crit}$, looses its meaning in the bulge-dominated area, we adjust the radial velocity dispersion profile to

$$\sigma_r(R) \propto \exp(-R/(2R_{\rm d})) \tag{4.24}$$

(e.g., Dehnen, 1999). The proportionality constant is defined by the requirement that $Q(R_0) = Q_0$, with

[10] If in Eq. 4.2 the 'simple ν-function', $\nu(x) = 0.5 + \sqrt{1 + 4/x}$, is applied, we correct the potential by adding an additional potential $\phi(r) = a_0 r$ to the bulge potential, because this individual ν-function yields the acceleration $g \to g_{\rm N} + a_0$ in the Newtonian limit $a_0 \to 0$ and therefore not exactly $g_{\rm N}$.

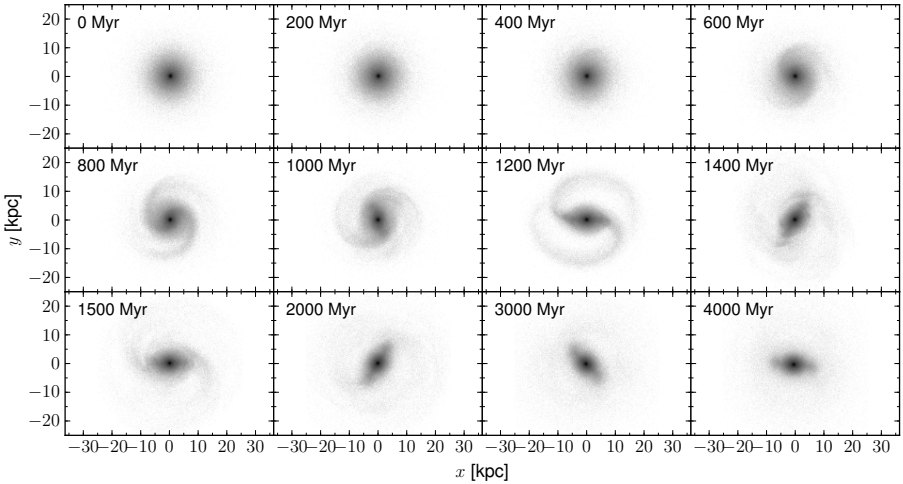

Figure 4.8: Evolution of an exponential disk + bulge model with time in the new Milgromian N-body code, POR. This model has a bulge that makes up ≈ 10% of the total mass. The bulge has a stabilizing effect on the disk and delays the formation of substructure due to self-gravitation. Particularly in the beginning the formation of small-scale substructure is suppressed. The full-length video of this computation is available as an online attachment to this paper and can also be viewed at youtu.be/GhR5w7qDTX8.

R_0 being a constant radius and Q_0 a dimensionless constant. This assumption is in agreement with observations (Sohn et al., 2012), and yields a radial velocity dispersion profile similar to Eq. 4.20 (apart from the galactic center).

Here, we set up a disk with the parameters similar to those used in Sect. 4.5.1, here with $Q(2R_\mathrm{d}) = 2$, and a Plummer bulge having the mass $M_\mathrm{b} = 0.6 \times 10^{10}\,\mathrm{M}_\odot$ and a half-mass radius of 1 kpc.

We let this model evolve using the same parameters as for the disk-only model and present the result in Fig. 4.8. This disk-bulge-model is notably more stable than the bulgeless disk model. In particular, the bulge potential strongly weakens the formation of the galactic bar. This happens to be the case because the bulge itself, as a pressure-supported system, is generally more stable than the rotation-supported disk component, providing the disk with an external potential having a stabilizing effect. Because the bulge makes up only a small fraction of the total mass (≈ 10%), it delays the formation of substructure but can not suppress it. As a consequence, the non-axisymmetry of the galactic potential grows continuously and more slowly than in the bulge-less model (see Fig. 4.7, dashed line). Also, this model shows an asymmetry peak in this figure due to the formation of spiral arms.

4.6 Summary and outlook

Milgromian dynamics has been very successful on galaxy scales in the last three decades. Most former predictions and tests have however been essentially of static nature, not studying the dynamical evolution of complex self-gravitating systems (with a few exceptions). The small number of efficient N-body codes has prevented from testing this theory in as many systems as the standard DM-based model.

Here, we presented a new Milgromian dynamics N-body code, which is a customized version of the

Ramses code. This code handles particles as well as gas dynamics, and provides a grid architecture based on the AMR technique, making it the right tool for a large range of possible applications. We demonstrated the good performance of the code based on static and dynamical benchmark models for which the analytical solutions are known. Furthermore, we presented models of rotating exponential disk models, with and without a central spherical bulge, thereby showing that we have at hand the tools necessary to set up such dynamical equilibrium models in the Milgromian DM-free framework.

Having such a code at hand, and being able to set up any kind of spherical equilibrium model as well as more complex disk galaxies, we will be able to build more sophisticated dynamical tests by combining these (e.g., galaxy mergers, formation of tidal dwarf galaxies, formation of tidal streams, etc.). Our future goals with this code are a) to test if already observed systems are in agreement or in contradiction with the theory, b) to make predictions that can observationally be tested, and c) to work out general, qualitative differences between Milgromian dynamics and the standard model in view of the dynamical consequences of each of the frameworks.

Bibliography

Alpher, R. A., Bethe, H., and Gamow, G. (1948). The Origin of Chemical Elements. *Physical Review*, 73:803–804.

Angus, G. W. (2008). Dwarf spheroidals in MOND. *MNRAS*, 387:1481–1488.

Angus, G. W. (2009). Is an 11eV sterile neutrino consistent with clusters, the cosmic microwave background and modified Newtonian dynamics? *MNRAS*, 394:527–532.

Angus, G. W. and Diaferio, A. (2011). The abundance of galaxy clusters in modified Newtonian dynamics: cosmological simulations with massive neutrinos. *MNRAS*, 417:941–949.

Angus, G. W., Gentile, G., Diaferio, A., Famaey, B., and Heyden, K. J. v. d. (2014). N-body simulations of the Carina dSph in MOND. *MNRAS*, 440:746–761.

Angus, G. W., van der Heyden, K. J., Famaey, B., Gentile, G., McGaugh, S. S., and de Blok, W. J. G. (2012). A QUMOND galactic N-body code - I. Poisson solver and rotation curve fitting. *MNRAS*, 421:2598–2609.

ATLAS Collab. (2011). Search for squarks and gluinos using final states with jets and missing transverse momentum with the ATLAS detector in $\sqrt{s} = 7\,\mathrm{TeV}$ proton-proton collisions. *Physics Letters B*, 701:186–203.

Babcock, H. W. (1939). The rotation of the Andromeda Nebula. *Lick Observatory Bulletin*, 19:41–51.

Barnes, J. and Hut, P. (1986). A hierarchical O(N log N) force-calculation algorithm. *Nature*, 324:446–449.

Barnes, J., Hut, P., and Teuben, P. (2010). NEMO: A Stellar Dynamics Toolbox. Astrophysics Source Code Library.

Barnes, J. E. and Hernquist, L. (1992). Formation of dwarf galaxies in tidal tails. *Nature*, 360:715–717.

Battaglia, G., Helmi, A., and Breddels, M. (2013). Internal kinematics and dynamical models of dwarf spheroidal galaxies around the Milky Way. *ArXiv e-prints*.

Begum, A., Chengalur, J. N., Karachentsev, I. D., and Sharina, M. E. (2008). Baryonic Tully-Fisher relation for extremely low mass Galaxies. *MNRAS*, 386:138–144.

Bekenstein, J. and Milgrom, M. (1984). Does the missing mass problem signal the breakdown of Newtonian gravity? *ApJ*, 286:7–14.

Bekenstein, J. D. (2004). Relativistic gravitation theory for the modified Newtonian dynamics paradigm. *Phys. Rev. D*, 70(8):083509.

Belokurov, V. (2013). Galactic Archaeology. The dwarfs that survived and perished. *ArXiv e-prints*.

Bennett, C. L., Larson, D., Weiland, J. L., Jarosik, N., Hinshaw, G., Odegard, N., Smith, K. M., Hill, R. S., Gold, B., Halpern, M., Komatsu, E., Nolta, M. R., Page, L., Spergel, D. N., Wollack, E., Dunkley, J., Kogut, A., Limon, M., Meyer, S. S., Tucker, G. S., and Wright, E. L. (2013). Nine-year Wilkinson Microwave Anisotropy Probe (WMAP) Observations: Final Maps and Results. *ApJS*, 208:20.

Bertone, G., Hooper, D., and Silk, J. (2005). Particle dark matter: evidence, candidates and constraints. *Physics Reports*, 405:279–390.

Bienaymé, O., Famaey, B., Siebert, A., Freeman, K. C., Gibson, B. K., Grebel, E. K., Kordopatis, G., Munari, U., Navarro, J. F., Reid, W., Seabroke, G. M., Siviero, A., Steinmetz, M., Wyse, R. F. G., and Zwitter, T. (2014). Weighing the local dark matter with RAVE red clump stars. *ArXiv e-prints*.

Binney, J. and Tremaine, S. (1987). *Galactic dynamics*.

Blanchet, L. and Bernard, L. (2014). Phenomenology of MOND and gravitational polarization. *ArXiv e-prints*.

Bosma, A. (1981). 21-cm line studies of spiral galaxies. I - Observations of the galaxies NGC 5033, 3198, 5055, 2841, and 7331. II - The distribution and kinematics of neutral hydrogen in spiral galaxies of various morphological types. *AJ*, 86:1791–1846.

Bournaud, F. (2010). Tidal Dwarf Galaxies and Missing Baryons. *Advances in Astronomy*, 2010.

Bournaud, F., Duc, P.-A., Brinks, E., Boquien, M., Amram, P., Lisenfeld, U., Koribalski, B. S., Walter, F., and Charmandaris, V. (2007). Missing Mass in Collisional Debris from Galaxies. *Science*, 316:1166–.

Bovy, J. and Tremaine, S. (2012). On the Local Dark Matter Density. *ApJ*, 756:89.

Boylan-Kolchin, M., Bullock, J. S., and Kaplinghat, M. (2011). Too big to fail? The puzzling darkness of massive Milky Way subhaloes. *MNRAS*, 415:L40–L44.

Brada, R. and Milgrom, M. (1999). Stability of Disk Galaxies in the Modified Dynamics. *ApJ*, 519:590–598.

Brada, R. and Milgrom, M. (2000). Dwarf Satellite Galaxies in the Modified Dynamics. *ApJ*, 541:556–564.

Brooks, A. M., Kuhlen, M., Zolotov, A., and Hooper, D. (2013). A Baryonic Solution to the Missing Satellites Problem. *ApJ*, 765:22.

Casas, R. A., Arias, V., Peña Ramírez, K., and Kroupa, P. (2012). Dwarf spheroidal satellites of the Milky Way from dark matter free tidal dwarf galaxy progenitors: maps of orbits. *MNRAS*, 424:1941–1951.

Combes, F. and Arnaboldi, M. (1996). The dark halo of polar-ring galaxy NGC 4650a: flattened towards the polar ring? *A&A*, 305:763.

de Blok, W. J. G. (2010). The Core-Cusp Problem. *Advances in Astronomy*, 2010.

Dehnen, W. (1999). Simple Distribution Functions for Stellar Disks. *AJ*, 118:1201–1208.

Disney, M. J., Romano, J. D., Garcia-Appadoo, D. A., West, A. A., Dalcanton, J. J., and Cortese, L. (2008). Galaxies appear simpler than expected. *Nature*, 455:1082–1084.

Eddington, A. S. (1916). *MNRAS*, 76:572.

Einasto, J. (1965). On the Construction of a Composite Model for the Galaxy and on the Determination of the System of Galactic Parameters. *Trudy Astrofizicheskogo Instituta Alma-Ata*, 5:87–100.

Faber, S. M. and Jackson, R. E. (1976). Velocity dispersions and mass-to-light ratios for elliptical galaxies. *ApJ*, 204:668–683.

Famaey, B., Bruneton, J.-P., and Zhao, H. (2007). Escaping from modified Newtonian dynamics. *MNRAS*, 377:L79–L82.

Famaey, B. and McGaugh, S. S. (2012). Modified Newtonian Dynamics (MOND): Observational Phenomenology and Relativistic Extensions. *Living Reviews in Relativity*, 15:10.

Ferguson, H. C. and Binggeli, B. (1994). Dwarf elliptical galaxies. *A&AR*, 6:67–122.

Foreman, S. and Scott, D. (2012). What Do Gas-Rich Galaxies Actually Tell Us about Modified Newtonian Dynamics? *Physical Review Letters*, 108(14):141302.

Freeman, K. C. (1970). On the Disks of Spiral and so Galaxies. *ApJ*, 160:811.

Gentile, G., Famaey, B., Combes, F., Kroupa, P., Zhao, H. S., and Tiret, O. (2007). Tidal dwarf galaxies as a test of fundamental physics. *A&A*, 472:L25–L28.

Gentile, G., Famaey, B., and de Blok, W. J. G. (2011). THINGS about MOND. *A&A*, 527:A76.

Giodini, S., Pierini, D., Finoguenov, A., Pratt, G. W., Boehringer, H., Leauthaud, A., Guzzo, L., Aussel, H., Bolzonella, M., Capak, P., Elvis, M., Hasinger, G., Ilbert, O., Kartaltepe, J. S., Koekemoer, A. M., Lilly, S. J., Massey, R., McCracken, H. J., Rhodes, J., Salvato, M., Sanders, D. B., Scoville, N. Z., Sasaki, S., Smolcic, V., Taniguchi, Y., Thompson, D., and COSMOS Collaboration (2009). Stellar and Total Baryon Mass Fractions in Groups and Clusters Since Redshift 1. *ApJ*, 703:982–993.

Guillet, T. and Teyssier, R. (2011). A simple multigrid scheme for solving the Poisson equation with arbitrary domain boundaries. *Journal of Computational Physics*, 230:4756–4771.

Hammer, F., Yang, Y., Fouquet, S., Pawlowski, M. S., Kroupa, P., Puech, M., Flores, H., and Wang, J. (2013). The vast thin plane of M31 co-rotating dwarfs: an additional fossil signature of the M31 merger and of its considerable impact in the whole Local Group. *ArXiv e-prints*.

Hees, A., Folkner, W. M., Jacobson, R. A., and Park, R. S. (2014). Constraints on MOND theory from radio tracking data of the Cassini spacecraft. *ArXiv e-prints*.

Hernandez, X., Jimenez, A., and Allen, C. (2014). Gravitational anomalies signaling the breakdown of classical gravity. *ArXiv e-prints*.

Hernandez, X. and Jiménez, M. A. (2012). The Outskirts of Globular Clusters as Modified Gravity Probes. *ApJ*, 750:9.

Hernandez, X., Jiménez, M. A., and Allen, C. (2012). Wide binaries as a critical test of classical gravity. *European Physical Journal C*, 72:1884.

Hernandez, X., Jiménez, M. A., and Allen, C. (2013). Flattened velocity dispersion profiles in globular clusters: Newtonian tides or modified gravity? *MNRAS*, 428:3196–3205.

Hernandez, X., Mendoza, S., Suarez, T., and Bernal, T. (2010). Understanding local dwarf spheroidals and their scaling relations under MOdified Newtonian Dynamics. *A&A*, 514:A101.

Hernquist, L. (1993). N-body realizations of compound galaxies. *ApJS*, 86:389–400.

Hughes, J. P. (1989). The mass of the Coma Cluster - Combined X-ray and optical results. *ApJ*, 337:21–33.

Ibata, R. A., Ibata, N. G., Lewis, G. F., Martin, N. F., Conn, A., Elahi, P., Arias, V., and Fernando, N. (2014). A Thousand Shadows of Andromeda: Rotating Planes of Satellites in the Millennium-II Cosmological Simulation. *ApJL*, 784:L6.

Ibata, R. A., Lewis, G. F., Conn, A. R., Irwin, M. J., McConnachie, A. W., Chapman, S. C., Collins, M. L., Fardal, M., Ferguson, A. M. N., Ibata, N. G., Mackey, A. D., Martin, N. F., Navarro, J., Rich, R. M., Valls-Gabaud, D., and Widrow, L. M. (2013). A vast, thin plane of corotating dwarf galaxies orbiting the Andromeda galaxy. *Nature*, 493:62–65.

Iodice, E. (2010). Polar Disk Galaxies as New Way to Study Galaxy Formation: the Case of NGC4650A. In Debattista, V. P. and Popescu, C. C., editors, *American Institute of Physics Conference Series*, volume 1240 of *American Institute of Physics Conference Series*, pages 379–382.

Iodice, E., Arnaboldi, M., Bournaud, F., Combes, F., Sparke, L. S., van Driel, W., and Capaccioli, M. (2003). Polar Ring Galaxies and the Tully-Fisher Relation: Implications for the Dark Halo Shape. *ApJ*, 585:730–738.

Iodice, E., Arnaboldi, M., Saglia, R. P., Sparke, L. S., Gerhard, O., Gallagher, J. S., Combes, F., Bournaud, F., Capaccioli, M., and Freeman, K. C. (2006). Stellar Kinematics for the Central Spheroid in the Polar Disk Galaxy NGC 4650A. *ApJ*, 643:200–209.

King, I. R. (1962). The structure of star clusters. I. an empirical density law. *AJ*, 67:471.

King, I. R. (1966). The structure of star clusters. III. Some simple dynamical models. *AJ*, 71:64.

Klessen, R. S. and Kroupa, P. (1998). Dwarf Spheroidal Satellite Galaxies without Dark Matter: Results from Two Different Numerical Techniques. *ApJ*, 498:143.

Kleyna, J. T., Wilkinson, M. I., Evans, N. W., and Gilmore, G. (2004). Dark Matter in the Draco and UMi dSphs. In Prada, F., Martinez Delgado, D., and Mahoney, T. J., editors, *Satellites and Tidal Streams*, volume 327 of *Astronomical Society of the Pacific Conference Series*, page 169.

Klypin, A., Kravtsov, A. V., Valenzuela, O., and Prada, F. (1999). Where Are the Missing Galactic Satellites? *ApJ*, 522:82–92.

Komatsu, E., Smith, K. M., Dunkley, J., Bennett, C. L., Gold, B., Hinshaw, G., Jarosik, N., Larson, D., Nolta, M. R., Page, L., Spergel, D. N., Halpern, M., Hill, R. S., Kogut, A., Limon, M., Meyer, S. S., Odegard, N., Tucker, G. S., Weiland, J. L., Wollack, E., and Wright, E. L. (2011). Seven-year

Wilkinson Microwave Anisotropy Probe (WMAP) Observations: Cosmological Interpretation. *ApJS*, 192:18.

Kraus, C., Bornschein, B., Bornschein, L., Bonn, J., Flatt, B., Kovalik, A., Ostrick, B., Otten, E. W., Schall, J. P., Thümmler, T., and Weinheimer, C. (2005). Final results from phase II of the Mainz neutrino mass searchin tritium {β} decay. *European Physical Journal C*, 40:447–468.

Kravtsov, A. V., Klypin, A. A., and Khokhlov, A. M. (1997). Adaptive Refinement Tree: A New High-Resolution N-Body Code for Cosmological Simulations. *ApJS*, 111:73.

Kroupa, P. (1997). Dwarf spheroidal satellite galaxies without dark matter. *NA*, 2:139–164.

Kroupa, P. (2012). The Dark Matter Crisis: Falsification of the Current Standard Model of Cosmology. *PASA*, 29:395–433.

Kroupa, P. (2014). Galaxies as simple dynamical systems: observational data disfavor dark matter and stochastic star formation. *ArXiv e-prints*.

Kroupa, P., Famaey, B., de Boer, K. S., Dabringhausen, J., Pawlowski, M. S., Boily, C. M., Jerjen, H., Forbes, D., Hensler, G., and Metz, M. (2010). Local-Group tests of dark-matter concordance cosmology . Towards a new paradigm for structure formation. *A&A*, 523:A32.

Kroupa, P., Pawlowski, M., and Milgrom, M. (2012). The Failures of the Standard Model of Cosmology Require a New Paradigm. *International Journal of Modern Physics D*, 21:30003.

Lacey, C. and Cole, S. (1993). Merger rates in hierarchical models of galaxy formation. *MNRAS*, 262:627–649.

Llinares, C., Knebe, A., and Zhao, H. (2008). Cosmological structure formation under MOND: a new numerical solver for Poisson's equation. *MNRAS*, 391:1778–1790.

Londrillo, P. and Nipoti, C. (2009). N-MODY: a code for collisionless N-body simulations in modified Newtonian dynamics. *Memorie della Societa Astronomica Italiana Supplementi*, 13:89.

Lüghausen, F., Famaey, B., and Kroupa, P. (2014a). Phantom of RAMSES (POR): A new Milgromian dynamics N-body code. *CJP, in press*.

Lüghausen, F., Famaey, B., and Kroupa, P. (2014b). Polar Ring Galaxies Favor Milgromian Dynamics over Standard Dark-Matter-Based Models. In *Astronomical Society of the Pacific Conference Series*, volume 486 of *Astronomical Society of the Pacific Conference Series*, page 225.

Lüghausen, F., Famaey, B., Kroupa, P., Angus, G., Combes, F., Gentile, G., Tiret, O., and Zhao, H. (2013). Polar ring galaxies as tests of gravity. *MNRAS*, 432:2846–2853.

LUX Collab. (2013). First results from the LUX dark matter experiment at the Sanford Underground Research Facility. *ArXiv e-prints*.

Macciò, A. V., Paduroiu, S., Anderhalden, D., Schneider, A., and Moore, B. (2012). Cores in warm dark matter haloes: a Catch 22 problem. *MNRAS*, 424:1105–1112.

Marks, M. and Kroupa, P. (2011). Dynamical population synthesis: constructing the stellar single and binary contents of galactic field populations. *MNRAS*, 417:1702–1714.

Mateo, M., Olszewski, E., Welch, D. L., Fischer, P., and Kunkel, W. (1991). A kinematic study of the Fornax dwarf spheroidal galaxy. *AJ*, 102:914–926.

Mateo, M. L. (1998). Dwarf Galaxies of the Local Group. *ARA&A*, 36:435–506.

McConnachie, A. W. (2012). The Observed Properties of Dwarf Galaxies in and around the Local Group. *AJ*, 144:4.

McGaugh, S. (2011a). Missing the Point - a Brief Reply to Foreman AMP Scott and Gnedin. *ArXiv e-prints*.

McGaugh, S. and Milgrom, M. (2013a). Andromeda Dwarfs in Light of Modified Newtonian Dynamics. *ApJ*, 766:22.

McGaugh, S. and Milgrom, M. (2013b). Andromeda Dwarfs in Light of MOND. II. Testing Prior Predictions. *ArXiv e-prints*.

McGaugh, S. S. (1996). The number, luminosity and mass density of spiral galaxies as a function of surface brightness. *MNRAS*, 280:337–354.

McGaugh, S. S. (2004). The Mass Discrepancy-Acceleration Relation: Disk Mass and the Dark Matter Distribution. *ApJ*, 609:652–666.

McGaugh, S. S. (2005a). Balance of Dark and Luminous Mass in Rotating Galaxies. *Physical Review Letters*, 95(17):171302.

McGaugh, S. S. (2005b). The Baryonic Tully-Fisher Relation of Galaxies with Extended Rotation Curves and the Stellar Mass of Rotating Galaxies. *ApJ*, 632:859–871.

McGaugh, S. S. (2008a). Milky Way Mass Models and MOND. *ApJ*, 683:137–148.

McGaugh, S. S. (2008b). Reconstructing the Mass Profile of the Milky Way. In *AAS/Division of Dynamical Astronomy Meeting #39*, volume 39 of *AAS/Division of Dynamical Astronomy Meeting*, page #01.04.

McGaugh, S. S. (2011b). Novel Test of Modified Newtonian Dynamics with Gas Rich Galaxies. *Physical Review Letters*, 106(12):121303.

McGaugh, S. S. (2012). The Baryonic Tully-Fisher Relation of Gas-rich Galaxies as a Test of ΛCDM and MOND. *AJ*, 143:40.

McGaugh, S. S. (2014). A Tale of Two Paradigms: the Mutual Incommensurability of LCDM and MOND. *ArXiv e-prints*.

McGaugh, S. S., Schombert, J. M., Bothun, G. D., and de Blok, W. J. G. (2000). The Baryonic Tully-Fisher Relation. *ApJL*, 533:L99–L102.

McGaugh, S. S., Schombert, J. M., de Blok, W. J. G., and Zagursky, M. J. (2010). The Baryon Content of Cosmic Structures. *ApJL*, 708:L14–L17.

McGaugh, S. S. and Wolf, J. (2010). Local Group Dwarf Spheroidals: Correlated Deviations from the Baryonic Tully-Fisher Relation. *ApJ*, 722:248–261.

McMillan, P. J. and Dehnen, W. (2007). Initial conditions for disc galaxies. *MNRAS*, 378:541–550.

Merritt, D., Graham, A. W., Moore, B., Diemand, J., and Terzić, B. (2006). Empirical Models for Dark Matter Halos. I. Nonparametric Construction of Density Profiles and Comparison with Parametric Models. *AJ*, 132:2685–2700.

Milgrom, M. (1983). A modification of the Newtonian dynamics as a possible alternative to the hidden mass hypothesis. *ApJ*, 270:365–370.

Milgrom, M. (1994). Dynamics with a Nonstandard Inertia-Acceleration Relation: An Alternative to Dark Matter in Galactic Systems. *Annals of Physics*, 229:384–415.

Milgrom, M. (1995). MOND and the Seven Dwarfs. *ApJ*, 455:439.

Milgrom, M. (1999). The modified dynamics as a vacuum effect. *Physics Letters A*, 253:273–279.

Milgrom, M. (2001). The shape of 'dark matter' haloes of disc galaxies according to MOND. *MNRAS*, 326:1261–1264.

Milgrom, M. (2002). MOND – theoretical aspects. *NAR*, 46:741–753.

Milgrom, M. (2008). The MOND paradigm. *ArXiv e-prints*.

Milgrom, M. (2009a). Bimetric MOND gravity. *Phys. Rev. D*, 80(12):123536.

Milgrom, M. (2009b). MOND effects in the inner Solar system. *MNRAS*, 399:474–486.

Milgrom, M. (2009c). The central surface density of 'dark haloes' predicted by MOND. *MNRAS*, 398:1023–1026.

Milgrom, M. (2009d). The Mond Limit from Spacetime Scale Invariance. *ApJ*, 698:1630–1638.

Milgrom, M. (2010). Quasi-linear formulation of MOND. *MNRAS*, 403:886–895.

Milgrom, M. (2011). MOND–particularly as modified inertia. *ArXiv e-prints*.

Milgrom, M. (2014). MOND theory. *ArXiv e-prints*.

Miyamoto, M. and Nagai, R. (1975). Three-dimensional models for the distribution of mass in galaxies. *PASJ*, 27:533–543.

Moiseev, A. V., Smirnova, K. I., Smirnova, A. A., and Reshetnikov, V. P. (2011). A new catalogue of polar-ring galaxies selected from the Sloan Digital Sky Survey. *MNRAS*, 418:244–257.

Moore, B., Ghigna, S., Governato, F., Lake, G., Quinn, T., Stadel, J., and Tozzi, P. (1999). Dark Matter Substructure within Galactic Halos. *ApJL*, 524:L19–L22.

Navarro, J. F., Frenk, C. S., and White, S. D. M. (1997). A Universal Density Profile from Hierarchical Clustering. *ApJ*, 490:493–508.

Navarro, J. F., Ludlow, A., Springel, V., Wang, J., Vogelsberger, M., White, S. D. M., Jenkins, A., Frenk, C. S., and Helmi, A. (2010). The diversity and similarity of simulated cold dark matter haloes. *MNRAS*, 402:21–34.

Nieuwenhuizen, T. M. (2009). Do non-relativistic neutrinos constitute the dark matter? *EPL (Europhysics Letters)*, 86:59001.

Nipoti, C., Ciotti, L., Binney, J., and Londrillo, P. (2008). Dynamical friction in modified Newtonian dynamics. *MNRAS*, 386:2194–2198.

Nusser, A. (2002). Modified Newtonian dynamics of large-scale structure. *MNRAS*, 331:909–916.

Oort, J. H. (1932). The force exerted by the stellar system in the direction perpendicular to the galactic plane and some related problems. *Bulletin of the Astronomical Institutes of the Netherlands*, 6:249.

Ostriker, J. P. and Peebles, P. J. E. (1973). A Numerical Study of the Stability of Flattened Galaxies: or, can Cold Galaxies Survive? *ApJ*, 186:467–480.

Ostriker, J. P. and Steinhardt, P. J. (1995). The observational case for a low-density Universe with a non-zero cosmological constant. *Nature*, 377:600–602.

Padmanabhan, T. (1993). Books-Received - Structure Formation in the Universe. *Journal of the British Astronomical Association*, 103:193.

Pawlowski, M., Famaey, B., Jerjen, H., Merritt, D., Kroupa, P., Dabringhausen, J., Lüghausen, F., Forbes, D., Hensler, G., Hammer, F., Puech, M., Fouquet, S., Flores, H., and Yang, Y. (2014). The planes' truth: co-orbiting satellite galaxy structures are still in conflict with the distribution of primordial dwarf galaxies. *submitted*.

Pawlowski, M. S., Kroupa, P., Angus, G., de Boer, K. S., Famaey, B., and Hensler, G. (2012a). Filamentary accretion cannot explain the orbital poles of the Milky Way satellites. *MNRAS*, 424:80–92.

Pawlowski, M. S., Pflamm-Altenburg, J., and Kroupa, P. (2012b). The VPOS: a vast polar structure of satellite galaxies, globular clusters and streams around the Milky Way. *MNRAS*, 423:1109–1126.

Peebles, P. J. E. and Nusser, A. (2010). Nearby galaxies as pointers to a better theory of cosmic evolution. *Nature*, 465:565–569.

Perlmutter, S., Aldering, G., Goldhaber, G., Knop, R. A., Nugent, P., Castro, P. G., Deustua, S., Fabbro, S., Goobar, A., Groom, D. E., Hook, I. M., Kim, A. G., Kim, M. Y., Lee, J. C., Nunes, N. J., Pain, R., Pennypacker, C. R., Quimby, R., Lidman, C., Ellis, R. S., Irwin, M., McMahon, R. G., Ruiz-Lapuente, P., Walton, N., Schaefer, B., Boyle, B. J., Filippenko, A. V., Matheson, T., Fruchter, A. S., Panagia, N., Newberg, H. J. M., Couch, W. J., and Project, T. S. C. (1999). Measurements of Ω and Λ from 42 High-Redshift Supernovae. *ApJ*, 517:565–586.

Planck Collab. (2013a). Planck 2013 results. XV. CMB power spectra and likelihood. *ArXiv e-prints*.

Planck Collab. (2013b). Planck 2013 results. XVI. Cosmological parameters. *ArXiv e-prints*.

Plummer, H. C. (1911). On the problem of distribution in globular star clusters. *MNRAS*, 71:460–470.

Reshetnikov, V. P. and Combes, F. (1994). Kinematics and dark haloes of polar-ring galaxies. *A&A*, 291:57–73.

Riess, A. G., Filippenko, A. V., Challis, P., Clocchiatti, A., Diercks, A., Garnavich, P. M., Gilliland, R. L., Hogan, C. J., Jha, S., Kirshner, R. P., Leibundgut, B., Phillips, M. M., Reiss, D., Schmidt, B. P., Schommer, R. A., Smith, R. C., Spyromilio, J., Stubbs, C., Suntzeff, N. B., and Tonry, J. (1998). Observational Evidence from Supernovae for an Accelerating Universe and a Cosmological Constant. *AJ*, 116:1009–1038.

Rubin, V. C. and Ford, Jr., W. K. (1970). Rotation of the Andromeda Nebula from a Spectroscopic Survey of Emission Regions. *ApJ*, 159:379.

Rubin, V. C., Ford, W. K. J., and . Thonnard, N. (1980). Rotational properties of 21 SC galaxies with a large range of luminosities and radii, from NGC 4605 /R = 4kpc/ to UGC 2885 /R = 122 kpc/. *ApJ*, 238:471–487.

Rubin, V. C., Thonnard, N., and Ford, Jr., W. K. (1978). Extended rotation curves of high-luminosity spiral galaxies. IV - Systematic dynamical properties, SA through SC. *ApJL*, 225:L107–L111.

Sackett, P. D., Rix, H.-W., Jarvis, B. J., and Freeman, K. C. (1994). The flattened dark halo of polar ring galaxy NGC 4650A: A conspiracy of shapes? *ApJ*, 436:629–641.

Sackett, P. D. and Sparke, L. S. (1990). The dark halo of the polar-ring galaxy NGC 4650A. *ApJ*, 361:408–418.

Sancisi, R. (2004). The visible matter – dark matter coupling. In Ryder, S., Pisano, D., Walker, M., and Freeman, K., editors, *Dark Matter in Galaxies*, volume 220 of *IAU Symposium*, page 233.

Sanders, R. H. (1990). Mass discrepancies in galaxies - Dark matter and alternatives. *A&AR*, 2:1–28.

Sanders, R. H. (1999). The Virial Discrepancy in Clusters of Galaxies in the Context of Modified Newtonian Dynamics. *ApJL*, 512:L23–L26.

Sanders, R. H. (2007). Neutrinos as cluster dark matter. *MNRAS*, 380:331–338.

Sanders, R. H. (2010). The universal Faber-Jackson relation. *MNRAS*, 407:1128–1134.

Sanders, R. H. and McGaugh, S. S. (2002). Modified Newtonian Dynamics as an Alternative to Dark Matter. *ARA&A*, 40:263–317.

Scarpa, R. (2006). Modified Newtonian Dynamics, an Introductory Review. In Lerner, E. J. and Almeida, J. B., editors, *First Crisis in Cosmology Conference*, volume 822 of *American Institute of Physics Conference Series*, pages 253–265.

Schmidt, B. P., Suntzeff, N. B., Phillips, M. M., Schommer, R. A., Clocchiatti, A., Kirshner, R. P., Garnavich, P., Challis, P., Leibundgut, B., Spyromilio, J., Riess, A. G., Filippenko, A. V., Hamuy, M., Smith, R. C., Hogan, C., Stubbs, C., Diercks, A., Reiss, D., Gilliland, R., Tonry, J., Maza, J., Dressler, A., Walsh, J., and Ciardullo, R. (1998). The High-Z Supernova Search: Measuring Cosmic Deceleration and Global Curvature of the Universe Using Type IA Supernovae. *ApJ*, 507:46–63.

Schweizer, F., Whitmore, B. C., and Rubin, V. C. (1983). Colliding and merging galaxies. II - S0 galaxies with polar rings. *AJ*, 88:909–925.

Serra, A. L., Angus, G. W., and Diaferio, A. (2010). Implications for dwarf spheroidal mass content from interloper removal. *A&A*, 524:A16.

Shull, J. M., Smith, B. D., and Danforth, C. W. (2012). The Baryon Census in a Multiphase Intergalactic Medium: 30% of the Baryons May Still be Missing. *ApJ*, 759:23.

Silk, J. (1968). Cosmic Black-Body Radiation and Galaxy Formation. *ApJ*, 151:459.

Skordis, C., Mota, D. F., Ferreira, P. G., and Bœhm, C. (2006). Large Scale Structure in Bekenstein's Theory of Relativistic Modified Newtonian Dynamics. *Physical Review Letters*, 96(1):011301.

Smith, S. (1936). The Mass of the Virgo Cluster. *ApJ*, 83:23.

Smoot, G. F., Bennett, C. L., Kogut, A., Wright, E. L., Aymon, J., Boggess, N. W., Cheng, E. S., de Amici, G., Gulkis, S., Hauser, M. G., Hinshaw, G., Jackson, P. D., Janssen, M., Kaita, E., Kelsall, T., Keegstra, P., Lineweaver, C., Loewenstein, K., Lubin, P., Mather, J., Meyer, S. S., Moseley, S. H., Murdock, T., Rokke, L., Silverberg, R. F., Tenorio, L., Weiss, R., and Wilkinson, D. T. (1992). Structure in the COBE differential microwave radiometer first-year maps. *ApJL*, 396:L1–L5.

Sohn, S. T., Anderson, J., and van der Marel, R. P. (2012). The M31 Velocity Vector. I. Hubble Space Telescope Proper-motion Measurements. *ApJ*, 753:7.

Spergel, D. N. and Steinhardt, P. J. (2000). Observational Evidence for Self-Interacting Cold Dark Matter. *Physical Review Letters*, 84:3760.

Springel, V., White, S. D. M., Jenkins, A., Frenk, C. S., Yoshida, N., Gao, L., Navarro, J., Thacker, R., Croton, D., Helly, J., Peacock, J. A., Cole, S., Thomas, P., Couchman, H., Evrard, A., Colberg, J., and Pearce, F. (2005). Simulations of the formation, evolution and clustering of galaxies and quasars. *Nature*, 435:629–636.

Steinmetz, M. and Navarro, J. F. (1999). The Cosmological Origin of the Tully-Fisher Relation. *ApJ*, 513:555–560.

Strigari, L. E. (2012). arxiv:1211.7090.

Strigari, L. E., Bullock, J. S., Kaplinghat, M., Simon, J. D., Geha, M., Willman, B., and Walker, M. G. (2008). A common mass scale for satellite galaxies of the Milky Way. *Nature*, 454:1096–1097.

Teyssier, R. (2002). Cosmological hydrodynamics with adaptive mesh refinement. A new high resolution code called RAMSES. *A&A*, 385:337–364.

Tiret, O. and Combes, F. (2007). Evolution of spiral galaxies in modified gravity. *A&A*, 464:517–528.

Tiret, O. and Combes, F. (2008). Evolution of spiral galaxies in modified gravity. II. Gas dynamics. *A&A*, 483:719–726.

Toomre, A. (1964). On the gravitational stability of a disk of stars. *ApJ*, 139:1217–1238.

Trippe, S. (2014). The "Missing Mass Problem" in Astronomy and the Need for a Modified Law of Gravity. *ArXiv e-prints*.

Tully, R. B. and Fisher, J. R. (1977). A new method of determining distances to galaxies. *A&A*, 54:661–673.

van den Bergh, S. (1999). The Early History of Dark Matter. *PASP*, 111:657–660.

Verheijen, M. A. W. (2001). The Ursa Major Cluster of Galaxies. V. H I Rotation Curve Shapes and the Tully-Fisher Relations. *ApJ*, 563:694–715.

Vogelsberger, M., Genel, S., Springel, V., Torrey, P., Sijacki, D., Xu, D., Snyder, G. F., Nelson, D., and Hernquist, L. (2014). Introducing the Illustris Project: Simulating the coevolution of dark and visible matter in the Universe. *ArXiv e-prints*.

Walker, M. G. (2013). *Dark Matter in the Galactic Dwarf Spheroidal Satellites*, page 1039.

Walker, M. G., Mateo, M., and Olszewski, E. W. (2009). Stellar Velocities in the Carina, Fornax, Sculptor, and Sextans dSph Galaxies: Data From the Magellan/MMFS Survey. *AJ*, 137:3100–3108.

Walker, M. G., Mateo, M., Olszewski, E. W., Gnedin, O. Y., Wang, X., Sen, B., and Woodroofe, M. (2007). Velocity Dispersion Profiles of Seven Dwarf Spheroidal Galaxies. *ApJL*, 667:L53–L56.

Walker, M. G. and Peñarrubia, J. (2011). A Method for Measuring (Slopes of) the Mass Profiles of Dwarf Spheroidal Galaxies. *ApJ*, 742:20.

Wang, J., Frenk, C. S., and Cooper, A. P. (2013). The spatial distribution of galactic satellites in the Λ cold dark matter cosmology. *MNRAS*, 429:1502–1513.

Whitmore, B. C., Lucas, R. A., McElroy, D. B., Steiman-Cameron, T. Y., Sackett, P. D., and Olling, R. P. (1990). New observations and a photographic atlas of polar-ring galaxies. *AJ*, 100:1489–1522.

Will, C. M. (2006). The Confrontation between General Relativity and Experiment. *Living Reviews in Relativity*, 9:3.

XENON100 Collab. (2012). Dark Matter Results from 225 Live Days of XENON100 Data. *Physical Review Letters*, 109(18):181301.

Zhao, H. (1997). Analytical dynamical models for double power-law galactic nuclei. *MNRAS*, 287:525–537.

Zhao, H. and Famaey, B. (2010). Comparing different realizations of modified Newtonian dynamics: Virial theorem and elliptical shells. *Phys. Rev. D*, 81(8):087304.

Zhao, H., Famaey, B., Lüghausen, F., and Kroupa, P. (2013). Local Group timing in Milgromian dynamics. A past Milky Way-Andromeda encounter at z > 0.8. *A&A*, 557:L3.

Zlosnik, T. G., Ferreira, P. G., and Starkman, G. D. (2007). Modifying gravity with the aether: An alternative to dark matter. *Phys. Rev. D*, 75(4):044017.

Zwicky, F. (1933). Die Rotverschiebung von extragalaktischen Nebeln. *Helvetica Physica Acta*, 6:110–127.

List of Figures